AD-A060 586 MASSACHUSETTS INST OF TECH LEXINGTON LINCOLN LAB F/G 10/3
FLYWHEEL COMPONENTS FOR SATELLITE APPLICATIONS.(U)
MAY 78 A R MILLNER
UNCLASSIFIED TN-1978-4 ESD-TR-78-97 F19628-78-C-0002 NL



DDC FILE COPY

AD A060586

LEVEL II

12

MASSACHUSETTS INSTITUTE OF TECHNOLOGY

LINCOLN LABORATORY

FLYWHEEL COMPONENTS FOR SATELLITE APPLICATIONS

A. R. MILLNER

Group 68

ACCESSION for
NTIS White Section
DDC Buff Section
UNANNOUNCED
JUSTIFICATION
BY
DISTRIBUTION/AVAILABILITY CODES
Dist. AVAIL. and/or SPECIAL
A

TECHNICAL NOTE 1978-4

16 MAY 1978

DDC
RECEIVED
NOV 1 1978
D

Approved for public release; distribution unlimited.

LEXINGTON MASSACHUSETTS

78 10 23 064

ABSTRACT

The following paper studies the possibilities of using high-speed flywheels with magnetic bearings in communications spacecraft. Hardware point designs have been completed for a very low drag bearing and a very efficient, compatible motor generator. Using the results of these designs, a tradeoff study compares these flywheels with combinations of NiCd batteries, NiH_2 batteries, and conventional low-speed momentum wheels.

Section I presents the tradeoff studies for flywheels used for energy storage only, for attitude control only, and for combined energy storage and attitude control. The results show that such wheels look excellent for attitude control alone (as high-speed, high-reliability momentum wheels) and attractive for combined power and attitude control, but not much better than NiH_2 for power alone.

Section II reviews the technology of flywheel components, showing that rotors are the biggest unsolved problem but can be built now to lower energy densities.

Section III analyzes two types of anisotropic rotors to allow design calculations for a given set of material properties. These types are the orthotropic composite rotor and the bare filament rotor.

Section IV documents the design, development, and testing of the Lincoln Laboratory magnetic bearing. This bearing can be used in momentum wheels which are not electronically gimballed, or in energy storage wheels.

Section V documents the development of the Lincoln Laboratory motor generator, which allows very high efficiency at high speeds.

Section VI contains overall conclusions of this study concerning spacecraft applications of high-speed flywheels.

TABLE OF CONTENTS

		Page
	ABSTRACT	iii
	LIST OF FIGURES	vii
	LIST OF TABLES	ix
I.	SYSTEM ASPECTS OF FLYWHEELS	1
	A. Flywheel Control	1
	B. Energy Storage Only	6
	C. Attitude Control Only	10
	D. Flywheel Combined Energy Storage and Attitude Control	16
II.	TECHNOLOGY SURVEY	26
	A. Rotor	26
	B. Magnetic Bearings	28
	C. Touchdown Bearings	31
	D. Motor-Generator	31
	E. Shaft and Housing Design	31
III.	ROTOR ANALYSIS	32
	A. Orthotropic Rotor, Analytical Analysis	32
	B. Bare Filament Rotor Analysis	35
	References	53
IV.	MAGNETIC BEARING INVESTIGATION	54
	A. Mechanical Design Concept	54
	B. Calculations	59
	C. Loop Design	63
	D. Magnetic Bearing Integration and Test	63
	E. Finite Element and Field Plotting Capabilities	77
V.	MOTOR GENERATOR	85
	A. Design Goals and Tradeoffs	85
	B. Design Realization	86
VI.	CONCLUSIONS	88

PRECEDING PAGE NOT FILMED
BLANK

Table of Contents (Cont'd.)

	Page
APPENDIX A: Lincoln Motor-Generator Design (Contract with Sperry Rand Corporation)	89
A.1 Introduction and Purposes	90
A.2 Requirements	90
A.3 Summary of Results	90
A.4 Selection of Motor/Generator Type and Drive Interface	92
A.5 Motor/Generator Design	100
A.6 Comments on Sample Fabrication	112
A.7 Two-Phase Continuously Commutated Efficiency Calculations	119
A. Motoring	119
A.8 Three Phase, Discretely Commutated Efficiency Calculations	124
A. Motoring	125
B. Generating	126
A.9 Rotor Stress Calculations	128
A.10 Addendum - Final Report	131
ACKNOWLEDGEMENT	135

LIST OF FIGURES

		Page
Fig. 1-1	Flywheel parameter relationship.	2
Fig. 1-2	Momentum wheel rotating unit tradeoffs.	5
Fig. 1-3	Magnetic bearing momentum wheel, type MDR.	18
Fig. 1-4	Wheel speed control loop diagram.	20
Fig. 3-1	Orthotropic rotor geometry.	32
Fig. 3-2	Single fiber configuration.	39
Fig. 3-3a	Smallest and intermediate roots of F(v) = 0.	44
Fig. 3-3b	Largest root of F(v) = 0.	44
Fig. 3-4	Maximum tension and attachment angle.	48
Fig. 3-5	Contribution of circumferential fiber loads to total load applied to the hub.	52
Fig. 4-1	Design layout of magnetic bearing test bed.	55
Fig. 4-2	Magnetic bearing system test.	68
Fig. 4-3	Bearing stator assembly and test bed.	69
Fig. 4-4	Construction of bearing stator.	70
Fig. 4-5	Bearing stator and rotor.	71
Fig. 4-6	Flywheel and shaft.	72
Fig. 4-7	Touchdown bearings.	73
Fig. 4-8	Touchdown bearing housing.	74
Fig. 4-9	Assembly fixtures.	75
Fig. 4-10	Bearing control panel.	76
Fig. 4-11	Drag vs. speed.	78
Fig. 4-12	Drag vs. pressure.	79

Fig. 4-13 Finite elements. 81

Fig. 4-14 Potential contours. 82

Fig. 4-15 Field intensity contours. 83

Fig. 4-16 Flux density contours. 84

Fig. A-1 Performance and outline drawing of brushless dc motor-generator. 93

Fig. A-2 High voltage M/G drive concept. 96

Fig. A-3 Construction of rotor. 110

Fig. A-4 Output voltage waveshape and phasing. 114

Fig. A-5 Output uniformity. 115

Fig. A-6 Breadboard unit in test fixture. 116

Fig. A-7 Stator for breadboard unit. 117

Fig. A-8 Rotor for breadboard unit. 118

Fig. A-9 Motoring diagram. 119

Fig. A-10 Magnetic circuit. 131

LIST OF TABLES

		Page
1-1	Single Flywheel Characteristics	7
1-2	Two Wheel Power-Only System	8
1-3	Battery System Comparisons	9
1-4	Power-Only Weight Tradeoff	11
1-5	GPSCS ACS Tradeoff	14
1-6	Requirements for LES Momentum Wheel	17
1-7	Weight and Power Budget for Combined Power and ACS Flywheels	22
1-8	Combined Energy and Momentum Storage Tradeoff	24
A-1	Motor Generator Requirements	91
A-2	System Configuration Comparison	97
A-3	Driver Efficiency Comparison	99
A-4	Generator Performance	106
A-5	Motor Performance	107
A-6	Stress Summary	109
A-7	Test Data on Breadboard Unit	113

I. SYSTEM ASPECTS OF FLYWHEELS

A. Flywheel Control

A flywheel system will be considered in the context of a synchronous communication satellite mission. Assume a 1 KW payload and an attitude control system with required stability of ± .01° with dominant solar torques on the order of 50 microfoot pounds sinusoidal component.

The Lincoln Laboratory (LL) flywheel unit concept briefly consists of a rotor, shaft, magnetic bearings, touchdown bearings, motor-generator, vacuum housing, and miscellaneous small parts. To ease unit integration for a first cut we have selected a small shaft with essentially zero internal rotor diameter, although this costs a factor of two in rotor weight compared to the limit of ID/OD → 1. We will assume two levels of rotor technology: a 34 watt-hour per pound, 40 K RPM rotor, probably achievable with present technology and minor improvements in fabrication techniques; and a 54 watt-hour per pound 50 K RPM rotor of the same size (20-in. dia.), probably the ultimate for present materials and the given geometry. Vacuum containment was chosen rather than lightweight covers for flight to provide complete testing of a fully assembled unit and to add bearing mount rigidity and small fragment confinement.

These units, denoted LL-30 and LL-50, are estimated to weigh respectively 45 and 50 pounds. They will be considered first as purely energy storage devices in competition with batteries, then as momentum wheels in competition with presently available and current prototype designs, and finally as combined energy and angular momentum storage devices.

The essential relationships between wheel speed, energy, momentum, and mass are given below and graphed in Fig. 1-1. A disc rotor with inner radius R_I and outer radius R_o, mass density p and thickness h has

$$\text{mass} \qquad M = \pi p h \, (R_I^2 - R_o^2) \tag{1-1}$$

$$\text{moment of inertia} \qquad I = 1/2 \, M \, (R_I^2 + R_o^2) \tag{1-2}$$

$$\text{angular momentum} \qquad H = I\omega \tag{1-3}$$

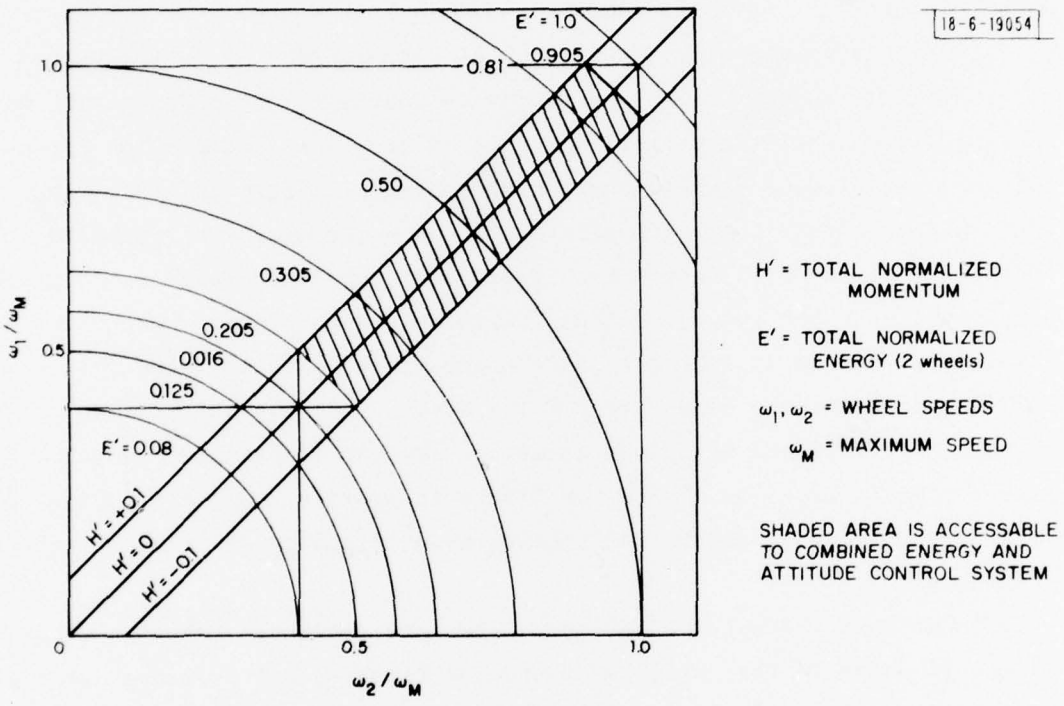


Fig. 1-1. Flywheel parameter relationship.

energy $E = 1/2\ I\omega^2 = 1/2\ H\omega$ (1-4)

energy/mass $E/M = 1/4\ (R_I^2 + R_o^2)\ \omega^2$ (1-5)

momentum/mass $H/M = 1/2\ (R_I^2 + R_o^2)\ \omega$ (1-6)

For our case R_I = o and for normalized variables $\omega' = \omega/\omega_m$ where ω_m = maximum speed. Total energy of two wheels $E' = E/I\omega_m^2$, $H' = H/I\omega_m$.

$$E' = 1/2\ (\omega_1'^2 + \omega_2'^2) \quad (1-7)$$

$$H' = \omega_1' - \omega_2' \quad (1-8)$$

A big concern with any energy wheel system on a satellite will be the large angular momentum (H) stored in their energy system, and its potential effects on attitude control. A basic ground rule of any such system must be that no likely single point failure shall cause total loss of the satellite. This implies that the following failure modes must not be very likely.

1. Rotor breaking catastrophically, throwing high-energy fragments.
2. Suspension totally lost at high speed, causing rotor failure.
3. Wheel overspeed.

On a less stringent level, to avoid a recoverable tumbling of the satellite, the following would be desirable:

1. ACS automatic rate-dumping mode not dependent on any one wheel.
2. Wheel speed control redundancy.
3. Simple, reliable suspension with redundancy and recovery capability.
4. A touchdown bearing system capable of at least 100 touchdowns and 100 hour continuous running at design speed, perhaps with increased power requirements.
5. Simple energy conversion from generator to suspension, including touchdown recovery.

The result of these conditions would then be a flywheel energy system which would not be likely to disturb the attitude control of the satellite in case of component failure, and would not result in total loss of satellite even if it did so.

The implications for construction of the flywheel are as follows:

1. High confidence in the rotor not to break catastrophically.

2. Redundant overspeed control.

3. A radially passive suspension system, the simplest and most reliable choice, is very attractive unless active axial suspension can be made fully redundant without compromising simplicity and reliability.

4. Redundant axial suspension, possibly with ground intervention by command.

5. A reliable high-speed touchdown bearing system.

6. Redundant motor-generator windings if the wheel energy storage function must be recovered.

7. Efficient, low-power suspension.

In looking at the actual realization of such a wheel system, several points became clear:

1. Most realizations of active suspension electronics include several failure modes which result in touchdown at high speed with reduced chance of automatic recovery, but with ground-commanded recovery capability. Very careful design in this area may result in a low probability of touchdown.

2. A radially passive, axially active (RPAA) magnetic suspension with a V-groove mechanical touchdown skid on the ball bearing races gives a simple caging mechanism for launch; simply remove bearing power or bottom the wheel actively.

3. The RPAA magnetic suspension results in a penalty in spinning energy losses due to eddy current drag. There is a great deal of work to be done in the area to minimize the drag. Wheel balancing is important to minimize this loss. Low stiffness ratio (see below) is also important.

4. The RPAA suspension requires a broadband audio frequency servo-loop design with possible complications due to acoustic resonances of the structure. The loop bandwidth is approximately equal to the time constant $\sqrt{K_A/M}$ where M is the rotor mass and K_A is the axial negative spring constant of the passive magnetic suspension. This loop must be designed into the structure of the satellite, and structural modes included in the loop design.

5. The axial spring constant K_A is about five to ten times the positive radial spring constant K_R which passively centers the rotor. For 1G operation and the required cross-axis rates ω_c, this stiffness must be large enough to avoid touchdown. The minimization of stiffness ratio is a development area with big payoff.

6. The touchdown system is most reliable with small (several mils to ten mils) clearances. This implies clearance S less than some maximum, limiting motions for a fixed disturbing force or torque, and so requiring a high stiffness from the magnetic bearings and a wide-band servo problem with acoustics to complicate matters.

Cross axis torque: $$(K_R L - K_A \frac{D^2}{L}) \frac{S}{L} > \omega_c H \qquad (1\text{-}9)$$

1G support: $$K_R S > MG \qquad (1\text{-}10)$$

Stiffness Ratio: $$K_A > N K_R \qquad 5 < N < 10 \qquad (1\text{-}11)$$

Plugging in, $$f_{Loop} > \frac{1}{2\pi} \sqrt{\frac{NG}{S}} \qquad (1\text{-}12)$$

For S = 10 mils, N = 8 this gives $f_{Loop} > 89$ Hz, a range in which careful design is required to avoid acoustics. Also, sensing elements at this bandwidth must be carefully designed to avoid noise pickup and phase shift.

Notice that the cross-axis torque equation (1) puts a limit, not only on minimum K_R, but on the aspect ratio of the fringing rings D/L, where D = diameter of ring and L = spacing along the axis between bearings. For good cross-axis torque we need $D/L << K_R/K_A$. This determines the system axial length.

7. Nutation damping may be a serious limitation to wheel speed. For damping at nutation frequencies in the suspension system, wide loop bandwidths (several to 10 times rotational rate) are needed and wheel inbalance couples into the suspension to produce losses. This area needs work for an imbalance-tolerant system; composite wheels tend to suffer from balance problems.

With these matters in mind, the LL flywheel unit has been designed. The following sections use it as a basis for system trade-off studies.

B. Energy Storage Only

The basic energy storage unit for a flywheel system is a pair of wheels controlled to give zero total angular momentum. For minimum $\omega' = 0.4$, Eq. (1-7) gives an accessible energy $\Delta E' = 0.84$. This limit occurs because the motor-generator is effectively torque-limited. At constant H, the torque required for a power level P is

$$T = I \frac{d\omega}{dt} = P/(\omega_1 + \omega_2) \qquad (1\text{-}13)$$

This is maximum at minimum ω.

The characteristics of the flywheel unit are listed in Table 1-1. Note that, for power only, the flywheel accessible energy to weight ratio for the rotating unit is a bit more than a third that of the rotor alone. Then, to convert the power out to usable DC, the electrical efficiencies and weights of machine, electronics, and other components are estimated in Table 1-2. This costs another factor of two in available energy to system weight. However, the final figures are quite respectable.

The competitor battery systems fall into several classes. Batteries may be NiCd or NiH_2. They may be operated at various depth of discharge (DOD) levels, with statistics for various resulting lifetimes. They may be operated through charger and discharger electronics for a fully regulated bus, but this eliminates the inherent advantage of a battery as a DC voltage source. The tradeoff study shown in Table 1-3 presents the options. Option I represents a NiCd lightweight battery with 50% battery-level redundancy, 60% DOD, with charger but no discharge converter, so that the bus floats at the battery output voltage level during eclipse. Option II is a NiH_2 battery on a fully

TABLE 1-1

SINGLE FLYWHEEL CHARACTERISTICS

Rotor Type	LL-30	LL-50
Rotor, 10-in. radius, lbs. (Kg)	20 (9.08)	20 (9.08)
Motor-generator, lbs.	5	10
Bearings, lbs.	10	10
Vacuum housing, lbs.	5	5
Shaft, lbs.	3	3
Miscellaneous lbs.	2	2
Total weight, lbs.	45	50
Speed range, RPM	16K-40K	20K-50K
Max. Rotor E/M, w-h/lb.	34	54
Max. Stored E, w-h (MJ)	680 (2.45)	1080 (5.89)
Available E, w-h, $H' = 0.1$	476	756
Available E, w-h, $H' = 0$	571	907
Available E/M, $H' = 0$	12.7	18.1
1.2 hr. Discharge Rate, $H' = 0$	475	755
Moment of Inertia, $Kg\text{-}m^2$	0.29	0.29
H, Angular Momentum, ft.-lb.-sec. (N-M-S)	867 (1188)	1084 (1485)

TABLE 1-2

2-WHEEL POWER-ONLY SYSTEM

DISCHARGING CHARACTERISTICS IN ECLIPSE

	LL-30	LL-50
Output power from wheels, W	950	1510
Generating machine efficiency %	96	96
Generating bridge efficiency %	92.5	92.5
Drag power from bus, W	20	20
Suspension and control power from bus, W	5	5
Output power to load	819	1316
Total generating efficiency %	86	87
Bridge weight, lbs., .035 lb./watt	76	42
Control electric weight, lb., .005 lb./watt	3.6	6.0
Suspension electric weight, lb.	5.0	5.0
Total electric weight, lb.	34.6	53.0
Total system weight	124.6	153.0
Total system output energy (w-h) 1.2 hr.	983	1579
Total system E/M, w-h/lb.	7.9	10.3

CHARGING CHARACTERISTICS IN SUNLIGHT, 10 HOUR RATE

Average drag losses, W	20	20
Suspension and control power, W	5	5
Wheel input power, W	114	182
Motoring efficiency, motor, %	94.5	94.5
Motoring efficiency, bridge, %	89.5	89.5
Total input power, W	160	240
Charging efficiency, %	71	76

TABLE 1-3

BATTERY SYSTEM COMPARISONS

1.0 Kw System

Option I: NiCd batteries, 50% battery redundant, with charger but no discharges, only diode isolation and protection, 6.8 w-h/lb., 60% DOD.

Option II: NiH_2 batteries, 20% cell redundant, with charges and discharger for fully regulated bus, 75% DOD, 14 w-h/lb.

Option III: NiH_2 batteries, 20% cell redundant, with charger but only output isolation and protection, 75% DOD, 17 w-h/lb.

	I	II	III
Control power, W	5	5	5
Discharge efficiency	.95	.85	.95
Total discharge power, W	1057	1181	1057
Stored E, w-h	1263	1417	1263
Charger efficiency, c/10	.8	.8	.8
Heater power, W	40	40	40
Charging input power, W	197	217	197
Charger and heater weight, lb. (.11 lb./W)	21.7	23.9	21.7
Discharger weight, lb. (.05 or .025 lb/W)	26	59	26
Total electronics weight, lb.	48	83	48
Battery weight with redundancy, lb.	262	101	90

regulated bus, with 20% cell level redundancy and 75% DOD. Option III, the lightest, is Option II without the discharge converter.

The resulting figures in Table 1-4 show system weight at 1 KW load, system E/M, input charging load on the solar arrays, extra resulting solar array weight, and total weight.

Based on these figures, it is easy to see that either NiH_2 or flywheel storage is much lighter than NiCd batteries. Both are developmental, but NiH_2 is far more advanced and no heavier. Because of this, there does not appear to be good reason to pursue flywheels purely for energy storage. Even the LL-50 system with its higher energy density does not look much better than nickel-hydrogen batteries.

Note also that the conditioning electronics become significant sources of power loss and system weight in both Option II and LL-50. This implies that the inherent DC voltage source nature of the chemical battery seems to give lightweight NiH_2 or similar systems an ultimate edge over kinetic storage.

C. Attitude Control Only

A high energy density flywheel should make a very lightweight momentum wheel. At first glance, the optimization would favor a larger diameter and lower speed for best momentum density. However, this tradeoff very quickly is limited by the size of the wheel and the form factor of the enclosure. In fact, simply by reducing the speed of an energy wheel by a healthy factor to reduce the stresses gives a rather attractive momentum storage device.

How much angular momentum is enough? Several criteria could be used. For a LES-8/9 type biased momentum system, the maximum solar torque acting over the 6 hours of uncontrolled yaw should produce a negligible yaw rotation. Taking worst case numbers of 50 microfoot-pounds and yaw $\varepsilon = 1.2°$ gives a bias requirement of $H = 2T/\omega_o\varepsilon = 68$ ft.-lb.-secs., a moderate figure, for daily $\omega_o = 7.3 \times 10^{-5}$ rad/sec.

Another criterion would be to avoid any thrusting due to the daily solar torque variation. For a daily ω_o we have

TABLE 1-4

POWER-ONLY WEIGHT TRADEOFF

1.2 KW-Hr. Battery

	I	II	III	LL-30	LL-50
				X 1.22	X .760
Total system weight, lbs.	310	184	138	152	116
System E/M, W-hr./lbs. usable	3.87	6.52	8.69	7.9	10.3
Input charging load, W	197	217	197	195	182
Extra solar array wt., .11 lb./W	22	24	22	21	20
Total Weight Penalty, lbs.	332	208	160	173	136

$$\Delta H = \int_{\omega_o t=0}^{\pi} T_o \sin \omega_o t \, dt = \frac{2T_o}{\omega_o} \tag{1-14}$$

For T_o = 50 μft.-lb. this gives ΔH = 1.37 ft.-lb.-sec. If this is to tip over the wheel by no more than, say, 1.2°, this gives a momentum requirement

$$\frac{\Delta H}{H} \leq 2 \times 10^{-2} \text{ radians} \tag{1-15}$$

or H > 70 ft.-lb.-sec. This is a moderately large angular momentum, as determined in the next section. To avoid tipping over by 0.12° would require 700 ft.-lb.-sec., certainly a large wheel, about the size of the energy storage prototype wheel (45 lbs.) using advanced flywheel technology.

One criterion of angular momentum size is to ask whether, if all the angular momentum of the wheel were suddenly transferred to the spacecraft, the craft would survive. For a spacecraft moment of inertia of 10^3 Kg-m^2 and a maximum recoverable body rate of 1 RPM (W = .1 rad/sec) this would allow H = 100 N-m-s or 74 ft.-lb.-sec. Another criterion would be whether the angular momentum could change by, say, 1% and not seriously interfere with operations. For allowable rates of .05°/sec. ($\omega = 10^{-3}$) this would give H = 100 ft.-lb.-sec., so the criteria are roughly equivalent. By these criteria, any zero bias system will have small momentum, and the minimum 2.5 ft.-lb.-sec. bias is also small. A biased system avoiding daily thrust is marginal. An energy storage system is large.

To compare attitude control capabilities alone, consider four possibilities. First, consider only a 10 ft.-lb.-sec. wheel with enough extra fuel to last 10 years thrusting against daily solar torque variations. Second, consider four 10 ft.-lb.-sec. reaction wheels with no bias momentum. Third, consider a 100 ft.-lb.-sec. wheel with conventional construction. Last, consider a LES-30

wheel scaled down to a 7-in. radius and 5-lb. rotor. The system weight tradeoff and LES weight budget is shown in Table 1-5.

To arrive at fuel penalty weight, we have used a specific impulse of gas of 100 secs., and a moment arm of 2.5 ft. Solar torque at $4T_o/\omega$ for T_o = 50 μft.-lb. gives 3 ft.-lbs. per day for 3650 days totals 1.1×10^4 ft.-lb.-sec. or 44 lbs. of gas. Wheel weights are taken from the rule $M = 7H^{0.4}$ which gives a good fit to Bendix wheel weights over a wide range, plotted on Fig. 1-2.

Note that the scaled-down LL flywheel is not that far in momentum or weight from the Teldix MSR momentum ring, which was an iron rotor and 5-axis active magnetic bearings with a hollow ring geometry to achieve high momentum at lower speeds. (See Eq. 6: if $R_I = R_o$, then ω can be half as large for the same H.)

The result of the tradeoff is clear: the weight and complexity of the 4-wheel Option II is poor. The weight of Option I (small wheel, extra gas) is slightly higher than Option III (large conventional wheel) but both are far heavier than Option IV, the advanced flywheel. The message is that lighter, longer-lasting momentum wheels can now be built and should be used.

One other possibility is very attractive for a high-speed magnetically suspended wheel. Magnetic gimballing of the flywheel rotor is possible without adding any extra hardware, provided that the offset angle is small enough. The Teldix wheel with all active suspension can do this simply by changing the offset on the four cross-axis position sensors. A permanent magnet passive suspension can also be modified to do this, but with more drag in the offset (gimballed) condition perhaps. Rotation is limited by bearing gap geometry to 0.5 to 1.2 degrees, depending on the design.

To allow complete 3-axis stabilization (no angle at all) the cross-axis momentum must equal the integrated daily solar torque over a day. From our assumptions and Eq. (10) we need 1.37 ft.-lb.-sec. Allowing 1.2° gimballing gives a 70 ft.-lb.-sec. wheel (100 n-m-s) which can be achieved with the existing Teldix MDR momentum wheel. An improved subscale version of this now has fully redundant windings for all bearings and motor, providing the needed reliability for a long-duration version. Therefore, the MDR type

TABLE 1-5

GPSCS ACS TRADEOFF

	I Single 10 FPS Wheel	II 4-10 FPS Wheels	III 100 FPS Wheel	IV LL-30 Wheel
Bias momentum - Ft.-lb.-sec.	10	0	100	100
Weight, 1 wheel	20	20	50	15
Weight, all wheels	20	80	50	15
Weight fuel penalty	44	0	0	0
Total weight	50	80	50	15
Structure Penalty Weight	0	20	0	0
Elect. weight	5	20	10	10
Total Weight	69	120	60	25
Complexity	good	poor	good	good

15-lb. 100 FPS Wheel LL-30 Variety-Weight Budget

Rotor 40K RPM, R = 7" M	5.0 lb.	E/M = 16 $^{W-H}$/lb.
M/G	2.0 lb.	
Mag bearing	3.0 lb.	
Housing	3.0 lb.	
Shaft and misc.	2.0 lb.	
	15.0 lb.	

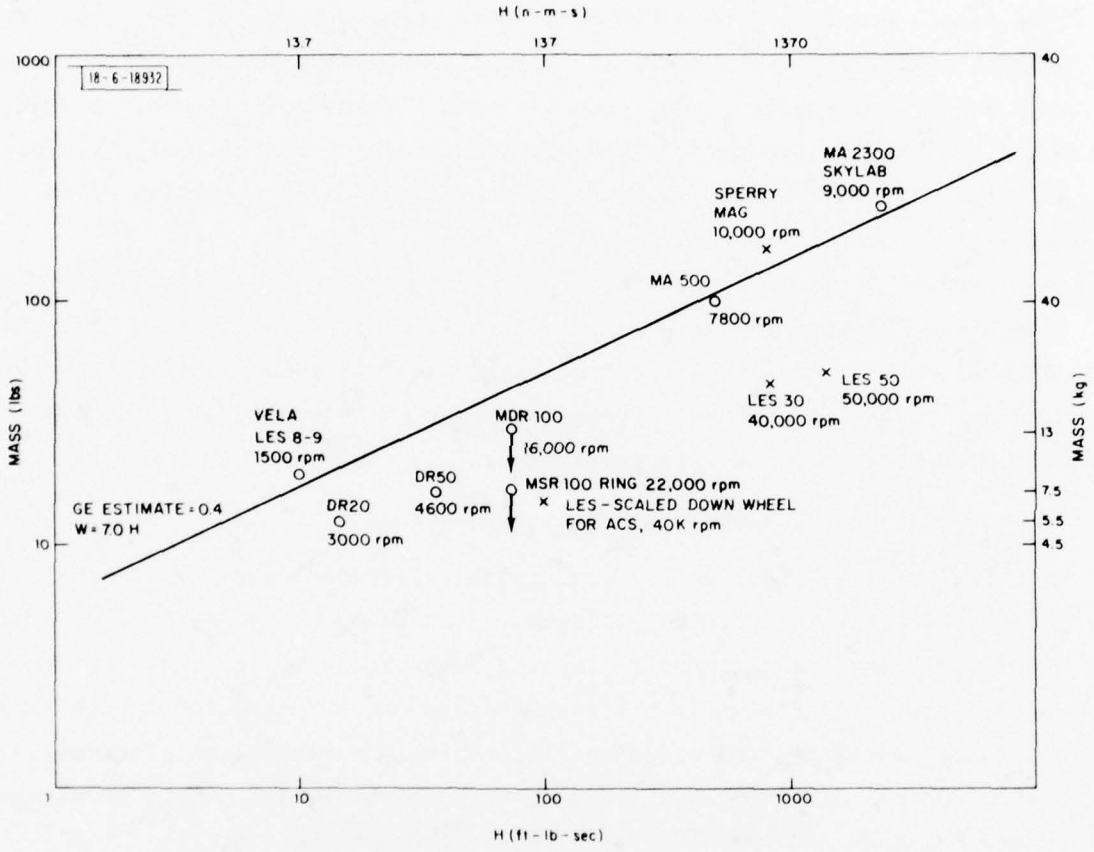


Fig. 1-2. Momentum wheel rotating unit tradeoffs.

wheel at 70 ft.-lb.-sec. with redundant windings is probably the best candidate for a general-purpose platform with 3-axis stabilization and low fuel utilization.

The unit weighs only about 20 lbs. and has no wear-out mechanism which appears worse than electronics reliability for long-term use in space. The only single-point failure would be a short between turns in the motor or bearing coils, so these should be carefully inspected and tested and treated as a mechanical defect rather than a random electronics failure. The unit would be able to operate over a much wider range of temperatures than previous ball-bearing systems, and would therefore allow a simplification of the satellite's thermal control.

Table 1-6 gives requirements for such a wheel. Figure 1-3 shows construction of an MDR type Teldix wheel, similar to that proposed here. The Teldix MDR wheel with increased gimballing angle and full redundancy in all coils and windings represents the best general-purpose fully stabilized platform element presently near complete development.

D. Flywheel Energy Storage and Attitude Control

The basic flywheel energy storage and attitude control unit consists of two wheels with axes carefully aligned, spun in opposite directions to give the desired angular momentum and energy combination. Note that only the control law is different from energy storage alone. Associated with each flywheel are generating and motoring electronics and suspension electronics. System control electronics are common to both wheels and create wheel speed change commands for the wheel motor-generator electronics.

At any given instant of time, the system controller desires each of the two wheels to be running at a given speed to contain the correct total energy and angular momentum. Figure 1-1 gives the relationship between the wheel speeds ω_1 and ω_2 and the angular momentum and energy of the system. All quantities are normalized to the maximum speed ω_M. Note that, since the motor-generator is designed to operate over a limited speed range (nominally $.4\ \omega_M < \omega < \omega_M$) only the upper right portion of the plot is useful. At constant stored energy,

TABLE 1-6

REQUIREMENTS FOR LES MOMENTUM WHEEL MAGNETIC BEARINGS,
ELECTRONICALLY GIMBALLED BASED ON TELDIX MDR WHEEL
NOMINAL MINIMUM REQUIREMENT

	English	MKS
Angular momentum	> 75 ft.-lb.-sec.	100 N-M-S
Momentum range	> ± 10%	± 10%
Electronic gimballing	> 1.2°	20 mrad
Momentum component	> 1.4 ft.-lb.-sec.	2 N-M-S
Slewing rate	> 5°/sec.	0.1 rad/sec.
Gimballing torque	> 3.5 ft.-lb.	5 N-M
Motor torque	> .035 ft.-lb.	.05 N-M
Nominal speed	> 16,000 RPM	16,000 RPM
Weight, no electronics	< 22 lbs.	10 kg
OD	< 12 inches	.3 m
Height	< 8 inches	.2 m
Power, steady state, 0G	< 10 W	10 W
Caging for launch	Yes	Yes
Suspension	Electromagnetic, 5-axis active touchdown ball bearings	
Motor	DC brushless	
Redundancy	All motor and suspension windings. No single-point failures except coil shorts or mechanical failure. Automatic fault detection and recovery.	

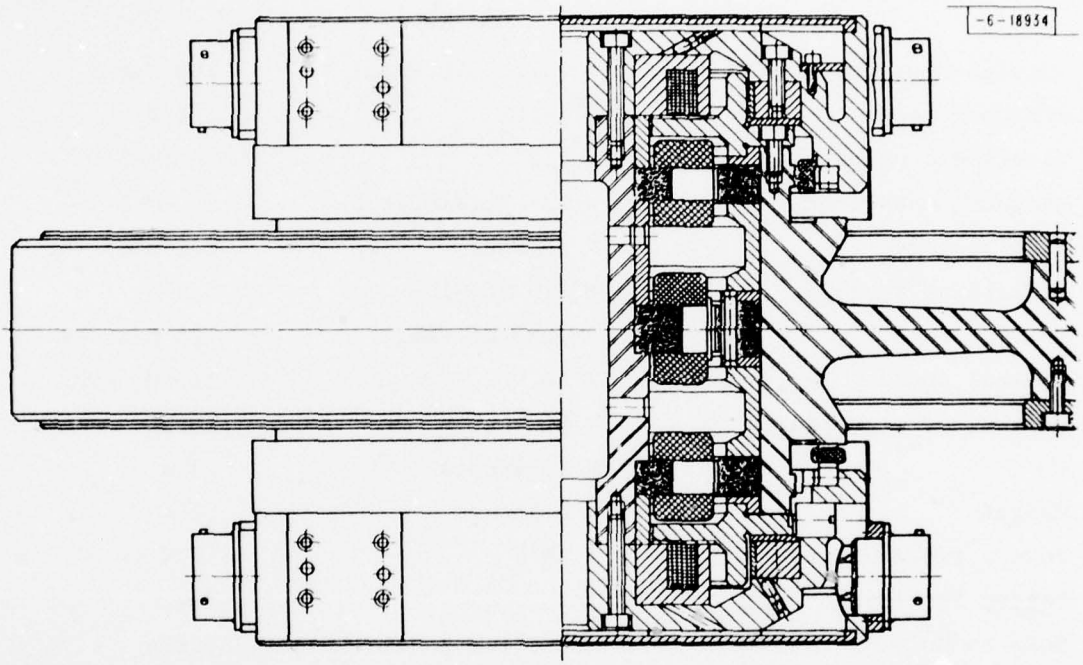


Fig. 1-3. Magnetic bearing momentum wheel, type MDR.

the system operates along the circular arcs centered on the origin to vary angular momentum. Such variations would be quite small for a system with large bias. (Typically $H/I\omega_M = .1$, $\Delta\omega/\omega_M < .01$.) At constant momentum, the system energy is charged and discharged along the straight lines with positive slope shown. Note that for these values with $H/I\omega_M = 0$, $\Delta E/I\omega_M^2 = .84$ or 84% of the maximum stored energy is accessible. For $H/I\omega_M = .1$, this reduces to 70%.

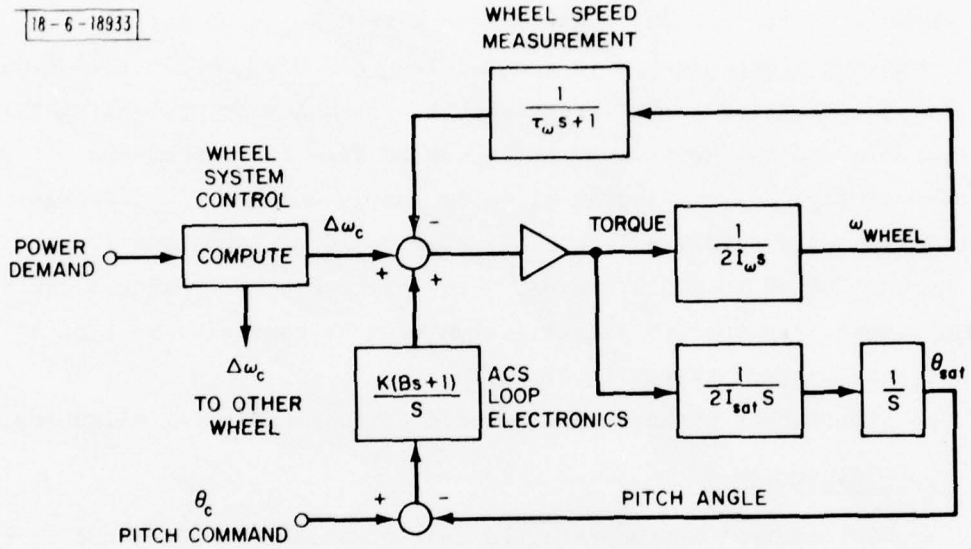
It is comforting to know that such a system has no unusual stability problems, and indeed the control system shown in Fig. 1-4 represents a first-cut at a stable control system diagram allowing energy and momentum management with relatively simple topology. Such a system could have perhaps 10-sec. transient response times to disturbances, with a second-order response and adjustable damping ratio. In reality such a system must be carefully modeled to include the attitude control system in detail.

Two other areas of concern are speed control and wheel alignment.

Speed Control

Our control system requires that the speed of the wheel be measured within $\tau_\omega = .5$ sec. Can it be done accurately enough in that time? Assume the motor-generator has N poles which are sensed as they pass. Assume a 1 MHz = f clock counts the interval between poles, so that in τ_ω seconds we receive $f\,\tau_\omega$ counts and the wheel rotates $N_\omega/2\pi\,\tau_\omega$ poles, $\omega = 2\pi\,(\text{RPM})/60$.

We can then measure ω within one part in fT_ω, which for our numbers is 5×10^5. This is well within the stability of a good clock (parts in 10^8) and sets the angular momentum within the same accuracy for constant wheel inertia I_ω. An error of H/fT_ω in angular momentum causes a satellite rate of $\omega_s = H/I_s fT_\omega$ which for our numbers is $I_s = 10^3$ Kg-m^2, $H = 10^3$ N-M-S, $\omega_s = 2 \times 10^{-6}$ which is well below the operational requirements. Without feedback, however, knowledge of I_ω within this accuracy is unlikely. Therefore, if the ACS loop is not closed, satellite rates of $\omega_s = H\Delta I_\omega/I_s I_\omega$ may result.



$$\frac{\hat{T}}{\Delta\omega_c} = \frac{2I_\omega s}{\frac{2I_\omega s}{A} + 1}$$

$$\frac{\theta_s}{\theta_c} = \frac{G}{1+G} \quad \text{WHERE } G = \frac{K(Bs+1)I_\omega}{I_{sat}S^2\left(1 + \frac{2I_\omega s}{A}\right)}$$

ASSUME $T_\omega \frac{2I_\omega}{A} = 0.5$ sec, $B = 5$ sec, $\frac{I_s}{I_\omega K} = 10$ sec

DAMPING MODE: $K = 0$

Fig. 1-4. Wheel speed control loop diagram.

For $\Delta I_\omega / I_\omega = 10^{-3}$, $\omega_s = 10^{-3}$ or .05°/sec. may result.

For a turn mode at .5°/sec., a 10% error will result. Stationary constant speed operation for several minutes would result in several degrees drift unless ΔI were measured and compensated for.

Alignment

If the two wheels of a pair are misaligned by δ radians, the discharging of the wheels during eclipse could transfer $.6\delta\ H_{wheel}$ angular momentum to the satellite over 1.2 hours would result in an uncorrected rate of

$$\omega_s = \frac{.6\delta\ H_{wheel}}{(1.2)\ (3600)\ (H\ bias)}$$

For $\delta = .01° = 2 \times 10^{-4}$ rad, which appears practical for a magnetic bearing system, we get with $H_{bias} = 0.1\ H_{wheel}$, $\omega_s = .06°/1.2$ hrs. $= 1.4 \times 10^{-5}$ deg./sec. $= 2.4 \times 10^{-7}$ rad./sec., quite low. This momentum is perpendicular to the base momentum of the satellite, so the amplitude of the resulting motion is limited to $1.2\delta\ H_{wheel}/H_{bias}$. This gives .12° maximum motion, which is quite acceptable if the above alignment δ can be achieved. Parameters of the combined function flywheel system are shown in Table 1-7.

The results of the system trade-off study are shown in Table 1-8. The options for power systems are batteries I (NiCd, no discharger) and III (NiH_2, no discharger) from the power study, and the two LES flywheels with built-in momentum storage. Momentum wheels for the battery systems include four 10 ft.-lb.-sec. wheels, one 100 ft.-lb.-sec. wheel without redundancy, one 10 ft.-lb.-sec. wheel plus extra gas, and a 100 ft.-lb.-sec. wheel based on LES technology.

The results show, as expected, that all NiCd systems are very heavy. The difference in weight between the lightest NiH_2 system and the lightest LES-50 flywheel system is 44%, which shows the magnitude of payoff in technology investment here. The LES-30 flywheel is 29% lighter than a NiH_2 system with conventional wheel.

TABLE 1-7

WEIGHT AND POWER BUDGET FOR COMBINED POWER AND ACS FLYWHEELS

Assume 2 Wheels Total, with H´ = 0.1:

	34 W-H/lb.	54 W-H/lb.
Characteristics of 1 Wheel:		
O.D. of rotor, in.	20-in.	20-in.
RPM Op. range	16K-40K	20K-50K
Rotor Mass, lb.	20	20
Max. stored E, watt-hrs. (MJ)	1360 (4.90)	2160 (7.78)
M/G weight, lb.	10	20
Inertia, Kg-m^2		
Available H, net ang. momentum, ft.-lbs.-sec. (N-M-sec.)	867 (121) 89	1084 (152) 111
Mag. bearing and touchdown wt., lb.	20	20
Vac. housing, lb.	10	10
Shaft, lb.	6	6
Misc., lb.	4	4
Rotating unit wt., lb.	90	100
Available E, W-H	952	1512
Available E/M W-H/lb.	10.6	15.1
1.2 hr. discharge rate, watts	792	1260
Eclipse Budget per 2 Wheel System		
Generator efficiency (%)	96	96
Bridge efficiency (%)	92.5	92.5
Drag power from bus (W)	40	40
Suspension and control power	10	10
Output power to bus (W)	653	1069
Generating efficiency (%)	84	85
Output energy to load (W-h)	784	1282
Bridge weight .035 lb./W	21.4	34.4
Control electric weight .005 lb./W	3.0	5.0
Suspension electric weight (lb.)	5.0	5.0
Total electric weight (lb.)	29.4	44.4
Total system weight, 2 wheels	119.4	144.4
Total System E/M (W-H/lb.)	6.6	8.9

TABLE 1-7 (Cont'd)

Sun Load Budget per 2 Wheels-Charging, c/10 hr. Rate:

	34 W-H/lb.	54 W-H/lb.
Maximum drag losses (W)	40	40
Suspension and control (W)	10	10
Wheel input power (W)	96	152
Motoring efficiency, motor (%)	94.5	94.5
Motoring efficiency, bridge (%)	89.5	89.5
Total input power (W)	173	239
Charging efficiency (%)	55	64

TABLE 1-8

COMBINED ENERGY AND MOMENTUM STORAGE TRADEOFF

Assume 1.2 K-W-hr. Load Energy, 50 μft.-lb. Torques

Energy option	NiCd	NiCd	NiH_2	NiH_2	NiH_2	LL-30 X1.26	LL-50 X0.79
Momentum option	4×10 LES	100 FPS No Red.	100 FPS No Red.	10 FPS No Red.	LES 100 FPS	LL-30 × 2 Incl.	LL-50 Incl.
Battery system wt.	310	310	184	184	184	150	114
Momentum weight	80	50	50	20	15	0	0
Gas weight	0	0	0	44	0	0	0
Momentum elec. weight	20	10	10	5	10	5	5
Added structure wt.	30	10	10	5	10	0	0
Total Weight	492	432	230	234	195	155	119
Charging power, W	197	197	197	197	197	218	189
Added solar cell weight (.11 lb./W)	22	22	22	22	22	24	21
Total Weight Penalty	514	455	252	256	217	179	140

Note, however, that there are two ways to minimize weight once the NiCd battery choice is eliminated. One can go to a flywheel storage system of advanced design for the lightest option, or use the flywheel technology to build a light momentum wheel, shown as the LL 100 FPS wheel. This second option is far easier to achieve, and gives half the payoff of the lighest choice. The key parameter becomes high wheel speed, resulting in low weight. For long life, this requires magnetic bearings. Such systems are clearly available in the time frame of 1980 (see Teldix MDR momentum wheel) even with steel rotors. The addition of composite rotors then makes energy storage feasible, but this can come later.

Integration of a flywheel system as opposed to a battery and momentum wheel combination presents advantages for each. The flywheel approach represents a single subsystem to be built or purchased, tested, and integrated instead of two separate ones, representing savings in cost and manpower and perhaps resulting in more intense refinement for the same resources. However, power and attitude control now interact intimately. Probably two sets of flywheels would be desirable, one for ACS system tests and one for power system simulation. The reliability of the final system is affected both ways also in that there is only one subsystem to fail rather than two. Since failure of either would probably end the mission, this is an improvement. However, making the flywheel reliable depends upon the solution of the key design problems discussed elsewhere.

In summary, the flywheel energy and attitude control system is lighter than any other currently available alternative. It matches the expected longevity of NiH_2 batteries. It represents a large technology investment for relatively small weight improvements over NiH_2 battery systems. However, much of this technology should be developed anyway to produce lightweight, magnetically suspended momentum wheels. Therefore, the technological progress of these significantly different rotating machines can be phased into a lower-risk program with tangible short-term rewards.

It makes sense now to develop a lightweight, perhaps electronically gimballed, internally redundant high-speed momentum wheel. With that in hand, energy storage can be studied later.

II. TECHNOLOGY SURVEY

The following section details the state-of-the-art of each flywheel component.

A. Rotor

For any given system parameters, flywheel system energy density is roughly proportional to that of the rotor. The energy per unit weight which can be stored in a flywheel rotor is directly proportional to the allowable stress to density ratio obtainable in the material. For an isotropic constant strength material, such as some metals, the mathematical solution to a constant-stress optimized wheel derived by Stodola in 1924 still represents the state-of-the-art. This gives a wheel with thick hub with an exponentially thinning rim, which is truncated in various ways for a practical design. However, real materials are not uniform in allowable stress because their properties vary with thickness due to the hardening and forming processes used. Therefore, a better optimum could be realized by including this dependence in the mathematical optimization of the shape. However, there is little reason to believe this optimum will significantly improve on the present designs (8 W-H/lb. obtained with titanium Stodola wheels). One such wheel system with mechanical bearings was developed by Rockwell and delivered to NASA/Langley RC this year.

Composite filament wound materials are anistropic; their properties (strength, stiffness, etc.) vary with orientation. Tensile strength is very high in the direction of fiber length but the normal strength and shear strength are quite small. Therefore, it is possible to create thin hoop-shaped structures by filament or tape winding processes which have primarily circumferential strength. Thin hoops have been built and tested which demonstrated 80 to 90 watt-hours per pound using Kevlar. However, attempts to make the hoop radially thicker produce radial stresses in the weak direction and failure occurs at lower energy densities. This is often aggravated by locked-in thermal radial stresses due to processing problems.

The result is that disc or hollow cylinder designs tend to break radially if a significant fraction of the circumferential design strength is used. Simple solid circumferentially wound discs of Kevlar composite actually have not achieved as good an energy density as isotropic metal wheels. S-glass, which has somewhat better transverse characteristics due to a more developed method of bonding fiber to matrix, does somewhat better but is still not impressive for solid discs. Goodyear Aerospace is now working on improved matrix characteristics for Kevlar wheels.

One approach to solving this problem is to put an outer radial fiber wrap of Kevlar on the rotor after the circumferential inner hub is cured. This adds some radial strength and helps carry the radial loads on the inner matrix material. Currently, Rockwell is attempting this for NASA/Langley, so far without success beyond 5 watt-hours per pound. At present, it is not clear that the outer wrap does not create more problems than it solves by introducing discontinuities in the radial properties.

A second approach being tried is to build up a radially thick structure out of thin hoops which are discontinuous and thus strain-relieved at their interfaces. By using a number of concentric thin hoops in a bicycle-wheel shaped assembly with flexible spokes, Garrett-Airesearch Corporation has achieved an impressive 17-watt hour per pound performance on a number of Kevlar rotors storing from tens of watt-hours to several kilowatt hours. The precise method of bonding concentric rings together at Garrett is proprietary but involving preloading fiber tension and ring interference fits held together by friction. However, these structures were test devices and need to be evaluated for flight criteria. A variation of this approach using concentric rings of different properties tied together with elastomers has been plagued with dynamics problems. Dynamics problems broke the wheel-hub bond in the Garrett wheel.

A third approach is to weave the fibers in the rotor in different directions so as to give the structure strength in the radial and axial directions as well as the circumferential. This requires a 3-dimensional "polar weave" capability which General Electric's RESD facility and others have developed

for nose cones. GE has produced several Kevlar rotors of this design and expects to achieve 40 watt-hours per pound with them, but have not yet tested them beyond the 5 watt-hour per pound level. Testing to the higher level was scheduled for December, 1976. This may also be a viable solution, but is very expensive.

A fourth variation, used by AVCO and developed to about the same point over a longer period of time, builds up a radially thick flywheel by using a two-dimensional weave to get circumferential and radial strength and then laminate these together axially. These separated from the hub at 8 watt-hours/lb.

All four of these approaches are currently under test and should show 20 to 40 watt-hour per pound performance if design expectations are achieved. Many of the current tests are motivated by U. S. Army Ft. Belvoir contracts for mobile energy storage devices under the MERADCOM program.

The most promising current experiments with anistropic rotor design are being done at Johns Hopkins Applied Physics Laboratory. Using bare filament Kevlar and other materials, rotors are wound without glue on a metal hub. Spokes of the same material are wrapped through the hub and around the periphery, then glued to give some radial and axial strength to the wheel. The resulting rotor is attached to a thin shaft with a metal and rubber shock mount to allow self-centering. Results have reached 30 to 40 watt-hours per pound in this solid disc configuration, in spite of problems in bonding spokes to circumferentials. Due to the lack of glue on the circumferentials, the potential hoop strength is nearly double other designs.

In summary, the composite rotor represents a technical risk but appears well worthwhile as a weight-saving advantage and an advance in the state-of-the-art for energy storage.

B. Magnetic Bearings

The magnetic bearing represents a quantum improvement in the long-term reliability and lifetime expectancy of high-speed spinning assemblies. A combination of permanent magnetics and electromagnets is used to levitate a rotor between the poles of the magnetic bearing. The resulting structure has

no contacting surfaces to require lubrication. The bearing requires electrical power only to counteract disturbances and can be operated with no steady-state dissipation at its bias point. The bearing is limited in force density by the magnetic saturation characteristics of iron, so that size, weight and ground power are dominated by the need to support the rotor during testing in a 1G environment.

In addition, a magnetic bearing is a "soft" support in that its restoring spring constant is relatively weak compared to mechanical bearings. Therefore, such a system is characterized by clearance dimensions measured in mils or tens of mils, rather than the tens of micro-inches typical of conventional ball bearings. Such soft bearings effectively isolate rotor from mounting when imbalance vibrations occur. Also, they allow a relatively crudely balanced rotor to spin about its principal axis with minimum effect on the system performance. However, the low stiffness places limits on the allowable cross-axis spin rate which causes lateral torque on the spinning flywheel.

At present, several gyro and momentum wheel vendors are investing in magnetic bearing technology to apply these bearings to inertial navigational systems and large momentum wheels. Cambion Corporation, which invented the magnetic bearing and has accumulated a long record of innovations in this field, is retrofitting several wheels for Bendix in hopes of interesting some customers of Bendix systems in an experiment promising longer lifetimes and eventually higher speeds. Sperry-Rand Corporation, Flight Systems Division, has developed a considerable in-house magnetic bearing capability and is rapidly developing these bearings for its momentum wheels to extend their lifetime.

Most work at Sperry has been with radially passive, axially active permanent magnet systems for momentum wheels. However, the wide servo bandwidths and associated stability problems of these systems have caused recent work to be directed at 5-axis active electromagnet systems.

Aerospatiale (France) has developed a permanent magnet bearing for a momentum wheel with a composite rotor. This radially passive, axially active system has realtively high input power requirements, due in part to the imbalances from a composite rotor and in part from the many magnetic components in

this design. It includes a passive magnetic damper for oscillations about the transverse directions. This wheel design is an ambitious use of several new technologies, with a rather complex implementation. It is the most developed unit of its kind, and has been qualified for COMSAT.

Teldix (Germany) has a metal wheel with 5-axis active magnetic bearings. This allows limited magnetic gimballing of the rotor by changing the set points of the transverse position loops. The limit is the maximum gimbal angle, done to small clearance in the magnetic gaps. The MDR series wheel at 100 N-M-S has a ± 1/2° gimbal capability, and has many coils for sensors, bearings, and motor which are single-point failures. However, engineering radial wheels with 1.2° gimballing and fully redundant coils have been built (not qualified) and demonstrated automatic fault correction. The MDR wheel, flight qualified for COMSAT, appears to be a very well-engineered unit, clearly implemented and easily inspected or repaired. The bandwidth of its servo loops is set by the wheel nutation frequency, and is not too much lower than the comparable permanent magnet system due to high (16K rpm) wheel speed. Other manufacturers of high-speed rotating equipment are moving more slowly in applying these bearings.

A fundamental statement derived from Maxwell's equations, known as Earnshaw's Law, states that no static assembly of permanent magnets and ferromagnetic materials will suspend a device in stable equilibrium. This means that at least one degree of freedom of the rotor in a magnetic bearing system must be stabilized by active feedback electronics. Passively stable behavior can be obtained axially (along the spin axis) or radially (perpendicular to the spin axis) but not both. For energy storage, it appears that a passive-radial, active-axial system will allow fully redundant electronics and electromagnets to be used with a simple arrangement described in Section 4. The radially passive containment can be achieved with permanent magnets while electromagnets at each end of the shaft are used for axial stabilization. Proper design allows either electromagnet to perform the function if one should fail. Key design parameters are low weight and realization of the potential for low power. This design represents state-of-the-art engineering using Samarium-Cobalt permanent magnet materials in ways which do not exceed their limited stress capabilities.

C. Touchdown Bearings

The magnetic bearings would not be designed to withstand launch vibration and shock, power failures, or accidental test handling mishaps. These loads would be absorbed by a "touchdown" or backup ball bearing which makes no contact with the rotor under operating conditions, but prevents contact of the magnetic components and complete failure in case of mishap. This bearing will require careful design to avoid brinelling or breaking during a high-speed spin down. It must withstand high accelerations without significant deterioration. For large energy wheels, this bearing represents a development item which Sperry, Bendix, or Draper Laboratories can design with existing technology and is an engineering development item of relatively low risk. For smaller wheels, the present MIT/LL design is adequate.

D. Motor-Generator

The design of small, light, efficient motor generators is an art. This art is understood by a number of manufacturers including GE and Garrett. The key to this design is the use of Samarium-Cobalt magnets on the rotor without exceeding the stress limits on the material, and the minimization of eddy current losses in the stator windings without sacrificing efficiency. Seventy percent cycle efficiency for a 10-hour charge, 12.8 hour coast, 1.2 hour discharge is desired. Rockwell's flywheel uses a GE design and achieves adequate motor-generator performance, so there is no reason to expect a technical risk in this item. The current effort with Sperry is reported elsewhere, and is a better solution to the problem.

E. Shaft and Housing Design

The shaft and housing for the flywheel system represent a significant part of the system weight. They are to provide rigid mounting support for wheel alignment, estimated to be tens of arc seconds to avoid attitude control interaction with power demands, and also provide a vacuum enclosure for ground testing. There is no doubt that these can be built. Use of composite materials for lighter weight and perhaps flywheel failure containment will be considered but may be a technical risk.

III. ROTOR ANALYSIS

A. Orthotropic Rotor, Analytical Analysis

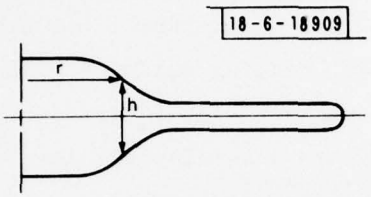


Fig. 3-1. Orthotropic rotor geometry.

Equilibrium equation:

$$\frac{d}{dr}(hr\sigma_r) - h\sigma_\theta + \rho\omega^2 hr^2 = 0$$

Compatibility equation:

$$r\frac{d\varepsilon_\theta}{dr} + \varepsilon_\theta - \varepsilon_r = 0$$

Stress-strain (plane stress):

$$\varepsilon_r = \frac{1}{E_r}(\sigma_r - \nu_r\sigma_\theta),\ \varepsilon_\theta = \frac{1}{E_\theta}(\sigma_\theta - \nu_\theta\sigma_r)$$

Introduce the stress function, ψ:

$$h_r\sigma_r = \psi,\ h\sigma_\theta = \frac{d\psi}{dr} + \rho\omega^2 hr^2$$

and eliminate ε_r, ε_θ from the compatibility equation, by means of the stress-strain relations:

$$r\frac{d}{dr}\left[\frac{1}{E_\theta}\left(\frac{1}{h}\frac{d\psi}{dr} + \rho\omega^2 r^2 - \nu_\theta\frac{\psi}{hr}\right)\right]$$

$$+ \frac{1}{E_\theta}\left(\frac{1}{h}\frac{d\psi}{dr} + \rho\omega^2 r^2 - \nu_\theta\frac{\psi}{hr}\right)$$

$$- \frac{1}{E_r}\left(\frac{1}{hr}\psi - \nu_r\frac{1}{h}\frac{d\psi}{dr} - \nu_r\rho\omega^2 r^2\right) = 0$$

If ε_θ, ε_r, ν_θ, ν_r are constants:

$$r^2\psi'' + r\psi' \left[1 - \nu_\theta + \frac{E_\theta}{E_r}\nu_r - \frac{h'}{h} r\right]$$

$$+ \psi \left[\nu_\theta \frac{h'}{h} r - \frac{E_\theta}{E_r}\right] = -\left(3 + \frac{E_\theta}{E_r}\nu_r\right) \rho\omega^2 r^3 h$$

In the general case (neglect variation of ν_θ):

$$r^2\psi'' + r\psi' \left[1 - r\frac{E'_\theta}{E_\theta} - \nu_\theta + \frac{E_\theta}{E_r}\nu_r - \frac{h'}{h} r\right]$$

$$+ \psi \left[\nu_\theta \left(\frac{h'}{h} r + r\frac{E'_\theta}{E_\theta}\right) - \frac{E_\theta}{E_r}\right]$$

$$= -\left(3 - r\frac{E'_\theta}{E_\theta} + \frac{E_\theta}{E_r}\nu_r\right) \rho\omega^2 r^3 h$$

NOTE: If $h \propto r^{\gamma_1}$, $\varepsilon_\theta \propto r^{\gamma_2}$, $\varepsilon_\theta/\varepsilon_r$ const, the equation remains equidimensional.

CASE 1: h = const. (=1), ε_θ, ε_r, ν_θ, ν_r const.

$$r^2\psi'' + r\,\psi' \left[1 - \nu_\theta + \frac{E_\theta}{E_r}\nu_r\right] - \psi\frac{E_\theta}{E_r} = -\left(3 + \frac{E_\theta}{E_r}\nu_r\right) \rho\omega^2 r^3$$

Let $\nu_r \frac{E_\theta}{E_r} = \nu_r$, $\frac{E_\theta}{E_r} = n$

$$r^2\psi'' + r\,\psi' \left[1 - \nu_\theta + \tilde{\nu}_r\right] - \psi n = -\left(3 + \tilde{\nu}_r\right) \rho\omega^2 r^3$$

Let: $Z = \ell n\ r$;

$$\psi'' + \psi' (\tilde{\nu}_r - \nu_\theta) - \eta\psi = -(3 + \tilde{\nu}_r)\ \rho\omega^2 e^{3Z}$$

$$((\ldots)' = \frac{d}{dZ}(\ldots))$$

General notation:

$$\psi = C_1 e^{\alpha_1 Z} + C_2 e^{\alpha_2 Z} - \frac{(3+\tilde{\nu}_r)\rho\omega^2\ e^{3Z}}{9+3(\tilde{\nu}_r-\nu_\theta)-\eta}$$

$$\alpha_1 = \frac{1}{2}(\nu_\theta - \tilde{\nu}_r) + \sqrt{\frac{1}{4}(\nu_\theta-\tilde{\nu}_r)^2 + \eta}$$

$$\alpha_2 = \frac{1}{2}(\nu_\theta - \tilde{\nu}_r) - \sqrt{\frac{1}{4}(\nu_\theta-\tilde{\nu}_r)^2 + \eta}$$

or

$$\psi = C_1 r^{\alpha_1} + C_2 r^{\alpha_2} - \frac{(3+\tilde{\nu}_r)\ \rho\omega^2}{9 + 3(\tilde{\nu} - \nu_\theta) - \eta}\ r^3$$

ψ finite at $r = 0$ $\Longrightarrow$ $C_2 = 0$

$\psi = 0$ at $r = a$ $\Longrightarrow$ $C_1 = \dfrac{(3+\tilde{\nu}_r)\ \rho\omega^2}{9 + 3(\tilde{\nu}_r-\nu_\theta) - \eta}\ a^{3-\alpha_1}$

Hence:

$$\psi = \beta((r/a)^{\alpha_1} - (r/a)^3)$$

$$\beta = \frac{(3+\tilde{\nu}_r)\ \rho\omega^2\ a^3}{9 + 3(\tilde{\nu}_r-\nu_\theta) - \eta}$$

and:

$$\sigma_r = \frac{\beta}{r}[(r/a)^{\alpha_1} - (r/a)^3]$$

$$\sigma_\theta = \frac{\beta}{a}[\alpha_1(r/a)^{\alpha_1-1} - 3(r/a)^2] + \rho\omega^2 r^2$$

$$\alpha_1 = \frac{1}{2}(\nu_\theta \tilde{\nu}_r) + \sqrt{\frac{1}{4}(\nu_\theta - \tilde{\nu}_r)^2 + \eta}$$

$$\beta = \frac{(3+\tilde{\nu}_r)\ \rho\omega^2 a^3}{9 + 3(\tilde{\nu}_r - \nu_\theta) - \eta}$$

$$\tilde{\nu}_r = \nu \frac{E_\theta}{E_r} \quad , \quad \eta = E_\theta/E_r$$

B. Bare Filament Rotor Analysis

1. Basic Assumptions

The configuration of a bare Kevlar fiber flywheel under steady rotation is determined in this section. It is supposed that the evenly-spaced radial spokes are inextensible, although the following analysis may be readily extended to include spoke compliance. Furthermore, the individual fibers composing the circumferential windings are assumed to be mutually noninteracting (i.e., no contact or friction forces are generated between fibers) so that they may be considered separately. Finally, each fiber is approximately a homogeneous elastic string with zero torsional and bending rigidity.

In the next section, the equations for the steady rotary motion of a string are assembled and the boundary conditions for the bare fiber flywheel are derived. Next, the approximation which neglects the compliance of the fibers is justified, and explicit results are obtained for the configuration and tension distribution. After presenting certain useful approximations, we conclude with a calculation of the loads imposed on the spokes by circumferential windings.

2. Equations of Steady Rotary Motion

Following Ref. (1), the general equations of motion of a homogeneous elastic string may be listed as follows:

$$\frac{\partial}{\partial s}\left(T\,\frac{\partial x^i}{\partial s}\right) - m\left(\frac{\partial}{\partial t} + u\,\frac{\partial}{\partial s}\right)\left(\frac{\partial x^i}{\partial t} + u\,\frac{\partial x^i}{\partial s}\right) + F^i = 0 \qquad (3\text{-}1.a)$$

Tangent Identity

$$\frac{\partial x^i}{\partial t} + \frac{\partial x^i}{\partial s} = 1 \qquad (3\text{-}1.b)$$

Mass Conservation Equation

$$\frac{\partial m}{\partial t} + \frac{\partial (mu)}{\partial s} = 0 \qquad (3\text{-}1.c)$$

Stress-Strain Relation

$$m = m_o \exp(-kT) \qquad (3\text{-}1.d)$$

where we define:

s $\triangleq$ arclength of stretched string (measured from an attachment point)

s_o $\triangleq$ arclength of unstretched string

x^i $\triangleq$ inertial position vector of a string point

u $\triangleq$ tangential component of velocity of string point at fixed s_o relative to a point at fixed s.

m $\triangleq$ lineal mass density of stretched string

$m_o = m(T=0)$ $\triangleq$ lineal denstiy of unstretched string

T $\triangleq$ tension

k $\triangleq$ axial compliance of string material

and where F^i is the externally applied force per unit length. Since the interaction of each fiber with other fibers is neglected, $F^i = 0$ in this analysis. Also note that the stress-strain relation implies the use of the logarithmic or natural strain and is valid for finite strain.

Consider the steady rotary motion of the flywheel with angular speed Ω about the flywheel axis. In this case, each fiber will lie in a plane normal to the rotation axis. Because the motion is steady, u vanishes and, according to the mass conservation relation, m is independent of time. The acceleration of a string point thus becomes:

$$\frac{\partial^2 x^i}{\partial t^2} = -\Omega^2 x^i$$

Adopting polar coordinates (r, ϕ) in a plane rotating with the flywheel, the equations of motion become (see Reference (2) for comparison).

Radial Momentum:

$$(Tr')' - Tr\phi'^2 + m\Omega^2 r = 0 \qquad (3\text{-}2.a)$$

Circumferential Momentum:

$$[Tr^2\phi'] = 0 \qquad (3\text{-}2.b)$$

Tangential Momentum:

$$T' + m\Omega^2 rr' = 0 \qquad (3\text{-}2.c)$$

Tangent Identity:

$$r'^2 + r\phi'^2 = 1 \qquad (3\text{-}2.d)$$

Stress-Strain Relation:

$$m = m_o \exp(-kT) \qquad (3\text{-}2.e)$$

Also, from mass conservation, we have:

$$\frac{\partial s}{\partial s_o} = \frac{m_o}{m} \qquad (3\text{-}2.f)$$

Finally, it is most convenient to adopt ϕ, rather than s, as the independent variable. Using the tangent identity:

$$\frac{d\phi}{ds} = \frac{1}{\sqrt{r^2 + \left(\frac{dr}{d\phi}\right)^2}}$$

the momentum equatiors become:

$$\frac{d}{d\phi}\left[Tr^2 \frac{}{\sqrt{r^2 + \left(\frac{dr}{d\phi}\right)^2}}\right] = 0 \qquad (3\text{-}3.a)$$

$$\frac{dT}{d\phi} + m\Omega^2 r \frac{dr}{d\phi} = 0 \qquad (3\text{-}3.b)$$

where the radial momentum equation may be omitted since it is merely a combination of the circumferential and tangential equations. Note also that the element of unstretched length, ds_o, is obtained by combining (2.f) with the relation for $\frac{d\phi}{ds}$:

$$ds_o = \frac{m}{m_o}\sqrt{r^2 + \left(\frac{dr}{d\phi}\right)^2}\, d\phi \qquad (3\text{-}3.c)$$

Relations (3), along with the stress-strain relation, (2.e), constitute a complete set of equations for each fiber.

To derive the appropriate boundary conditions, consider a single fiber attached at radial distance r_o along the neighboring spokes. Referring to Fig. 3-2, we define:

Φ = angle between spokes (a submultiple of 2π)

L = unstretched length between spokes

Because of symmetry of the fiber configuration about $\phi = \Phi/2$:

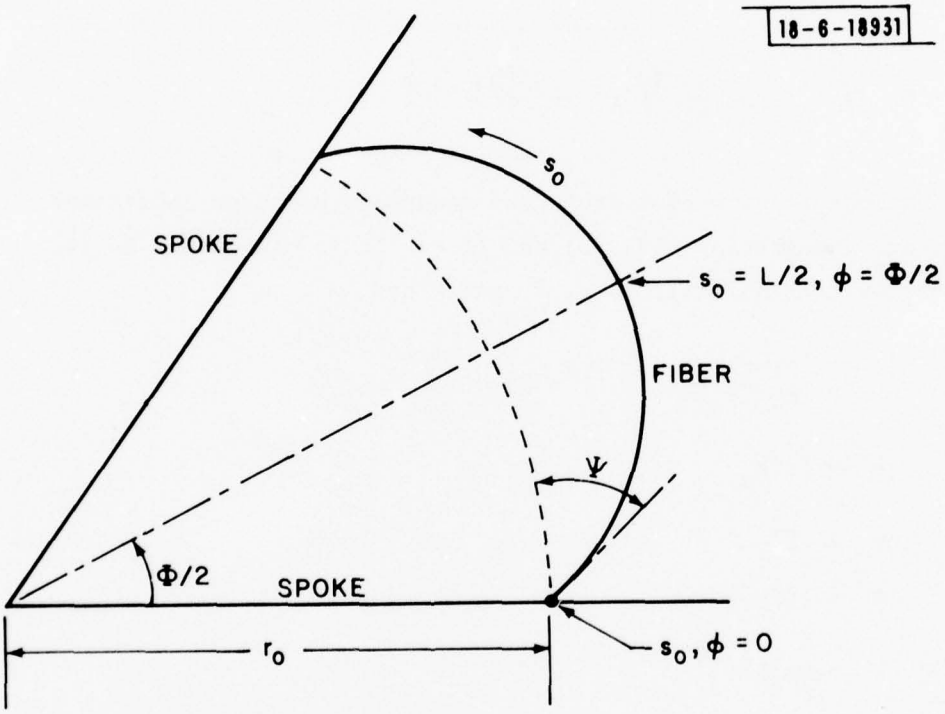


Fig. 3-2. Single fiber configuration.

$$\phi = 0 \quad : \quad r = r_o \tag{3-4.a}$$

$$\phi = \Phi/2 \quad : \quad \frac{dr}{d\phi} = 0 \tag{3-4.b}$$

In addition, the total unstretched length must be constrained to be L. From (3.c):

$$\int_o^{\Phi/2} d\phi \, \frac{m}{m_o} \sqrt{r^2 + \left(\frac{dr}{d\phi}\right)^2} = \frac{L}{2} \tag{3-4.c}$$

Equations (4) now constitute the necessary boundary conditions.

Before integrating Eqs. (3) and (2.e), it is convenient to define the dimensionless variables τ, r, v, ℓ, and κ by:

$$\begin{aligned} \tau &= \frac{T}{m_o \Omega^2 r_o^2} \\ \tilde{r} &= r/r_o \\ v &= \tilde{r}^2 \\ \ell &= L/r_o \Phi \\ \kappa &= k m_o \Omega^2 r_o^2 \end{aligned} \tag{3-5}$$

Clearly, τ and κ are the dimensionless tension and compliance while ℓ is the ratio of the total length to the arclength of a circular arc between the spokes. It is expected that as a result of the fibrication process, there will be excess fiber so that $\ell - 1 > 0$.

In terms of the dimensionless variables, the governing equations and boundary conditions become:

$$\frac{d}{d\phi} \left\{ \frac{\tau v}{\sqrt{v + \frac{1}{4v} \left(\frac{dv}{d\phi}\right)^2}} \right\} = 0 \tag{3-6.a}$$

$$\frac{d}{d\phi}\left\{\frac{1}{\kappa}\, e^{\kappa\tau} + \frac{1}{2}\, v\right\} = 0 \qquad (3\text{-}6.b)$$

$$\phi = 0 \quad : \quad v = 1 \qquad (3\text{-}6.c)$$

$$\phi = \frac{\Phi}{2} \quad : \quad \frac{dv}{d\phi} = 0 \qquad (3\text{-}6.d)$$

$$\int_0^{\Phi/2} d\phi \;\; e^{-\kappa\tau} \sqrt{v + \frac{1}{4v}\left(\frac{dv}{d\phi}\right)^2} = \ell\Phi/2 \qquad (3\text{-}6.e)$$

3. Solution of the Inextensible Case

Note that the term $\kappa\tau$ is the axial strain. Supposing that $\tau\kappa < M$, $M > 0$, Eqs. 6(b) and 6(c) become, upon rearrangement:

$$\frac{d}{d\phi}\left\{\tau(1 + \alpha_1) + \frac{1}{2}\, v\right\} = 0$$

$$\frac{2}{\Phi}\int_0^{\Phi/2} d\phi \sqrt{v + \frac{1}{4v}\left(\frac{dv}{d\phi}\right)^2} = \ell(1 + \alpha_2)$$

where α_1 and α_2 are both positive and:

$$\alpha_1 < \frac{1}{M}\,(e^M - 1 - M)$$

$$\alpha_2 < M$$

Since the strain at failure for KEVLAR 29 is less than four percent, $M < .04$ and

$$\alpha_1 < .02$$

$$\alpha_2 < .04$$

Thus, as a first approximation, terms of the order of the compliance may be neglected and the fiber treated as inextensible.

With this approximation, Eqs. 6(a) and 6(b) may be integrated to give:

$$\tau = \tau_o + \frac{1}{2}(1-v) \qquad \text{(a)}$$

$$\frac{\tau v}{\sqrt{v + \frac{1}{4v}\left(\frac{dv}{d\phi}\right)^2}} = \tau_o \cos\psi \qquad \text{(b)} \qquad (3\text{-}7)$$

where:

$\tau_o \triangleq \tau(\phi = 0)$

$\psi \triangleq$ angle between the tangent and the ϕ direction at $\phi = 0$.

Elimination of τ from Eq. (7) gives the equation determining $v(\phi)$:

$$\left(\frac{dv}{d\phi}\right) = \frac{v^2}{\tau_o^2 \cos^2\psi} F(v) \qquad \text{(a)}$$

$$F(v) = \left[4\, v(\tau_o + \frac{1}{2}(1-v))^2 - \tau_o^2 \cos^2\psi\right] \qquad \text{(b)} \qquad (3\text{-}8)$$

$$= (v - v_1)(v_2 - v)(v_3 - v)$$

$$v_1 \leq v_2 \leq v_3$$

The roots, v_1, v_2, and v_3 of $F(v)$ determine the extrema of the string curve and may be evaluated iteratively from the expressions

$$v_{1,2} = 1 + \frac{2\tau_o}{4\tau_o - 1}\left\{\tau_o - 1 \mp \sqrt{(\tau_o-1)^2 + (4\tau_o-1)\left(\sin^2\psi + \frac{1}{4}\frac{(v_{1,2}-1)^3}{\tau_o^2}\right)}\right\} \qquad \text{(a)}$$

$$v_3 = 4\tau_o - 4\frac{\tau_o(\tau_o-1)}{v_3 - 1} - 4\frac{\tau_o^2 \sin^2\psi}{(v_3 - 1)^2} \qquad \text{(b)} \qquad (3\text{-}9)$$

to yield the numerical results shown in Fig. 3-3.

It is seen from 8(a) that $\frac{dv}{d\phi}$ is defined only for $v \in [v_1, v_2]$ and $v \geq v_3$. Since the latter possibility corresponds to an unbounded string curve, it must be discarded. Furthermore, Fig. 3-3 shows that $v_1 < 1$ and $v_2 > 1$. Thus, in view of the boundary conditions 6(c) and 6(d), the string curve must be confined to $v \in [1, v_2]$, and 6(d) merely implies that $v(\phi = \Phi/2) = v_2$.

Integrating 8(a) and expressing ϕ as a function of v, we have

$$\phi = \tau_o \mathrm{Cos}\psi \int_1^v \frac{dx}{x\sqrt{F(x)}} \text{ , or (Ref. 3, p. 227):}$$

$$\phi = \frac{2\tau_o \mathrm{Cos}\psi}{v_1\sqrt{v_3-v_1}} \left\{ \Pi\left(\sin^{-1}\sqrt{\frac{v-v_1}{v_2-v_1}}\ ,\ 1-\frac{v_2}{v_1}\ ,\sqrt{\frac{v_2-v_1}{v_3-v_1}} \right) \right.$$

$$\left. - \Pi\left(\sin^{-1}\sqrt{\frac{1-v_1}{v_2-v_1}}\ ,\ 1-\frac{v_2}{v_1}\ ,\sqrt{\frac{v_2-v_1}{v_3-v_1}} \right) \right\} \qquad (3\text{-}10)$$

where $\Pi(\phi, n, k)$ is the elliptic integral of the third kind. The condition $v(\phi = \Phi/2) = v_2$ gives:

$$\frac{\Phi}{2} = \frac{2\tau_o \mathrm{Cos}\psi}{v_1\sqrt{v_3-v_1}} \left\{ \Pi\left(\frac{\pi}{2}\ ,\ 1-\frac{v_2}{v_1}\ ,\sqrt{\frac{v_2-v_1}{v_3-v_1}} \right) \right.$$

$$\left. - \Pi\left(\sin^{-1}\sqrt{\frac{1-v_1}{v_2-v_1}}\ ,\ 1-\frac{v_2}{v_1}\ ,\sqrt{\frac{v_2-v_1}{v_3-v_1}} \right) \right\} \qquad (3\text{-}11)$$

This provides one relation with which to determine τ_o and ψ. The second relation is Eq. 6(e) which, when the compliance is neglected, becomes:

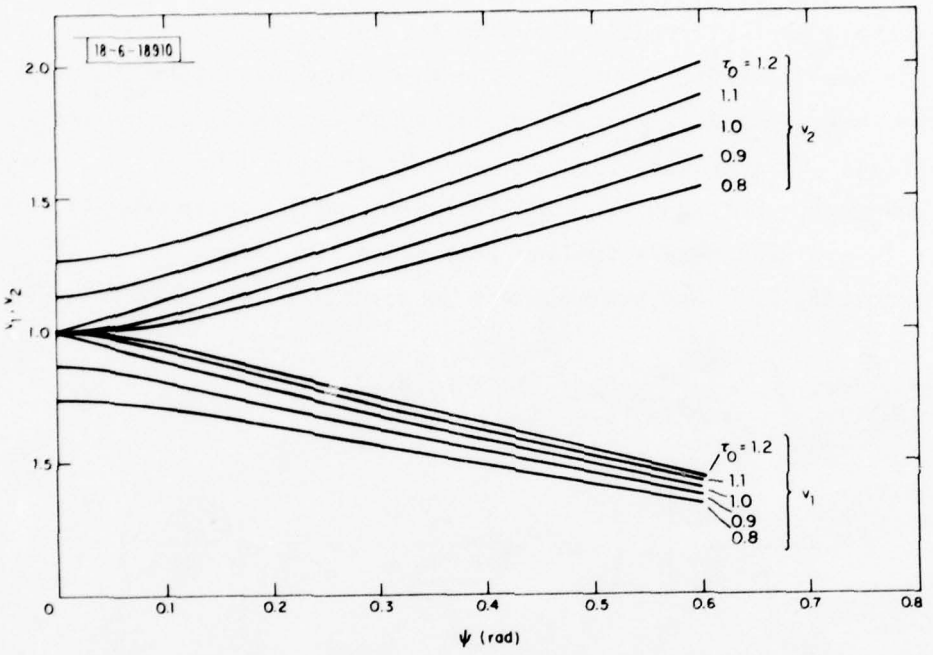


Fig. 3-3a. Smallest and intermediate roots of F(v) = 0.

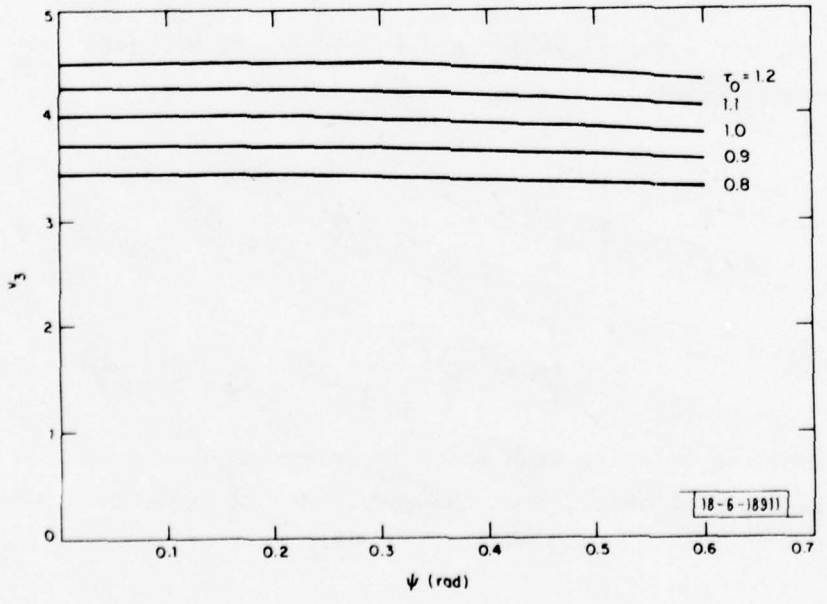


Fig. 3-3b. Largest root of F(v) = 0.

$$\frac{2}{\Phi}\int_{1}^{v_2} dv\ \frac{\tau_o + \frac{1}{2}(1-v)}{\sqrt{(v_3-v)(v_2-v)(v-v_1)}} = \ell$$

Or, (Ref. 3, pp. 219-220):

$$\left(\tau_o + \frac{1}{2}(1-v_3)\right)\ F(\delta, q) - \frac{1}{2}(v_2-v_3)\ \Pi(\delta, q^2, q)$$

$$= \frac{1}{4}\ \ell\Phi\ \sqrt{v_3-v_1} \qquad (3\text{-}12)$$

where:

$$\delta \triangleq \sin^{-1}\sqrt{\frac{(v_3-v_1)(v_2-1)}{(v_2-v_1)(v_3-1)}}$$

$$q \triangleq \sqrt{\frac{v_2-v_1}{v_3-v_1}}$$

and where $F(\delta, q)$ is the elliptic integral of the first kind.

The quantities τ_o and ψ, determined by (11) and (12), are of importance since τ_o is the maximum tension in the string (see Eq. 7(a)) while the radial load applies to the spokes, $\tau_o \sin\psi$, is proportional to both τ_o and ψ.

4. Approximate Evaluation of τ_o and ψ

To obtain useful approximate results, note that when ℓ is $\underset{\sim}{>} 1$, v_2 is also $\underset{\sim}{>} 1$, and the factor v_3-x in the integrands leading to (11) and (12) can be approximated by (v_3-1). Thus, for $|\ell-1| << 1$, the conditions $v(\phi = \Phi/2) = v_2$ and 6(e) become approximately:

$$\frac{\Phi}{2} \simeq \tau_o \cos\psi \frac{1}{\sqrt{v_3-1}} \int_1^{v_2} \frac{dx}{x\sqrt{(v_2-x)(x-v_1)}}$$

$$2\int_1^{v_2} dx \frac{\tau_o + \frac{1}{2}(1-x)}{\sqrt{(v_2-x)(x-v_1)}} \simeq \ell\Phi \sqrt{v_3-1}$$

Or, evaluating the integrals:

$$\frac{\Phi}{2} = \tau_o \cos\psi \frac{1}{\sqrt{v_1 v_2 (v_3-1)}} \left\{ \frac{\pi}{2} - \sin^{-1}\left(\frac{v_1+v_2-2v_1v_2}{v_2-v_1}\right) \right.$$

$$\left. 2\left(\tau_o + \frac{1}{2}\left(1 - \frac{v_1+v_2}{2}\right)\right)\left[\frac{\pi}{2} + \sin^{-1}\left(\frac{v_1+v_2-2}{v_2-v_1}\right)\right] = \ell\Phi \sqrt{v_3-1} + \sqrt{(v_2-1)(1-v_1)} \right.$$

(3-13)

These relations may be further simplified by approximately v_1, v_2, and v_3. With $|\ell-1| << 1$, both $|\tau_o-1|$ and ψ are also small, and Eq. (9) give as a first approximation:

$$v_1 \simeq 1 + \Delta - \varepsilon \qquad \text{(a)}$$

$$v_2 \simeq 1 + \Delta + \varepsilon \qquad \text{(b)}$$

where $$\Delta = \frac{2}{3}(\tau_o - 1) \qquad \text{(c)} \qquad \text{(3-14)}$$

$$\varepsilon = \frac{2}{3}\sqrt{(\tau_o-1)^2 + 3S.^2\psi} \qquad \text{(d)}$$

$$v_3 \simeq 4$$

Expressing τ_o and ψ as well as v_1 and v_2 in terms of Δ and ε and substituting (14) into Eq. (13), we finally obtain:

$$\tau_o \simeq 1 + \frac{3}{2}\Delta \qquad \text{(a)}$$

$$\sin\psi \simeq \sqrt{\frac{3}{2}}\sqrt{\varepsilon^2 - \Delta^2} \qquad \text{(b)}$$

with Δ and ε determined by

$$\varepsilon = \frac{C_1 - C_2}{1 - C_2^2} \qquad \text{(c)}$$

$$\Delta = -C_2\varepsilon \qquad \text{(d)} \qquad (3\text{-}15)$$

where

$$C_1 = \cos\frac{\Phi}{2}\,\frac{\sqrt{3\ (1+\Delta)^2 - \varepsilon^2}}{(1+\frac{3}{2}\Delta)\ \sqrt{1-\frac{3}{4}(\varepsilon^2-\Delta^2)}} \qquad \text{(e)}$$

$$C_2 = \cos\frac{\ell\Phi\ \sqrt{3} + \sqrt{\varepsilon^2 - \Delta^2}}{2(1+\Delta)} \qquad \text{(f)}$$

Numerical results for τ_o and ψ as functions of the excess length $(\ell-1)$ are shown in Fig. 3-4 for 4, 5, and 6 spokes (i.e., $\Phi = \frac{\pi}{2}, \frac{2}{5}\pi, \frac{\pi}{3}$ radians, resp.). Although the accuracy degrades somewhat above $(\ell-1) \sim .2$, these curves still reflect the correct qualitative trends. It is seen that the attachment angle, ψ, is roughly the same for all values of Φ considered. As should be expected, the maximum tension τ_o falls below 1 for small $(\ell-1)$ and ultimately rises above this value for sufficiently large $(\ell-1)$. Although the maximum τ_o is seen to decrease somewhat with increasing number of spokes, $\tau_o \simeq 1$ (which

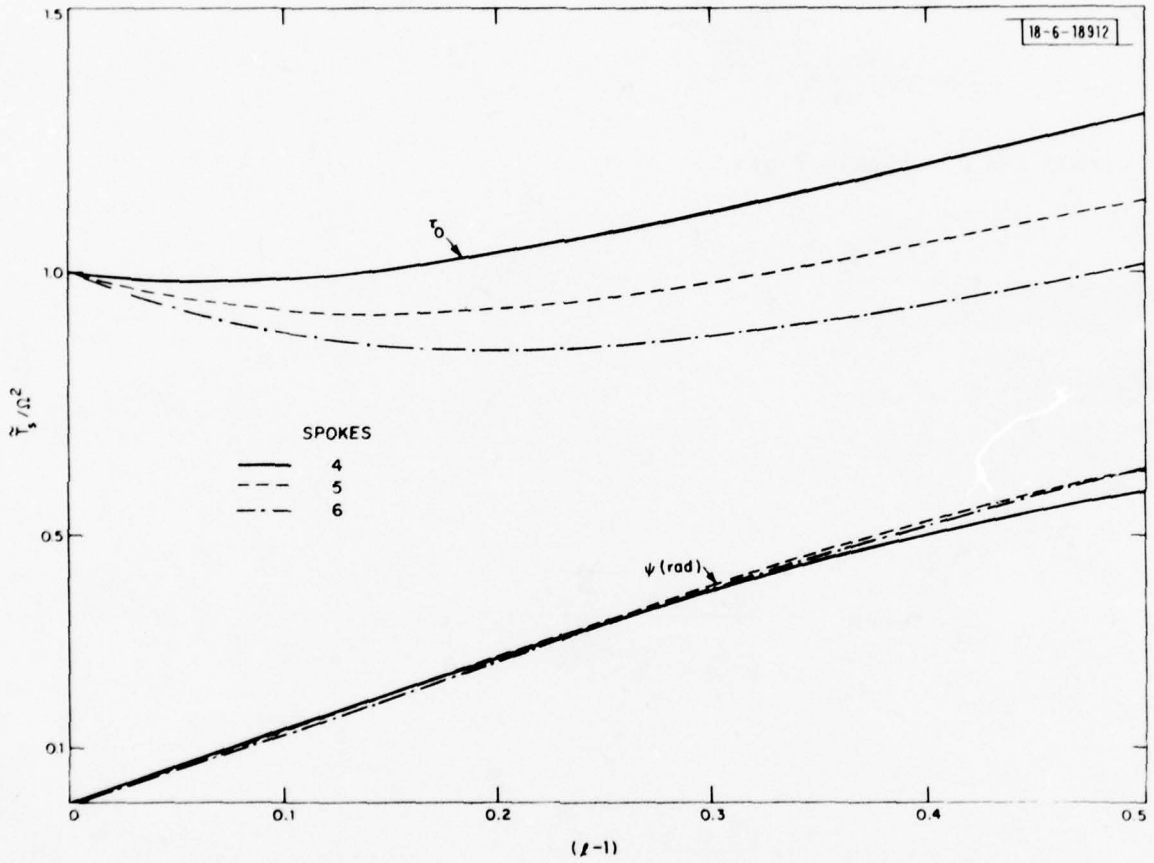


Fig. 3-4. Maximum tension and attachment angle.

corresponds to the "hoop" stress of a circular arc of string) is still a reasonable approximation over the range of parameters considered.

5. Computation of Spoke Loads

Before calculating the loads applied by the fibers to the spokes as a result of Eq. (15), we must first determine the unstretched length of all fiber segments between the spokes. When the spokes are completed and the end-plates used during fabrication are removed, the lateral surfaces of the spokes must support a load due to the circumferential windings. This lateral load causes the spokes to thicken along the flywheel axis with a corresponding decrease in the radial extent of the spokes. It is reasonable to assume that the radial position of attachment of each fiber segment decreases proportionally. That is, if:

$\bar{r}_o(n) \triangleq$ radius of n^{th} winding during fabrication

$r_o(n) \triangleq$ final radius of n^{th} winding (at $\Omega = 0$)

than our assumption is that $\frac{1}{\bar{r}_o(n)} (\bar{r}_o(n) - r_o(n))$ is the same for all windings. Thus, the unstretched length, L(n), of a fiber segment belonging to the n^{th} winding is $\Phi\bar{r}_o(n)$, and the dimensionless quantity becomes:

$$\ell(n) = \ell, \text{ independent of } n.$$

With this assumption, both the dimensionless tension τ and the attachment angle ψ are the same for all fiber segments. The tension in a fiber at its point of attachment to a spoke is then:

$$m_o \Omega^2 r_o^2 \tau_o(\ell, \Phi)$$

so that the total radial force on the spoke due to one fiber is:

$$2 \sin\psi m_o \Omega^2 r_o^2 \tau_o(\ell, \Phi)$$

so that the total radial force on the spoke due to one fiber is:

$$2\mathrm{Sin}\psi m_o \Omega^2 r_o{}^2 \tau_o(\ell, \Phi)$$

If the circumferential fibers are held in a hexagonal close-packed pattern by the spokes, the number of fibers per unit cross-sectional area of the fiber pack is $\frac{2}{\sqrt{3}} \frac{1}{d_f{}^2}$, where d_f is the fiber diameter.

Consequently, the total radial load, F_r, applied to a spoke per unit radial distance is:

$$F_r = \frac{4}{\sqrt{3}} \frac{h_w}{d_f{}^2} m_o \Omega^2 r_o{}^2 S.\psi \tau_o(\ell, \Phi) \qquad (3\text{-}16)$$

where:

$r_o \triangleq$ radial coordinate along spoke

$h_w \triangleq$ thickness of flywheel

$d_f \triangleq$ fiber diameter

The total radially directed force resultant, T_s, developed over spoke cross-sections as a result of the above load distribution may be determined from:

$$\frac{dT_s}{dr_o} + F_r + M_s \Omega^2 r_o = 0$$

$$r_o \epsilon \ [R_H, R_w] \qquad (3\text{-}17)$$

$$T_s(r_o = R_w) = 0$$

where:

$T_s \triangleq$ force resultant over spoke cross-section

$M_s \triangleq$ mass of spoke per unit length

$R_w \triangleq$ flywheel radius

$R_H \triangleq$ radial coordinate of hub-spoke attachment.

Substituting relation (16) for F_r, Eq. (17) yields:

$$T_s(r_o) = \frac{1}{2} M_s \Omega^2 (R_w^2 - r_o^2)$$

$$+ \frac{4}{3\sqrt{3}} \frac{h_w}{d_f^2} m_o \Omega^2 (R_w^3 - r_o^3) \, \mathrm{Sin}\psi\tau_o(\ell, \Phi) \qquad (3\text{-}18)$$

Thus, the total load applied to the hub by one spoke is $T_s(r_o = R_H)$.

The first term in (18) results from the centrifugal loading only and the corresponding tension in individual spoke fibers is no more than half the "hoop" tension, $m_o \Omega^2 R_w^2$, developed in the outer circumferential fibers. Thus, it is the second term in (18), representing circumferential fiber loading, that significantly degrades the maximum energy density below the optimum. Denoting by $\widetilde{T}_s$ the contribution of this term to the total load applied to the hub, we have:

$$\widetilde{T}_s = \frac{4}{3\sqrt{3}} \frac{h_w}{d_f^2} m_o \Omega^2 (R_w^3 - R_H 3) \, \mathrm{Sin}\psi\tau_o(\ell, \Phi) \qquad (3\text{-}19)$$

Assuming the following typical values:

$R_w = 9$ in., $R_H = 2$ in.

$h_w = \frac{1}{2}$ in., $d_f = 15$ mil

fiber density $= .052$ lbm/in^3

Figure 3-5 shows T_s/Ω^2 as a function of $(\ell\text{-}1)$ for 4, 5, and 6 spokes. It is seen that while some slight advantage is derived by increasing the number of spokes, the only effective way to eliminate $\widetilde{T}_s$ is to reduce the excess length, $(\ell\text{-}1)$, as far as possible.

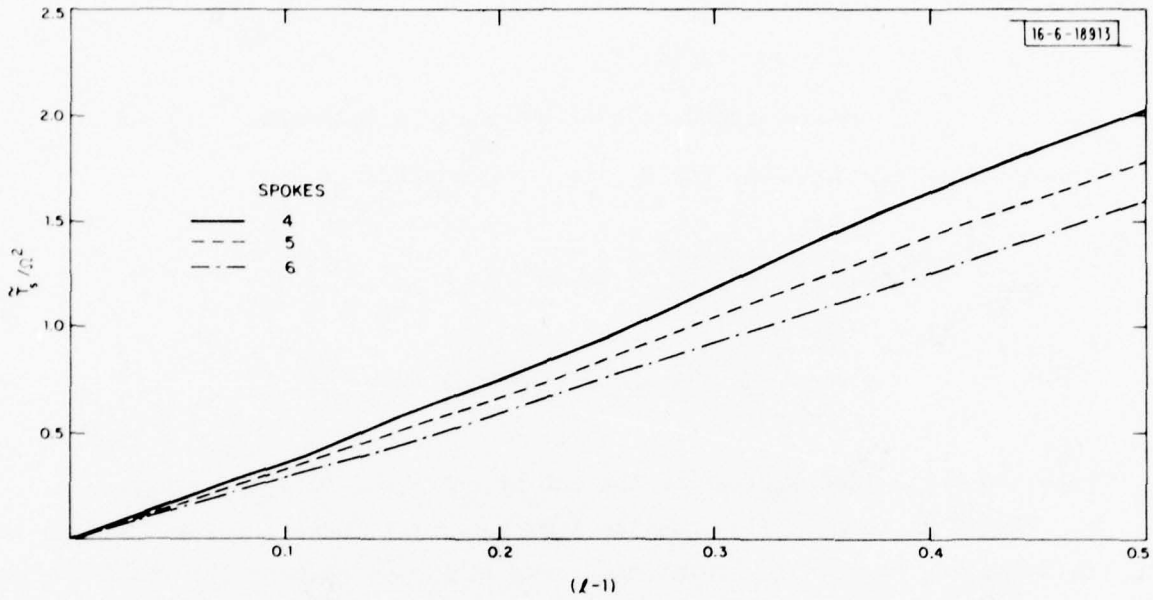


Fig. 3-5. Contribution of circumferential fiber loads to total load applied to the hub.

6. Conclusions

The above analysis shows that both the fiber configuration and tension depend primarily on the "excess length" of the fiber segments (i.e., the difference between the true length and the length of a circular arc joining the fiber-spoke attachment points). While the maximum tension decreases somewhat with increasing number of spokes, it is still of the order of the "hoop" tension, $m_o\Omega^2 r_o^2$. Furthermore, the angle formed between a fiber and the circumferential direction at a spoke is nearly independent of the number of spokes and linearly dependent on the excess length.

Since the excess length ultimately produces significant loading of the spokes, flywheel optimization depends on the maximum reduction of this quantity.

REFERENCES

1. E. Yhland, "Contributions to the Dynamics of Flexible Strings," Gothenburg, Sweden. Trans., No. 32, (1961). Chalmers University of Technology.

2. H. W. Hall and W. Hunter, "On the Form Assumed by a Steadily Rotating Thread," The London, Edinburgh, and Dublin Philosophical Magazine and J. Sci., Series 7, (February, 1938).

3. I. S. Gradshteyn and I. M. Ryzhik, Tables of Integrals, Series, and Products, (Academic Press, 1965).

IV. MAGNETIC BEARING INVESTIGATION

A design layout of the MIT/LL magnetic bearing test bed system is shown in Fig. 4-1. It consists primarily of magnetic bearings (stators and rotors), touchdown bearings, motor-generator, turbine-flywheel, shaft, position sensor, and test bed support.

The following sections are the supporting design calculations for the magnetic bearing brassboard and descriptions of other related work.

A. Mechanical Design Concept

The prototype energy storage wheel assembly consists of rotor, shaft, two magnetic bearing assemblies, two touch-down ball bearing assemblies, a motor generator assembly and a base support structure. A conventional rotating shaft spindle configuration vs. fixed shaft was chosen for the prototype model as shown in Fig. 4-1. The rotor was designed to simulate the mass of a flight configured wheel, but not the inertia. The rotor weighs 15 pounds and was made from nonmagnetic stainless steel. The shaft is 16 inches long, 1-1/4 inches in diameter at the center section and 1/2 inch in diameter at the ends. The shaft is also made from nonmagnetic stainless steel. The ratio of inertia of the rotating assembly, axial vs. transverse, is less than one and could result in stability problems. Preliminary tests at low speed have shown that this is not a problem with the test setup. In a real system this ratio will be greater than one and thus stable.

The stator of the magnetic bearing, which contains the Samarium Cobalt ($SmCO_5$) magnets and the coils, is mounted to the fixed base structure. The stator is made from high silicon low chromium steel for its high magnetic permeability. The magnetic bearing section of the rotor is made from 4130 carbon steel.

The magnetic gap in the axial direction is 0.015 inch and travel is limited in both the axial and transverse directions by the touchdown ball bearing assemblies. The touchdown bearings engage with 0.010 inch travel and protect the magnetic bearings from rubbing contact within themselves.

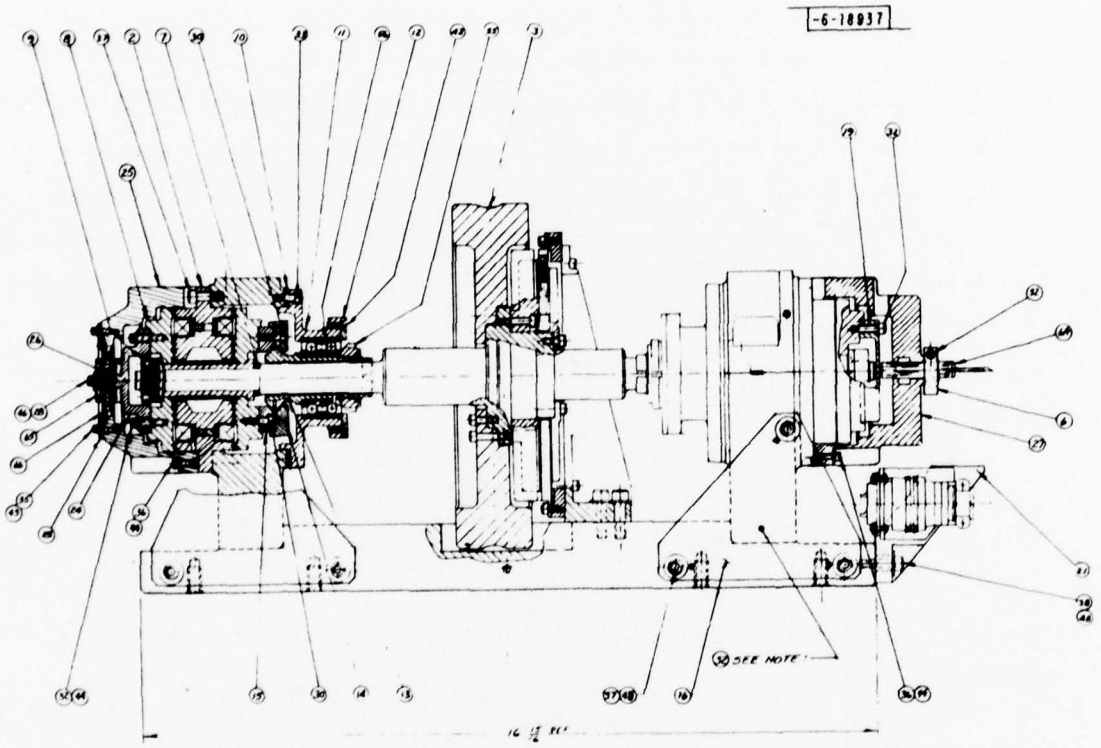


Fig. 4-1. Design layout of magnetic bearing test bed.

The ball bearing assemblies are a duplex pair with a twelve pound preload separated by a distance of 10 inches. The inertia of the rotating element of the touchdown bearing assembly was minimized so that its acceleration rate during touchdown at high speeds will be very high and thus minimize scuffing on the balls.

The male touchdown stud was made from nonmagnetic steel and the rotating female pieces from leaded bronze. The bearings were high speed, duplex turbine bearings purchased from Barden Corporation.

The geometry of the touchdown elements are bi-conical at 45° to achieve touchdown in either the axial or transverse directions with the same linear travel. The bi-conical feature of the touchdown elements limited the coning of the shaft and maintained normal alignment at the extreme axial displacement. The problem of fabrication tolerances of the touchdown elements was controlled by manufacturing matched sets and providing for shimming at assembly. Assembly measurements were recorded and the shims ground to size to maintain the specified clearance of 0.01 inch within ± .001 in.

The base structure consists of an aluminum bottom plate and two stanchions which are bolted and pinned to the base. The stanchions are split at the spin axis to facilitate assembly without removing the stanchions from the base. The base assembly was prematchined and then assembled and final machined as an integral unit to maintain alignment of the axis. The base structure is made from 6061-T6 aluminum.

The motor generator was purchased from Sperry Electro Components, Durham, North Carolina. The unit is a brushless DC motor-generator with an ironless armature and a 0.015 inch axial airgap. The motor-generator consists of three components, armature, return path and permanent magnet rotor. The armature is supported to the base structure by an aluminum bracket. The "return path" and permanent rotor are supported to the shaft as shown in Fig. 4-1.

The return path is made from high strength stainless steel. The permanent magnet rotor support is made from titanium.

Based on dynamic considerations the elements of the assembly were designed for high stiffness within the constraints of the basic configuration. The desired natural frequency of the individual elements was above 1 kHz, a rather

ambitious goal. The low natural frequency of the shaft (154 Hz) was a result of placing the touchdown bearings inboard of the magnetic bearings. It was recognized that some frequency tuning might be required during testing to avoid particularly troublesome frequency bands.

The conventional rotating slender shaft configuration is not the optimum configuration with respect to stiffness from practical considerations. The fixed shaft configuration offers an advantage in this respect and should be considered in advanced designs.

The rotor of the magnetic bearing assembly must react a magnetic force of approximately 200 pounds. The deflection of the rotor due to this force is 0.0006 inch. Under normal operation with the magnetic bearing centered, the axial forces on the rotor are small. The axial force is a function of the rotor-stator clearance, at the mid-position the force is small and increases to a maximum as the gap is decreased.

The stator of the magnetic bearing assembly is inherently stiff with respect to both the inner and outer pole pieces prior to assembly. Fasteners were not permitted in the assembly of this unit to minimize energy losses. The outer pole pieces were assembled by means of a shrink fit with the two structural members.

The Samarium Cobalt ($SmCO_5$) magnets were purchased from Spectraflex, Inc., located in Watsonville, California. The individual magnets were premachined and magnetized prior to assembly into the outer pole piece. The outer pole pieces were fabricated at Lincoln Laboratory and sent to Spectraflux to have the magnets installed. After bonding the magnets to the pole piece, the inside diameter of the outer magnets was ground for 0.001 inch diametrical clearance with the inner pole piece. The combination of small clearances, strong magnetic forces, and brittle magnets necessitated the use of sophisticated assembly fixtures.

Alignment was maintained by tolerance control of machined parts and hand fitting at assembly. Spacers were provided to maintain the 0.015 inch axial gap between rotor and stator of the magnetic bearing and for axial centering of the touchdown bearing assembly. Measurements were made during

the assembly process and the spacers were ground to achieve the specified clearances.

A dynamic analysis of the energy wheel system was performed to determine resonant frequencies of the rotating system. A distributed mass was modeled for the shaft and discrete loads for the flywheel rotor and magnetic bearing rotors.

The first mode frequency of the rotating element was calculated to be 154 Hz. The first mode frequency of the rotating element coupled with the magnetic bearings was calculated to be 38 Hz. Both values were confirmed by test.

Rare earth magnets exhibit excellent magnetic properties which enable an engineer to build smaller reliable magnetic parts. The common permanent magnetic materials, alnicos and ferrites, are insufficient for our application because of size and weight constraints, and reliability. Samarium Cobalt, $SmCO_5$, magnets are small with high stability and provide high energy which makes them adaptable to be used in the magnetic bearing in the energy storage flywheel.

All magnets irrespective of the manufacturing techniques have fairly well specified remanence and induction coercive force; however, the intrinsic coercive force and the energy product values vary over a wide range as a result of sintering, heat treatment and the particle size. Magnetic pieces from a single lot cannot be accepted because several test samples happen to meet specifications. From Table 1 it can be seen that after measuring the residual inductance, B_r, and exposing it to a 10% demagnetization knock down field, H_k, 48% failed to meet the specification requirements. The finished, B_r, should be within ± 5% of the lot value after the demagnetization. Absolute B_r could not be readily measured on the finished product because the shape of the part did not match the induction coil utilized in the measuring procedure. To get around this, a standard B_r relative to the experimental setup was used and the B_r after knockdown was compared to the B_r before for each piece.

Properties of the magnet such as the B_r, coercive force, H_c, and the intrinsic coercive force, H_{ic}, are merely endpoints in the intrinsic or the

inductive demagnetization curve and do not give sufficient information about the loop shape. Therefore we specified that a plot of the second quadrant of the magnetization curve be supplied. The magnets were serialized, permitting us to select matched sets for each bearing.

The data required on the Samarium Cobalt magnets that we considered to be most useful were as follows:

B_r = 8,000 to 8,400 gauss

H_c = 7,700 to 8,100 oersteds

H_{ci} > 18K oersteds

BH > 16×10^6 gauss - oersteds

and full second quadrant B-H curve.

The high silicon, Si, low chromium, Cr, steel used in the stator was supposed to give a high permeability, μ, and resistivity, ρ. Permeability expresses the dynamic relationship between B and H and is a function B, H, ρ frequency of excitation, etc. Measurement of μ and ρ was made at Lincoln Laboratory and they fell short of our expectation. However, wet chemical analysis of the steel gave 1.7% Si instead of about 3% but an emission spectro-analysis confirms that Cr was low (< 0.5%).

B. Calculations

The target design of the brassboard system was to support a 25-lb rotor with spin axis within 30° of vertical in 1G, and allow an 750 ft. lb. sec. wheel to be rotated at approximately 0.5°/sec. cross axis rate. This was derived from system studies and satellite maneuvering or tipoff requirements. The resulting design impact was that bearing area must be sufficient to supply 15 lbs. of lift (20% safety margin) and the bearing separation adequate for the cross-axis torque.

The MTI report "A Theoretical and Experimental Investigation of the Magnetic Fields and Forces Arising in Magnetic Suspension Systems" by J. Walowit et al., 1975, was used as a basis for the design.

The important results of this study were the following:

1) Optimum tooth width T is roughly equal to the gap spacing h

2) Optimum tooth separation is between 3 and 4 times the gap spacing h

3) Use the B field in the middle of a tooth B as the scaling B field, the force density $F_n = 1/2\ B_o^2/M_o$ as the scaling force, density, the scaling magnetic flux $\Lambda_o = B_o A_t$ where A_t is the tooth area, and the MMF $\emptyset_o = B_o h/M_o$ where h is the gap spacing, and the scaling permeance is $\Lambda_o/\emptyset_o = P_o$

4) With the above scaling values and optimum dimensions, for square teeth $P/P_o = 1.4$, $F^*/F_o = 1.2$, $F^*/P^{*2} = 0.6\ F_o/P_o^2$ where F* is the force normal to the tooth, and $F_t/F_o = 0.08\ e/T$ where e is the transverse displacement and F_t the transverse force density per unit total bearing area. Also, F_t begins to flatten out for $e/T > 0.5$.

Therefore, I chose to allow a reasonable touchdown bearing clearance of ± (10 mils), h = 15 mils, T = 15 mils, S = 50 mils. I let the tooth depth be equal to the spacing. This allowed a working bearing range of ± 7.5 mils without saturating F_t. Probable value of the bearing force density would at e/T = .5 then be $0.04\ F_o/2$, the last factor of two due to the cylindrical geometry. The above choices were verified by comparison with available designs in the literature. Measured F_t appears to be 10 to 20% higher.

The axial forces can be calculated for a single model of our bearing without teeth for maximum magnet flux Λ, current NI in the coils, pole area A, effective total gap G_o ($G_o/2$ per pole), and displacement x the axial force should be

$$F_x = \frac{2\ \Lambda\ NI}{G_o} + \frac{2\ \Lambda^2\ x}{\mu o A\ G_o}$$

Therefore, for $x = G_o/4$ the total force is just equal to four times that calculated for one unbalanced pole of $\mu o^2/8$ A, and the force per rotor equal to the unbalanced equilibrium force on one rotor.

So, to estimate axial stiffness, at B_o = .83 T the average flux will be $1.7B_o$ times the tooth area or .33 T per unit pole area. This gives an unbalanced pole force density of $(.33/.83)^2 F_o = .156F_o$ in equilibrium. Therefore, at 7.5 mils displacement we will have $F_A = .156F_o$ and $R_R = .02F_o$ for a stiffness ratio of 7.8, which is in good agreement with the literature values of 6 to 8.

For most kinds of iron, tooth saturation occurs at B = 2.0 T and one must allow perhaps a factor of two due to field concentrations near corners. The desired field F_o was set to be .0833 T. This gave $F_o = 2.76 \times 10^5$ n/m^2 and $F_t = 5.5 \times 10^3$ n/m^2 per area of pole in the transverse directions.

The total 30 lbf = 133 N is supported effectively at 1/2 G at two ends, giving 33.25 N per bearing, 16.6 per rotor, or 8.3 per pole. Therefore, the pole area must be 15.1 cm^2, or a tooth area 3/13 of this = 3.48 cm^2 of tooth area, including the 20% safety factor of force required.

Based on a shaft diameter of .75 inch, an inner radius for the bearing-pole pieces of 1 cm was required. Then, by adding up tooth areas with 15 mil thickness and 50 mil spaces between, the radius of the inner teeth could be terminated at 9 teeth with 2.285 cm radius and 3.485 cm^2 accumulated area. Leaving just over 1 cm for coils, the inner ring of the outer poles had a radius of 3.30 cm. Adding rings and spaces as before give four teeth with 3.83 cm radius = 1.5 inches, with another 3.38 cm^2 accumulated area (close enough).

Now to determine the required spacing between bearings. At 15 lbs with motion of 7.5 mils, the radial stiffness is K_r = 2000 lbf/in. and for our stiffness ratio, the axial stiffness is K_A = 16,150 lbf/in. If all rings were located at a single radius D and separation L from the center of mass, the torsional stiffness would be

$$K_T = K_R L^2 \ (1 - K_A D^2 / K_R L^2)$$

Suppose (worst case) D = 1.5" and L = 6.0". Then, $K_t = .252\ K_R L^2 = 3.64 \times 10^4$ in-lb/rad or 3028 ft-lb/rad.

With angular deviation of 7.5 mils/6 in. = .00125 rad. This allows 3.8 ft-lb. or a cross-axis rate of 5×10^{-3} rad/sec = .28 deg/sec. However, things are not this bad since most rings are located closer to the spin axis, the average radius (center of the coils) being at 1.1 in. so that a better estimate of torsional stiffness is $K_T = .37\ K_R L^2$ and the resulting cross-axis rate capability is .413 deg/sec. This is close enough to specified values for a first cut design, since the relative stiffnesses are only approximately known. If the stiffness ratio is actually at the low end (6.0) this gives the required cross-axis torque.

To achieve the field of B_o = .833 T in the center of a tooth, assuming average B/B_o is perhaps 0.8, the required Λ/Λ_o = 1.75 so the average B in the iron behind the teeth is 1.75 (3/13) B_o = 0.33 T. The iron can be used to concentrate flux at the permanent magnet to be 0.67 T, about 80% of the residual flux level of SaCo magnets.

The required flux from the magnet is double the 1.75 B_o times the tooth area of 3.48 cm^2, or 10.1 webers. At the flux level of .67 T this requires a magnet cross section of 15.1 cm^2, at an average radius of 3 cm. This then requires an axial length of 0.8 cm. Allowing 20% leakage flux gives a cross section requirement for a magnet ring at 1.2 inches radius with length of 0.4 inch.

The expected MMF requirement is 2(0.8) B_o h/m_o or 400 amps. At 70% of Br a SaCo magnet can be expected to give an MMF of about 20% of its coercive force, or 1600 oersteds of 1.27×10^5 amps/meter. This then requires a magnet thickness of 3.17 mm = 125 mils. To give a safety factor and allow for iron losses, but primarily to increase magnet thickness for physical integrity with a better form factor, this was increased to 150 mils.

To keep drag low, magnet sections are to be matched within 5% or better and taken from a single lot. Also, bearing tooth dimensions are to be tightly controlled to determine how low the drag can be pushed.

C. Loop Design

In the axial direction, the stiffness of the bearing will be about 8x the passive direction stiffness of 2×10^3 lbf/in., or 1.6×10^4 lbf/in. = 2.8×10^6 n/m. The rotor weighs about 25 lbm = 11.34 kg. Therefore, the axial resonant frequency is 497 rad/sec = 79 Hz.

The loop compensation was intended to create a crossover frequency 10x higher than this, with a midband gain of 30 and a phase margin of 45°. To do so, a zero was placed at 3x the axial resonant frequency and a pole at 30x that frequency. This should give the 45° desired phase lead at a crossover of 800 Hz. All other poles must be located well beyond 2.4 kHz, preferably beyond 8 kHz.

Therefore, a sensor with 10 kHz bandwidth has been chosen. Effects of structural resonances and phase lag due to eddy currents in the bearing materials must be measured and compensated for during system testing.

During integration, it was found that the many vibration modes of the system required lowering the crossover frequency to 150 Hz.

D. Magnetic Bearing Integration and Test

The assembly of magnetic bearing parts went relatively smoothly. Press-fitting of stator parts required good positive control of the planar positioning of parts; otherwise they tended to tip over and bind. One stator was successfully disassembled and rebuilt.

Stators were measured for magnetic field variation with rotation. A modification of the fixturing for stator assembly and a magnetoresistor were used. The results showed that the open-circuit stator field of 1000 gauss had variations on S/N 1 of ± 20 gauss. These variations should be halved again at least by the addition of rotors to close the circuit. Therefore, variations in B of 0.2% can be expected with rotation.

Mechanical tolerances on bearing tooth runout and height were measured to be typically ± 0.1 mil, with occasional peaks of ± 0.2 mils. These represent about 0.3% variations in the effective gap total of 30 mils.

Therefore, the sum of all B-field variations is expected to be within 0.5%. This will lead to drag due to eddy currents in the bearing material with power

density of $\frac{1}{2\rho}(\omega\Delta BL)^2$ where L is the length scaling the eddy currents. Over a volume = AL the resulting power loss is on the order of $P = \frac{1}{2\rho}\omega^2\Delta B^2L^3A$ watts. For measured $\rho = 10^{-5}$ Ω-cm = 10^{-7} Ω-m, $L = 3.8 \times 10^{-4}$ m, $A = 4 \times 10^{-3}m^2$, $\Delta\beta = 3.5 \times 10^{-3}T$, $w = 5 \times 10^{3}$, $P = 3 \times 10^{-4}$ watts. Ridiculous! But if $L = 3.8 \times 10^{-2}m$, then P = 300 watts, so the eddy current scaling length L is critical.

Assembly of the bearings onto the shaft went as planned. Forces near 250 pounds were encountered when positioning bearing pole pieces and stators onto the shaft, but the use of jacking screws and holding fixtures was successful. Use of aluminum or stainless in fixtures caused some galling problems, which were solved by a little lubricant. A better answer would be to use brass for tight fitting fixtures.

Applying swept frequency currents to the motors allowed measurement of resonances in the structure. Also, the current needed for moving the rotor from one end to the other was measured to be 2 amps on both motors, or 4 amps on one motor. This showed some increase (to near 6 amps on one end) as time progressed, perhaps due to extended touchdown gaps. The linearity was gratifying.

Resonances were found at several frequencies in the structure. One problem was the original position sensor and its mounting bracket. It had internal nodes in the micrometer adjustment as well as a cantilevered geometry. A new sensor with no micrometer and a bracket with no cantilever was designed and solved this problem.

The flywheel rotor turned out to have a very high Q resonance at about 2.1 kHz. This was clearly audible as a ringing if the rotor were struck. Use of fiberglass spacers between rotor and shaft did not help. Eventually, a notch filter with Q = 5 was built to eliminate the problem. This worked. A non-metallic rotor would eliminate the problem.

Several other resonances were not easy to locate but did not cause large phase shifts in the bearing loop. A transverse resonance due to shaft bending at 154 Hz was numerically predicted and verified. Longitudinal resonance at 400 Hz and at 600 Hz is believed to be bending of the yoke arms. A stiffening yoke member may be added later.

The bearing was floated initially with the new sensor and bracket but no notch filter.

It had no phase margin and a small (± 1 mil) residual oscillation at its crossover frequency of 150 Hz. Addition of the notch filter allowed lead compensation which gave over 30° of phase margin, a dc loop gain of 5, and crossover frequency of 150 Hz. The bearing is sensitive to resonances in its mounting structure. Mounting on a table which is not flat causes oscillations at about 400 Hz, believed to be due to the rocking of the assembly causing phase shifts and interacting with the yoke bending modes.

In use in a satellite, such a bearing would have to be designed into the structural dynamics, and the dynamics of the structure also designed into the bearing loop.

The bearing motor inductance was close to the 15 mH predicted value at low frequencies and as predicted fell off as almost $1/\sqrt{s}$ at frequencies above 100 Hz due to eddy currents. To avoid large circulating currents of 50 kHz due to current driven switching, a 2 mH pot core inductor was added in series.

The floated bearing showed stiffnesses of about 10 lbf/mil along the spin axis, about 1.2 lbf/mil transverse, and 3.26 foot-lbf per milliradian transverse rotational stiffness. This was in good agreement for axial to radial stiffness but low by about a factor of two in total stiffness. The cause is presently unknown. Increased stiffnesses can probably be obtained by reducing the magnetic gap.

One possible explanation of the low stiffness values could be larger than predicted reluctance in the bearing pole piece iron. This could result in increased flux leakage or in the flux clustering near the magnet and not giving much centering at the inner and outer fringe rings. Such an effect could be avoided by designing for larger magnetic gap and larger clearances (more magnet length), or by using better iron or lower field strengths (more bearing area). Due to the small dimensions of the gap, it is difficult to measure the radial field distribution.

Resonant frequencies were looked for to verify stiffness measurements and check damping. The transverse translation resonance at 22 Hz checks out, and has a damping time constant of about 2 seconds. The rotational damping is too

large to measure; it may be critically damped. A Bode plot of position vs. input current shows a very linear force/current relationship and a pair of poles at 80 Hz as expected.

Position sensor outputs, using Lion precision capacitance non-contact sensors, are used for position and velocity sense lines. These are very troublesome due to the capacitance sensitivity of all 1 MHz tuned cables and non-interchangeable probe types causing anomalously high gain (almost double) in the sensor outputs. These are supposed to be approximately 1 volt/mil and 1 volt/mil/millisecond, respectively. The small signal electronics transfer function, without the 2.1 kHz center Q:5 notch filter, is then

$$\frac{I(\text{amps})}{Z(\text{mils})} = \frac{(2 \text{ ms } S+1)}{(.039 \text{ ms } S+1)\ (.047 \text{ ms } S+1)}$$

$$\frac{(1 \text{ ms } S+1)\ (.33 \text{ ms } S+1)\ (.07 \text{ ms } S+1)\ (.02 \text{ ms } S+1)}{(.5 \text{ ms } S+1)\ (.14 \text{ ms } S+1)\ (.04 \text{ ms } S+1)\ (.22 \text{ ms } S+1)}$$

The alternating poles and zeros in the right side of this expression are an attempt to compensate for the $1/\sqrt{S}$ eddy current effect with a 45° lead network. The zero at 2 ms is created by adding the position and velocity outputs of the sensor together with appropriate gains. The poles at .039 ms, .047 ms, and .22 ms are low-pass filters to eliminate the effects of high-frequency resonances in the system.

An additional feedback loop using an integrator with clipped output is used to eliminate steady-state current by automatically seeking the null force point. This "VZP" circuit, first used in this application by S. Lyman of Cambion Corp., adds a multiplier to the transfer function

$$\frac{100 \text{ ms } S}{100 \text{ ms } S-1}$$

With this circuit in operation, or without it and with the offset position trimmed to zero, the power drawn by the fully redundant bearing system is just under 2.0 watts. This is independent of the rotor weight up to the touchdown point: over 150 pounds in the vertical position. This input power can probably

be reduced by a factor of two in future systems if it matters by improving the sensor electronics and reducing the number of op amps. Redundancy has been demonstrated by manually switching off one motor and turning on the other, one sensor per motor.

To enhance the liftoff (large signal) stability of the bearing, a nonlinear lead network is added. This is to attempt to compensate for the LdI/dt limitations of the power supply (± 15 volts). Through Zener diodes, the network introduces a 4.7 ms zero above 2.4 amps and increases this to a 22 ms zero above 5 amps, with an accompanying .044 ms pole.

The current drive circuit, presently a half bridge switched at 50 kHz, is quite efficient but should be replaced by a full bridge. This would allow larger LdI/dt, would simplify power conditioning by using unregulated bus, and would avoid one supply boosting the other through the current driver output inductance.

The motor characteristics of the bearing are 50 lbf/amp and 5 lbf/mil per motor giving a measured total open loop dc gain of 5 for one active motor and one passive one. If, as appears possible, the sensor gain is anomalously high X2, the motor gain may be lower by a factor of two.

Magnetic gaps have been measured in floated and non-floated conditions to be within 5% of nominal values: gaps on both sides of the stator sum to 30 mils. Total rotor motion between touchdown stops is 22.5 mils. Drag is dominated by air flows and spin-down time constant is measured to be one to two hours in air at ambient pressure. Ball bearing drag by comparison gives spin-down time constants of less than one minute under 150 lb. estimated preload on the touchdown bearings.

The actual hardware under test is shown in Fig. 4-2. Construction details are shown for the stator in Fig. 4-3, 4-4, and 4-5, the test flywheel and shaft in Fig. 4-6, the touchdown bearings in 4-7, bearing housing and shims in 4-8, assembly fixtures in 4-9 and the electronics control panel in 4-10.

Several very interesting observations were made while measuring bearing drag. First, the drag is dominated by aerodynamic forces down to quite low pressures, on the order of 10 microns. This implies that a spacecraft device

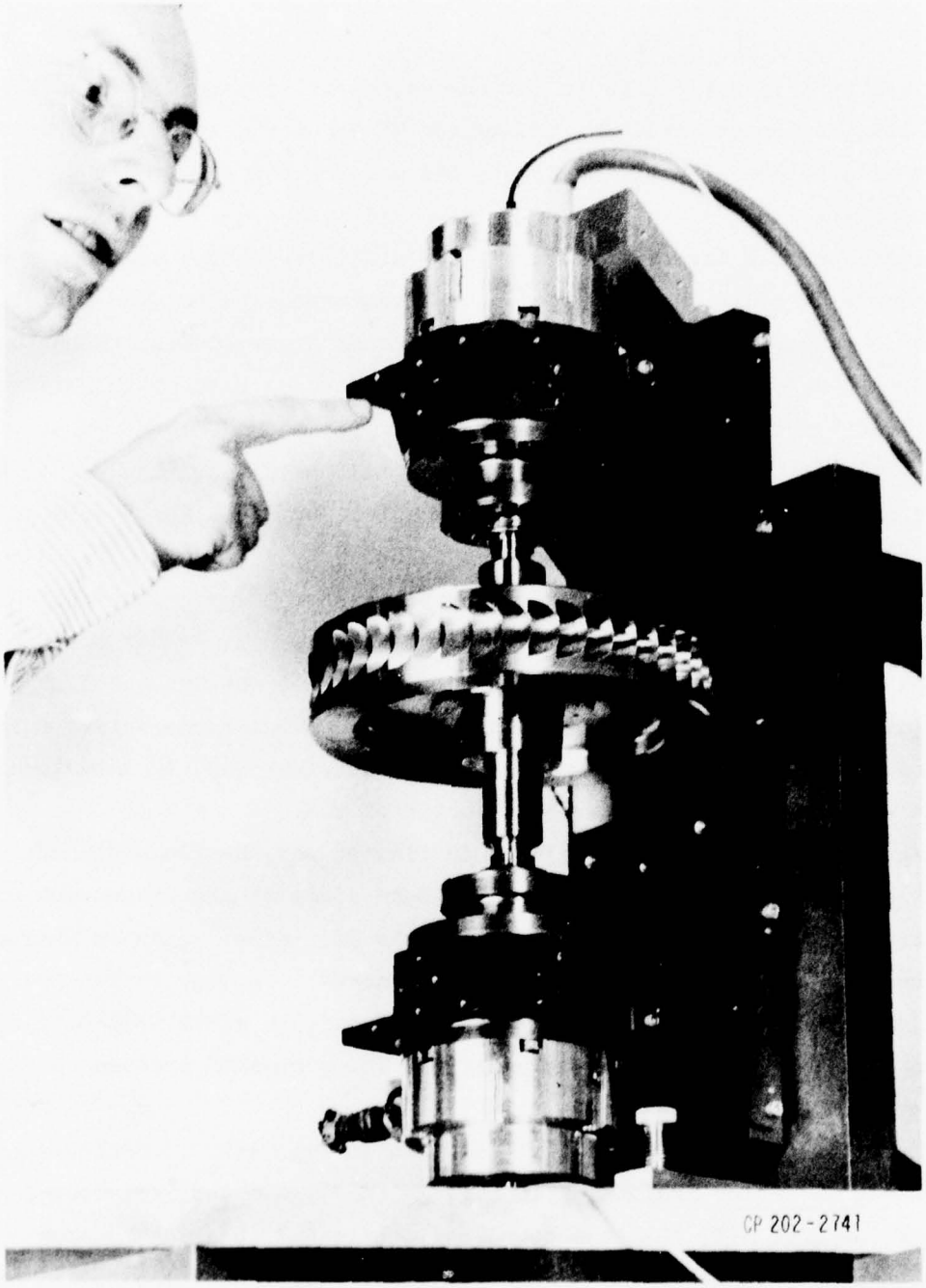


Fig. 4-2. Magnetic bearing system test.

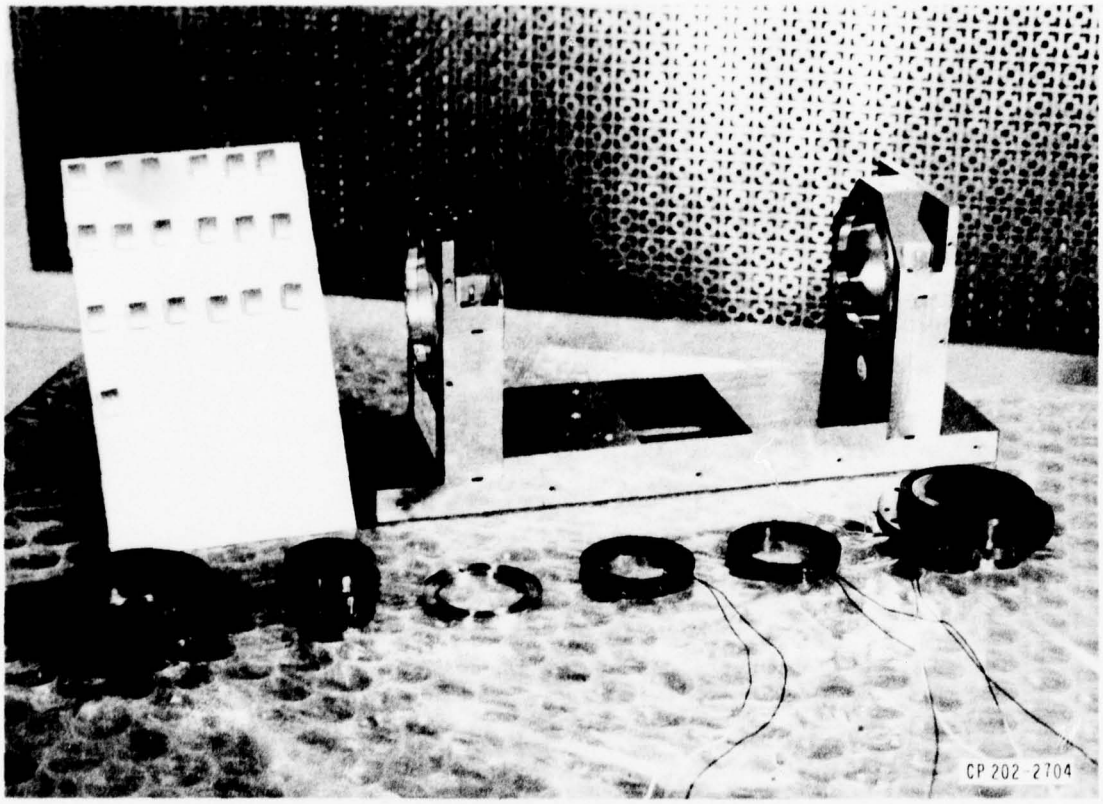


Fig. 4-3. Bearing stator assembly and test bed.



Fig. 4-4. Construction of bearing stator.

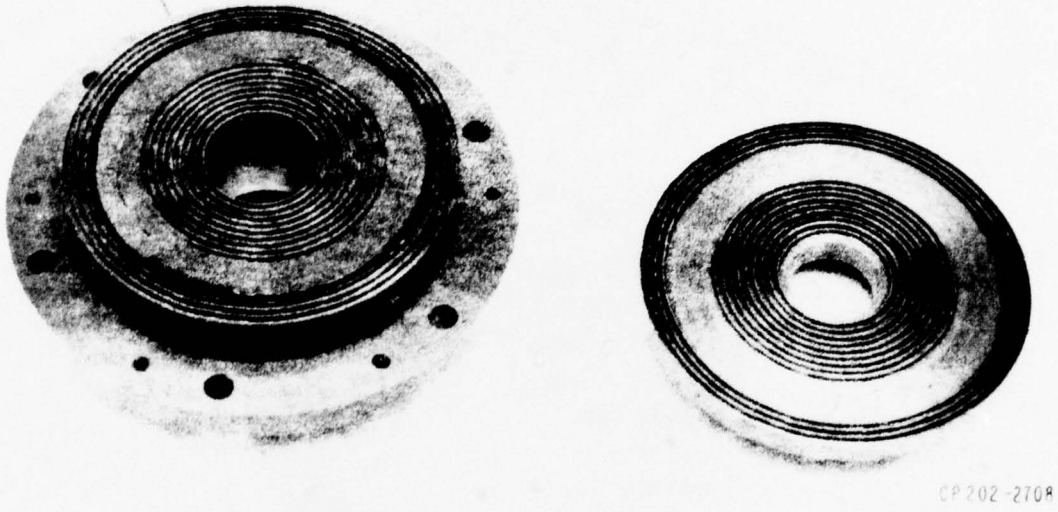


Fig. 4-5. Bearing stator and rotor.

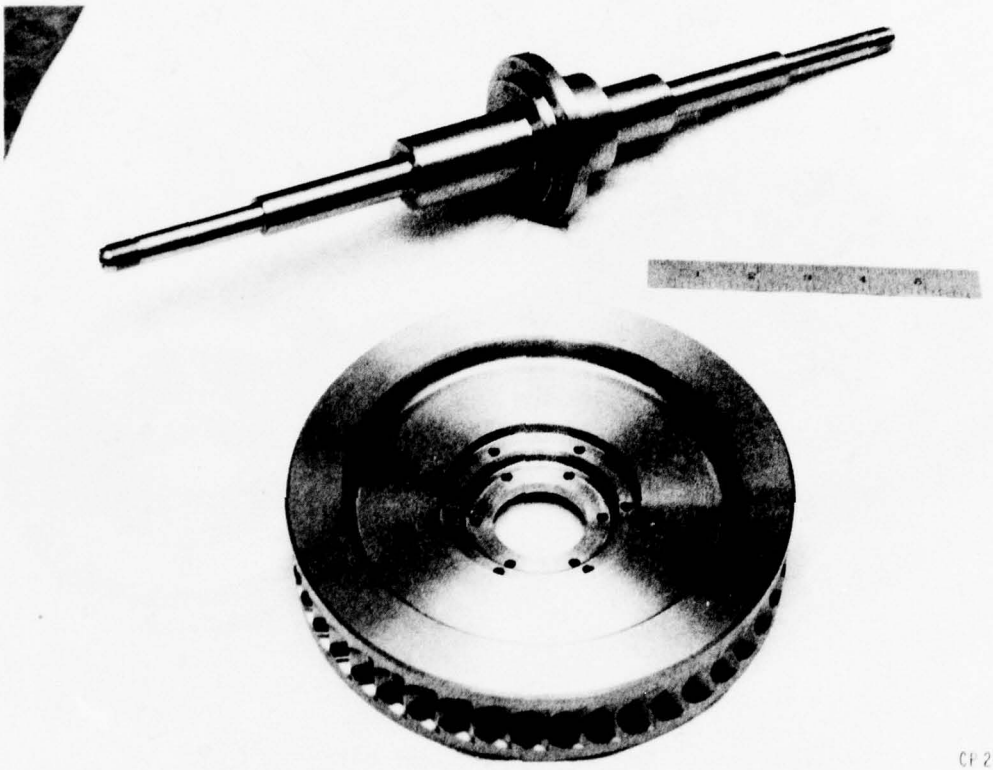


Fig. 4-6. Flywheel and shaft.

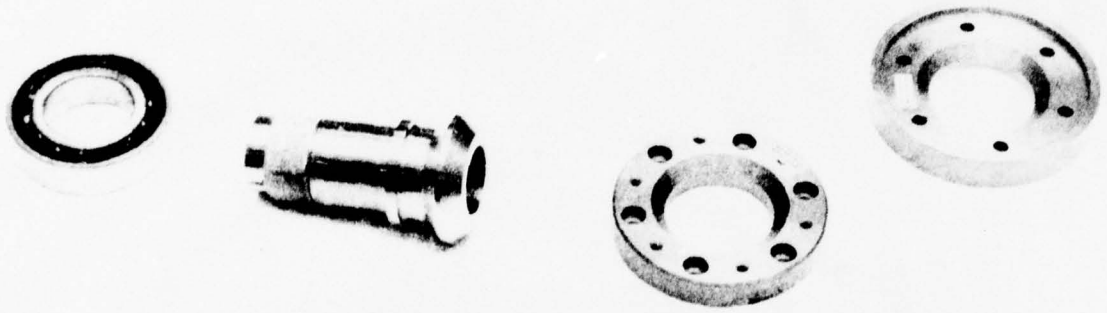


Fig. 4-7. Touchdown bearings.



Fig. 4-8. Touchdown bearing housing.

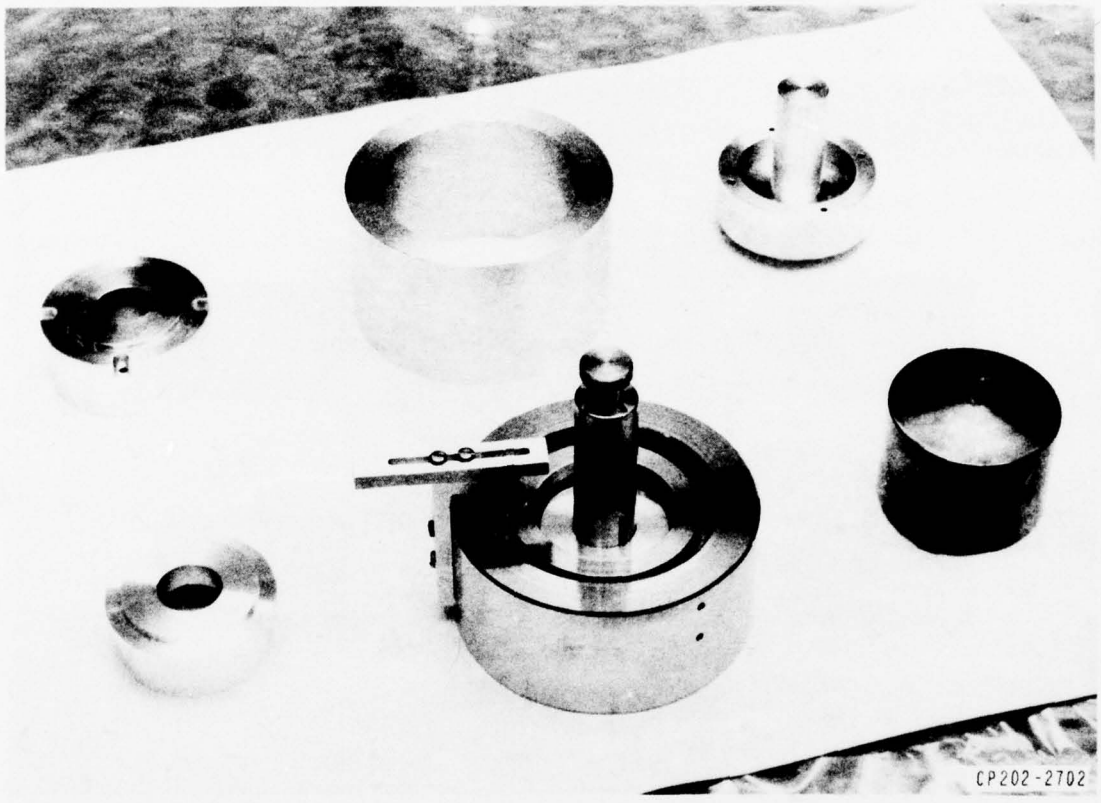


Fig. 4-9. Assembly fixtures.

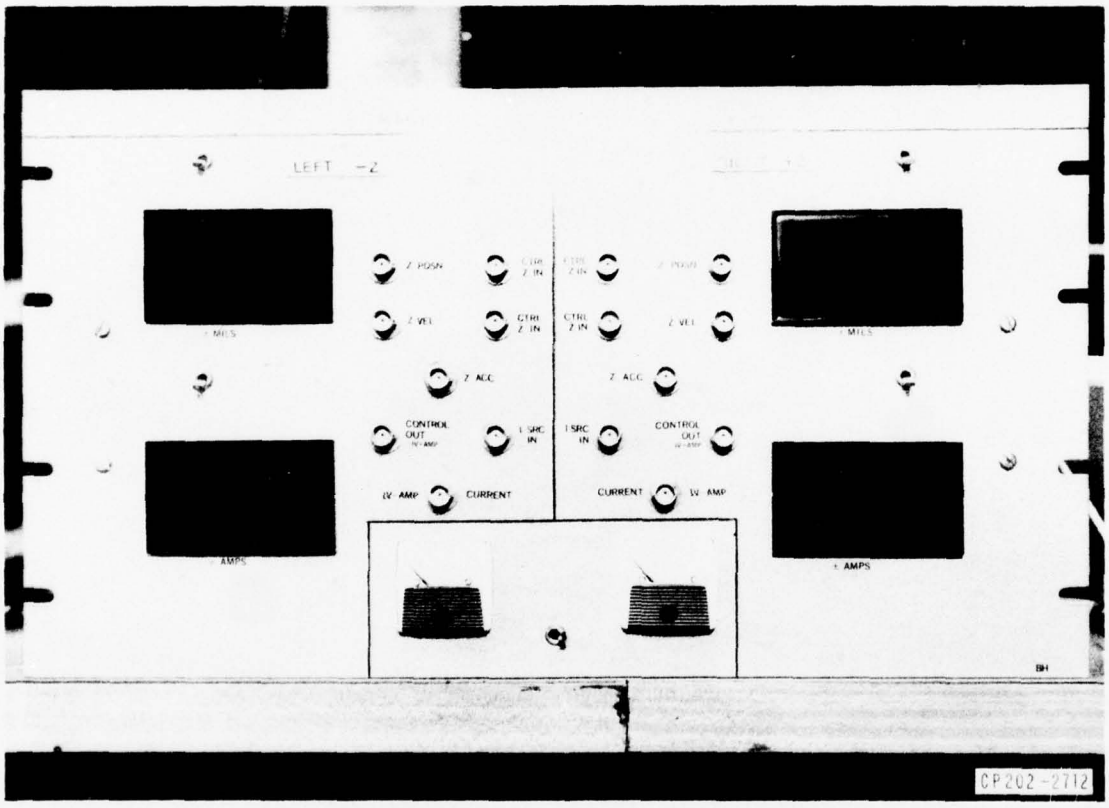


Fig. 4-10. Bearing control panel.

must be well vented to take full advantage of its environment, and ground testing should be done with a cryopump. Second, the drag has its lowest value below the lowest critical speed, reaches a sharp maximum at that speed, and settles down to a higher drag at supercritical speeds. For our test system, rotating M = 25 lbs. and I = 0.586 in.lbf-sec^2. Besides the resonance, the drag torque appeared to be linearily proportional to speed over a range of 50 RPM to 1.5 KRPM, with critical speed at about 1.2KRPM. Below critical, if T = Bw and spindown time constant τ = I/B = 30 hours and so B = 5.4×10^{-6} in-lbf-sec = 8.7×10^{-5} in-oz-sec. or a drag of 9.1×10^{-3} in-oz. per 1KRPM.

Above critical speed, drag was approximately 22 hours, or B = 1.2×10^{-4} in-oz-sec. for a drag of .012 in-oz. per 1KRPM. This was measured with a rotor which had not been balanced at all. Therefore it should not be any surprise that the drag is higher, due to the rotation of the shaft geometric center about the principal axis of the rotor. In fact, this indicates that poorly balanced nonmetallic rotors will not have a problem due to drag.

Drag versus speed and pressure are plotted on Figs. 4-11 and 4-12. The 30-hour drag rate corresponds to power inputs of .67 watt at 10,000 RPM or 19 watts at 50,000 RPM.

E. Finite Element and Field Plotting Capabilities

To allow exploration of magnetic bearing tooth geometries and to verify design calculations, a magnetic field finite element analysis program has been developed. This was used to verify reluctance calculations for the LES magnetic bearing. Further work using this program is expected to give more insight into construction of many types of electromagnetic devices.

MIT/LL Electromagnetic Field Computer Analysis

Lincoln Laboratory has added electromagnetic field calculation features to the well-known general-purpose structural analysis system ICES-STRUDL. When operated on the Laboratory's IBM 370/168 computer, the ICES executive provides the data management and program management facilities needed to minimize storage and computation requirements, while the STRUDL subsystem provides the finite element and equation solving facilities needed for efficient analysis.

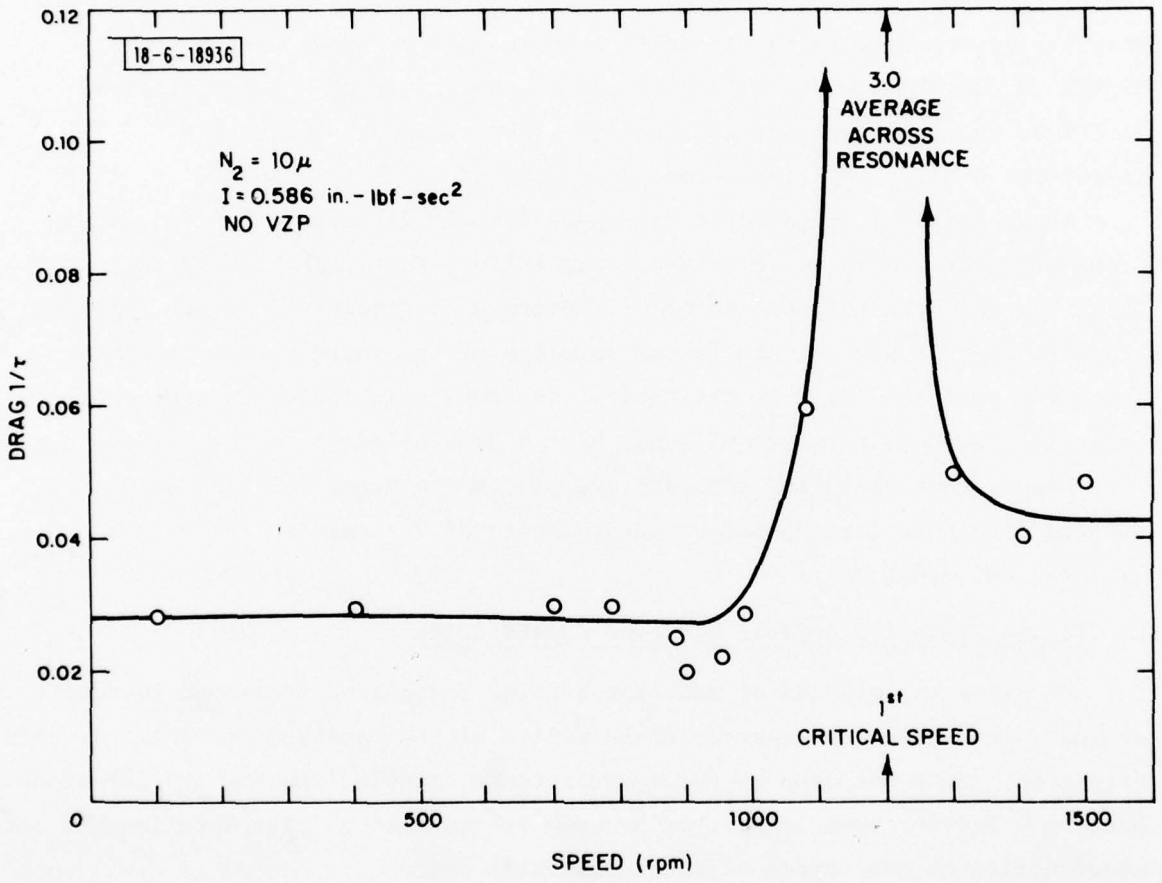


Fig. 4-11. Drag vs. speed.

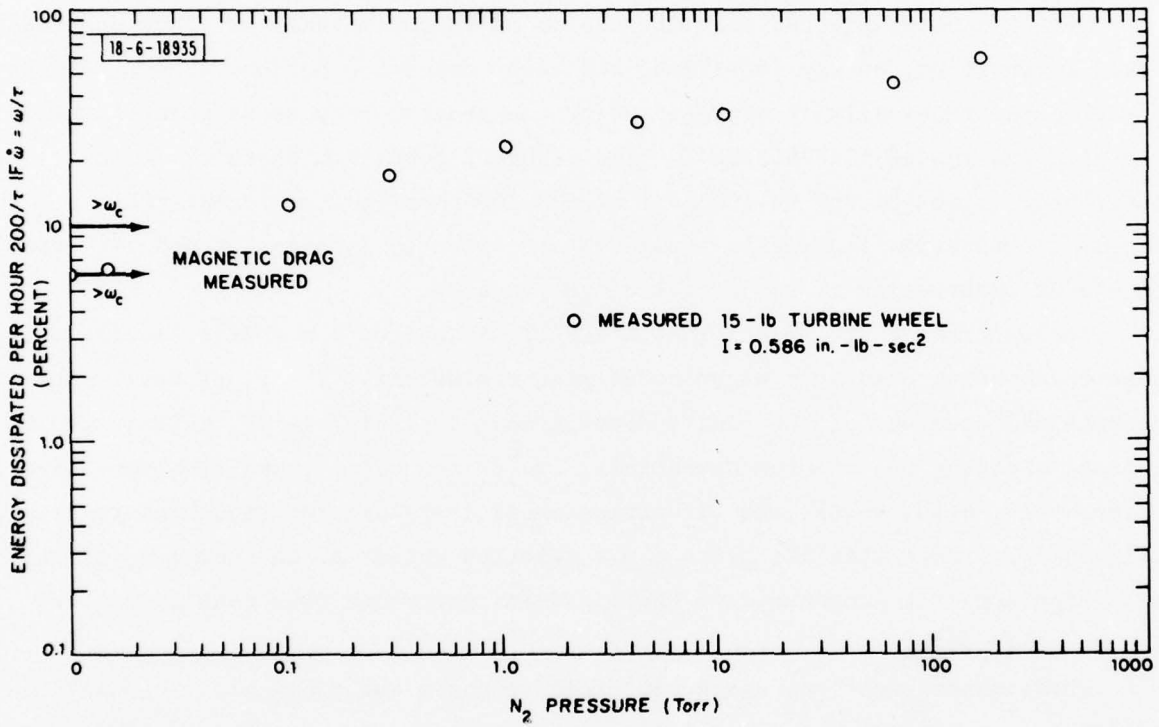


Fig. 4-12. Drag vs. pressure.

Families of isoparametric finite elements are available for scalar potential models (electric or magnetic) and for magnetic vector potential models. These families presently consist of 6 different types: linear, quadratic, and cubic planar quadrilaterial elements; linear and quadratic 3-dimensional brick elements; and a linear 3-dimensional triangular prism element. Nonlinear material properties for permeability and permittivity will soon be available.

Output quantities available are scalar or vector potentials, flux densities, field intensities, energy densities, and electromagnetic forces. These results may then be graphically interpreted using the general-purpose structural analysis plotting system ICES-STRUPLOT. The STRUPLOT subsystem operates in the interactive time-sharing environment of CMS-ICES, using free-format CDL (command definition language). Commands are selected dynamically and are based on visual observation of successive plots produced.

Enclosed are four typical ICES-STRUPLOT plots from a magnetic bearing tooth case study using quadratic eight-noded planar elements. The plots verify the geometrical accuracy of the finite element modeling (Fig. 4-13); illustrate the contour plotting feature for potentials, field intensities, and flux densities (Figs. 4-14, 4-15, 4-16); and illustrate nodal averaging for smoothing results (Fig. 4-16). Note that the plots are a selected subset of the total model and also that specific components of the field intensity and flux density vectors can be selected.

These described electromagnetic finite element and field plotting capabilities are an extension of well-known and popular general-purpose structural analysis systems, and future maintenance and/or further enhancement of them will require very little extra effort.

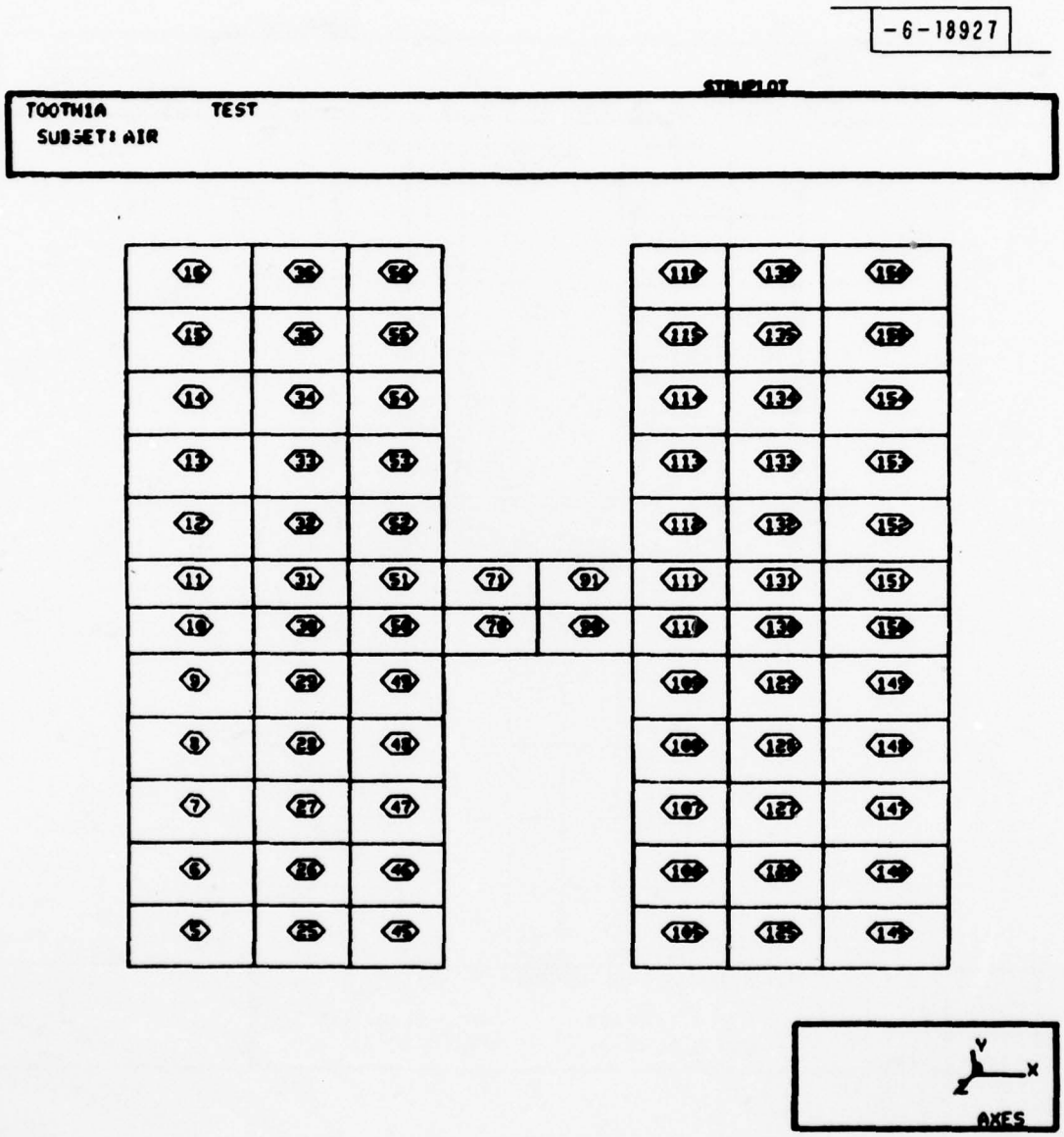


Fig. 4-13. Finite elements.

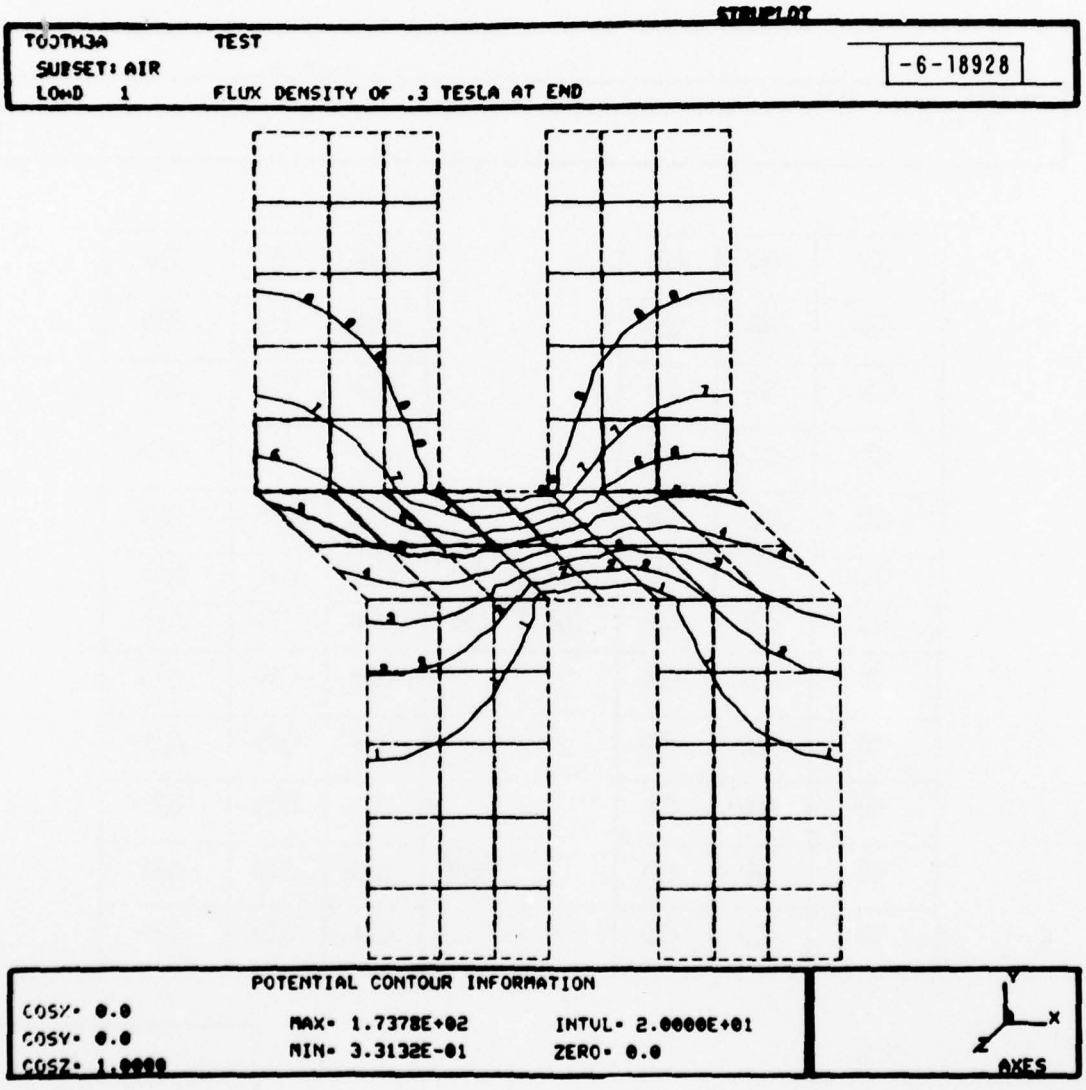


Fig. 4-14. Potential contours.

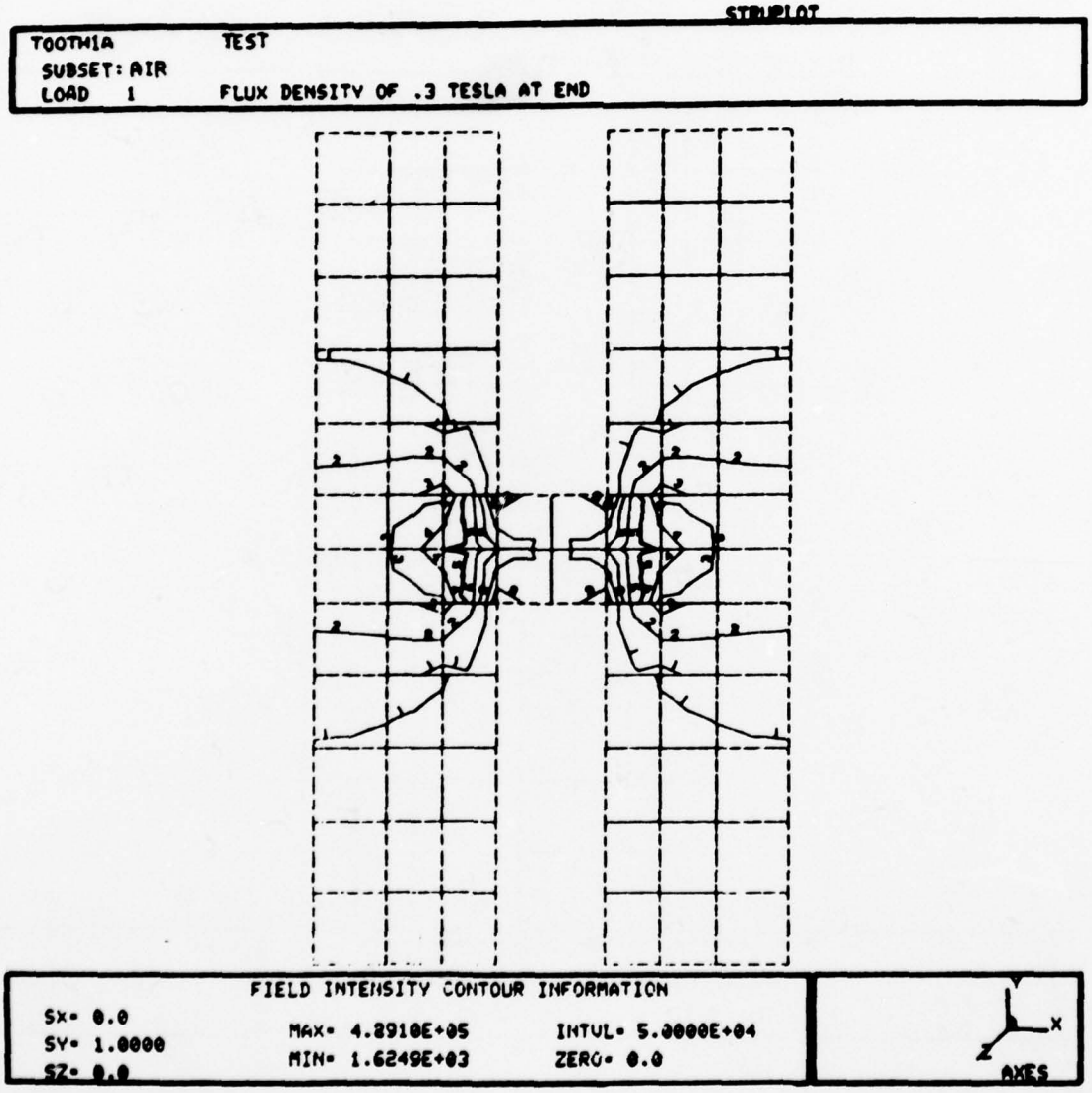


Fig. 4-15. Field intensity contours.

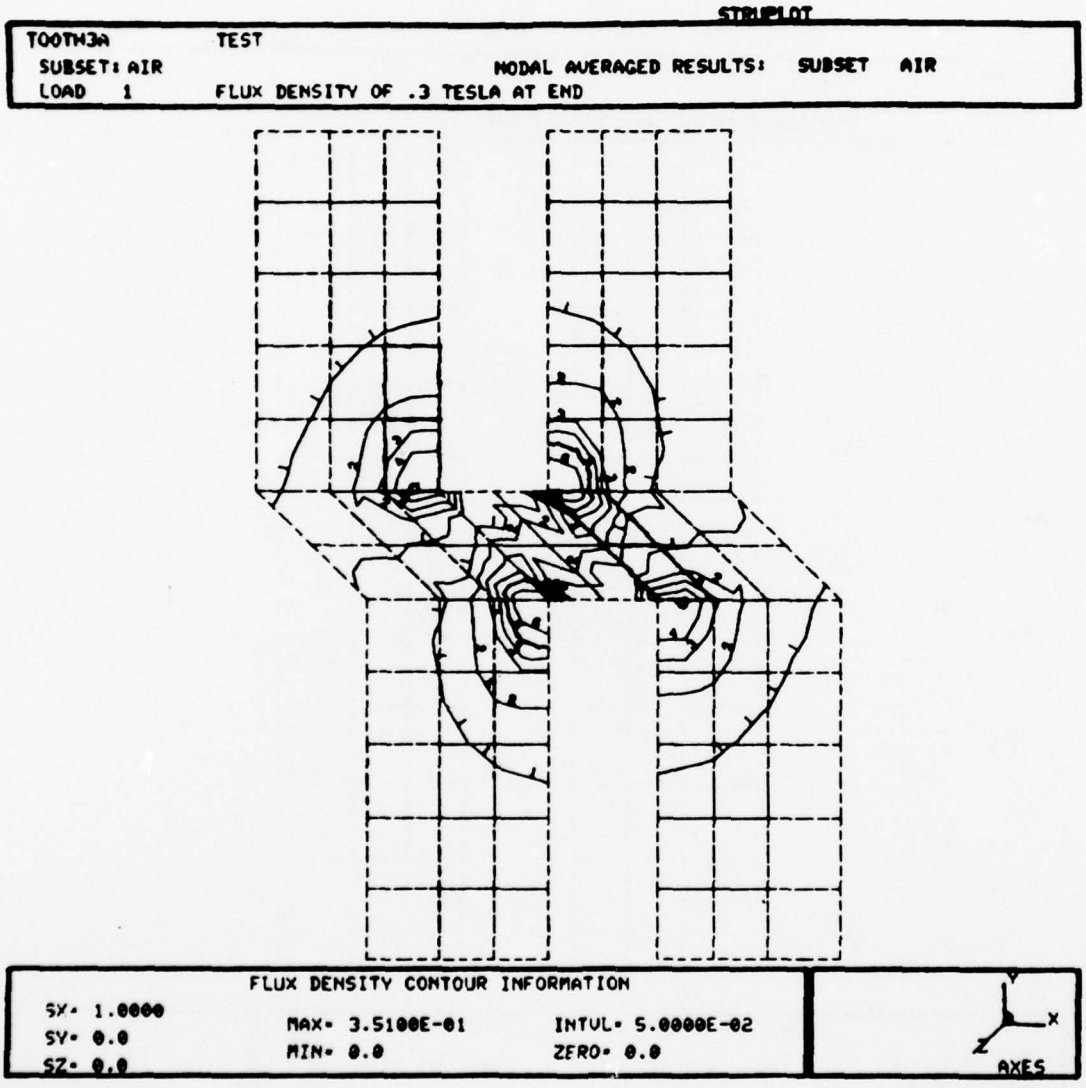


Fig. 4-16. Flux density contours.

V. MOTOR GENERATOR

A. Design Goals and Tradeoffs

An efficient flywheel system needs a motor generator with very low coasting losses and efficient generating and motoring modes, in that order of importance. High speeds allow a smaller unit and smaller electronics with higher quality output, but make the efficiency problem worse. By using unconventional design approaches, the LL motor generator program attempted to resolve this difficulty. The attempt appears to be successful based on available diagnostics. High speeds require no slip rings or moving contacts. It is difficult but not impossible to keep field variations small with a homopolar or Lundell type induction machine, so that a permanent magnet rotor looked attractive. Active solid state commutation would allow output regulation, so the lack of control of field strength would not be a problem. Also, the lack of field exitation would avoid associated losses. However, the field could not be turned off during coasting to avoid drag.

The availability of Samarium Cobalt permanent magnets prompted to choice of a permanent magnet rotor. They offer a smaller, lighter rotor than would otherwise be possible, and allow large magnetic gaps to minimize armature losses.

To avoid high drag from the rotating field, an ironless stator was chosen. This is compatible with the high coercive force of the rotor magnets. To avoid eddy current losses in the stator, the conductors were made of Litz wire (very small, individually insulated filaments) and no other conducting material was used in the rotor. All iron in the magnetic path rotates with the magnets.

The choice of numbers of poles could be made two ways. If the stator currents are to be sinusoidal, produced by a chopped DC waveform, then the number of poles must be minimized to keep the chopping frequency low. At 50 KRPM, a two-pole machine with ten chopping cycles per rotation requires over 8 kHz chopping rate. A two-pole machine would require long wire runs between poles.

However, using the concept of square-wave drive, the chopping frequency equals the electromagnetic angular rate, so that ten times the number of poles

can be accommodated at the same switching speed. It is also desirable to use a 3 phase drive to eliminate third harmonic effects in the square-wave drive. A 12-pole design allows this, with electrical chopping frequency of 4x rotational rate, which at 50 KRPM gives about 3.3 kHz. Allowing 10% for rather thin pulses for low-power motoring, this gives pulse widths of 15 μsec, comfortably longer than the 1 μsec switching times typical of appropriately sized transistors.

A scheme for laying two rows of conductors with all three phases and no empty space was worked out, allowing minimum gap in the motor and so minimum magnet size. Stresses in the magnets appeared critical and a system of support using titanium for support and an iron pole piece was designed. An iron return path rotor was used.

The resulting structure was therefore a SaCo and steel and titanium rotor, an iron return path, and an ironless stator with two layers of Litz wire. Twelve poles and three phases were selected.

Various electrical voltage level schemes and switching circuits were considered. The driving consideration was that generating efficiency be high, so the open circuit voltage was chosen to be higher than the required 28 VDC bus over the generating range. An upconverter to a variable DC bus is used for motoring, and a 3-phase bridge of diodes and transistors (6 each) used to interface the M/G leads to a varying DC bus. The variable DC is then downconverted (efficiently) to the 28 VDC satellite bus.

At this point in the design, it was decided to contract out the final design and characterization of the motor-generator to an experienced manufacturer. A design specification for the motor-generator and interface drawing were drafted and released. Goals of 5 lbs and 85% generating efficiency were set for a fully redundant 250 watt unit.

B. Design Realization

The contract was awarded to Sperry Electro Components after competitive bidding. Sperry reviewed the design tradeoffs in the areas of chopping frequency, conversion circuitry, and hardware implementation. Their findings

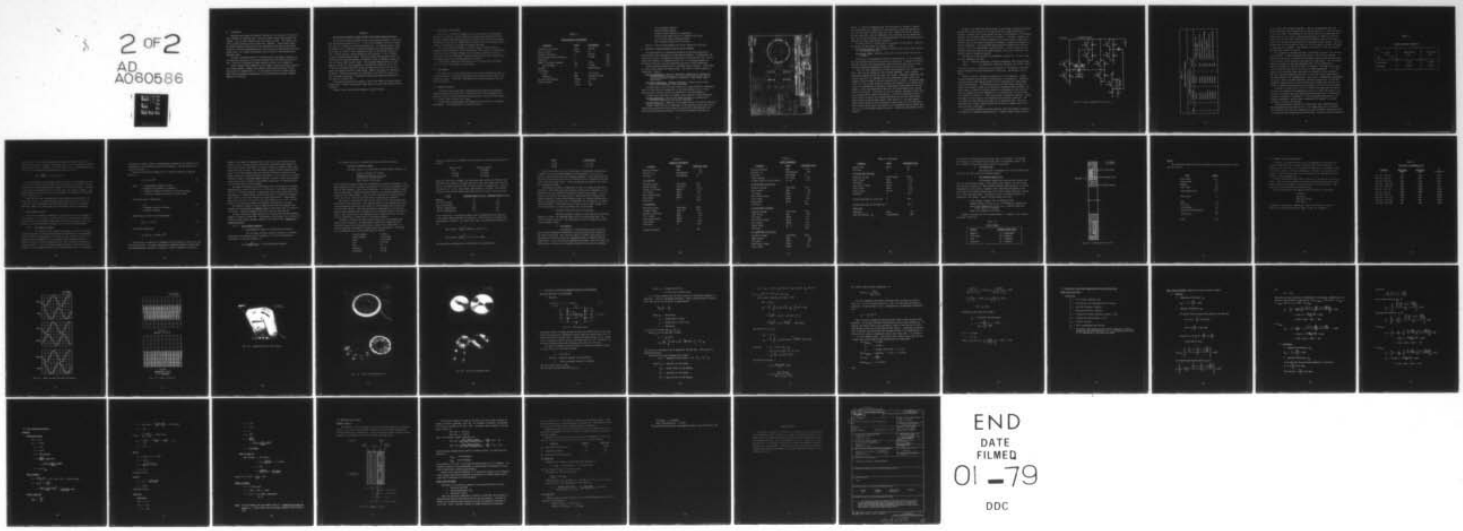
agreed with our own that a three-phase, square-wave drive should be used, that 12 poles was near optimum, that the bridge and motoring upconverter and generating downconverter g ve best system efficiency, and that weight and efficiency goals were close to achievable values. The titanium magnet support structure was modified but conceptually adopted. The use of Litz wire was adopted too, but more to improve field penetration into the windings than to decrease drag. The coils were wrapped on three separate layers for ease of manufacture, with fiberglass stiffness between coils. The connection scheme was modified from delta to wye to allow for nonuniformity of fields without excessive losses. Appendix A is the Sperry report.

Sperry built a brassboard of the motor generator. It is like a final model except for the use of readily available steel instead of high-strength materials, as it is unable to run at full 50 KRPM. This brassboard can be mounted to the LES magnetic bearing test bed for further experiments.

Results of the design show that even higher efficiencies than expected can be achieved with this unit, with average constant-power generating efficiency of the generator of 96% and electronics 92.5%, giving system overall generating efficiency of 88.5% estimated. Motoring is also good, with machine 94.5% and electronics 89.5% for overall motoring efficiency 84%. This gives total input-output efficiency of 74.3%, a very respectable number.

AD-A060 586 MASSACHUSETTS INST OF TECH LEXINGTON LINCOLN LAB F/G 10/3
FLYWHEEL COMPONENTS FOR SATELLITE APPLICATIONS.(U)
MAY 78 A R MILLNER F19628-78-C-0002
UNCLASSIFIED TN-1978-4 ESD-TR-78-97 NL

2 OF 2
AD
A060586



END
DATE
FILMED
01 -79
DDC

VI. CONCLUSIONS

Momentum wheels made with magnetic bearings are far superior to those with ball bearings for spacecraft use. They allow higher speeds and therefore are lighter. They are more reliable over long periods of time. They require very little operating power and can be made fully redundant. Their design should be radially-passive, axially-active for applications requiring low cross-axis rates due to satellite maneuvering, and 5-axis active for applications requiring higher (over 1 or 2 degree per second) cross axis rates or an electronically gimballed wheel.

The most troublesome aspect of a momentum wheel with magnetic bearings is the potential interaction of the active bearing loops with the satellite structure. This can be resolved by design analysis but must not be neglected.

Energy storage using flywheels is only slightly lighter than NiH_2 batteries and is more complex. However, such energy storage looks attractive if attitude control is combined with it. It also looks attractive if power requirements dictate extensive conditioning of the battery output voltage, through a regulator or inverter.

APPENDIX A

Lincoln Motor-Generator Design (Contract with Sperry Rand Corporation)

The Lincoln Laboratory flywheel system motor-generator design is compatible with system design layout Fig. 4-1. It is a fully redundant 250 watt DC brushless unit for operation on a 28 VDC satellite bus. Its samarium-cobalt permanent magnet rotor is capable of 50,000 RPM operation with full generation capability down to 20 KRPM. Extra windings are used for induced EMF commutation with a special start-up circuit needed for cold starting. It is a 3-phase, 12 pole, ironless armature design. The three phases are separately wound on individual non-conducting armature stiffeners for ease of assembly, using Litz wire to minimize eddy current losses. The permanent magnets and iron in the magnetic circuit all rotate together to eliminate eddy currents in the iron. A titanium containment structure houses the magnets and iron on the rotor to support the magnet material at high speeds. Magnets are purely in compression by design. Estimated efficiency as a generator is over 90%, as a motor over 85%, including electronics. Performance analysis and brassboard hardware were delivered on 1 October 1977.

This design should scale up easily to the 6-10 kW level for larger system applications. Higher scaling levels might impact the power switching electronic interface.

Sperry's report on the Motor Generator contract follows.

A.1 INTRODUCTION AND PURPOSES

This report is written to summarize the work performed on Massachusetts Institute of Technology Lincoln Laboratory Purchase Order F19628-76-C-002 PO CX-1340, Flywheel Motor-Generator Design as covered by MIT Specification dated 8 February 1977 and RFI No. 30098 dated 21 December 1976 and subsequent modifications as discussed in the design coordination meetings.

This order covered the design of an Axial Airgap, Ironless Armature, Brushless DC Motor-Generator and the development techniques for its fabrication. The design effort involved trading-off motor generator performance with the driver type and then optimizing the generating performance with secondary goals of minimum weight, size, and high motoring efficiency.

An Engineering sample was fabricated to verify manufacturing techniques and as a check on the magnetic circuit design.

A.2 REQUIREMENTS

The primary goal of this design effort was to obtain maximum efficiency in the generator mode. Additional requirements and design goals were used to constrain the design. The salient requirements for the Motor-Generator are presented in Table A-1.

A.3 SUMMARY OF RESULTS

A tradeoff analysis was made of several possible commutation/regulation systems resulting in selection of a three-phase, discretely commutated motor generator using an external regulator and operating at relatively high voltage, i.e., always higher than the bus voltage.

A twelve-pole motor/generator was designed which exceeded all performance requirements. This design has the following features:

TABLE A-1

MOTOR-GENERATOR REQUIREMENTS

PARAMETERS	UNITS	REQUIREMENTS	GOAL
Generator Output Power	Watts	250 Min.	
Output Voltage	Volts	28	
Generator Efficiency	%	92% Min.	Max.
Total Generator Mode Efficiency	%	70% Min.	Max.
Redundancy	-		Full
Weight - One Motor Generator	Lbs.	5 Max.	Min.
Full Redundant	Lbs.	6.5 Max.	Min.
Rotation	-	Bidirectional	
Speed Range			
Motor	RPM	0 to 50,000	
Generator	RPM	20,000 to 50,000	
Air Gaps and Clearance	Inches	.015 Min.	
Design Lifetime	Years	10	
	Cycles	3000	

- Fully Redundant Windings.
- Samarium Cobalt Magnets.
- Integral Pickoff Winding for Commutation.
- Primary Losses Resulting in 96% Generator Efficiency.
- Litz wire for Coils to Minimize Losses.
- High Strength Titanium Rotor Structure.

Figure A-1 shows the performance and outline drawing for this unit.

A.4 SELECTION OF MOTOR/GENERATOR TYPE AND DRIVE INTERFACE

The design approach is determined primarily by the system generating characteristics and, secondarily, by motoring performance. In generating, the system must convert a raw generator output which varies more than two to one in voltage and frequency to regulated 28 Volts DC. As a motoring system, the electronics must carry out both commutation and motor current regulation.

Several possible schemes exist to accomplish these functions. Three trade-off areas heavily impact the system design. The first of these is method of commutation. Define:

Discrete Commutation: Motor (or generator) commutation by sequentially connected each motor phase to a fixed voltage source such that the desired direction of rotation is attained. Often called "Square Wave Drive".

Continuous Commutation: Effecting sinusoidal current drive by using pulse width modulation (PWM) techniques.

Although simple, there is little place for two phase discretely commutated motors in high efficiency systems due to the third harmonic loss. A three phase approach, however, results in elimination of the third harmonic.

A second area of decision is Integral versus External voltage regulation;

Integral Regulation: Use of pulse width modulation to combine motor/generator commutation with current regulation.

External Regulation: Commutator and voltage regulator are separate entities.

Integral regulation has the advantage of high efficiency since most driver losses are associated with the voltage drop across "ON" semiconductors, and this approach minimizes the number of in series semiconductor switches in a

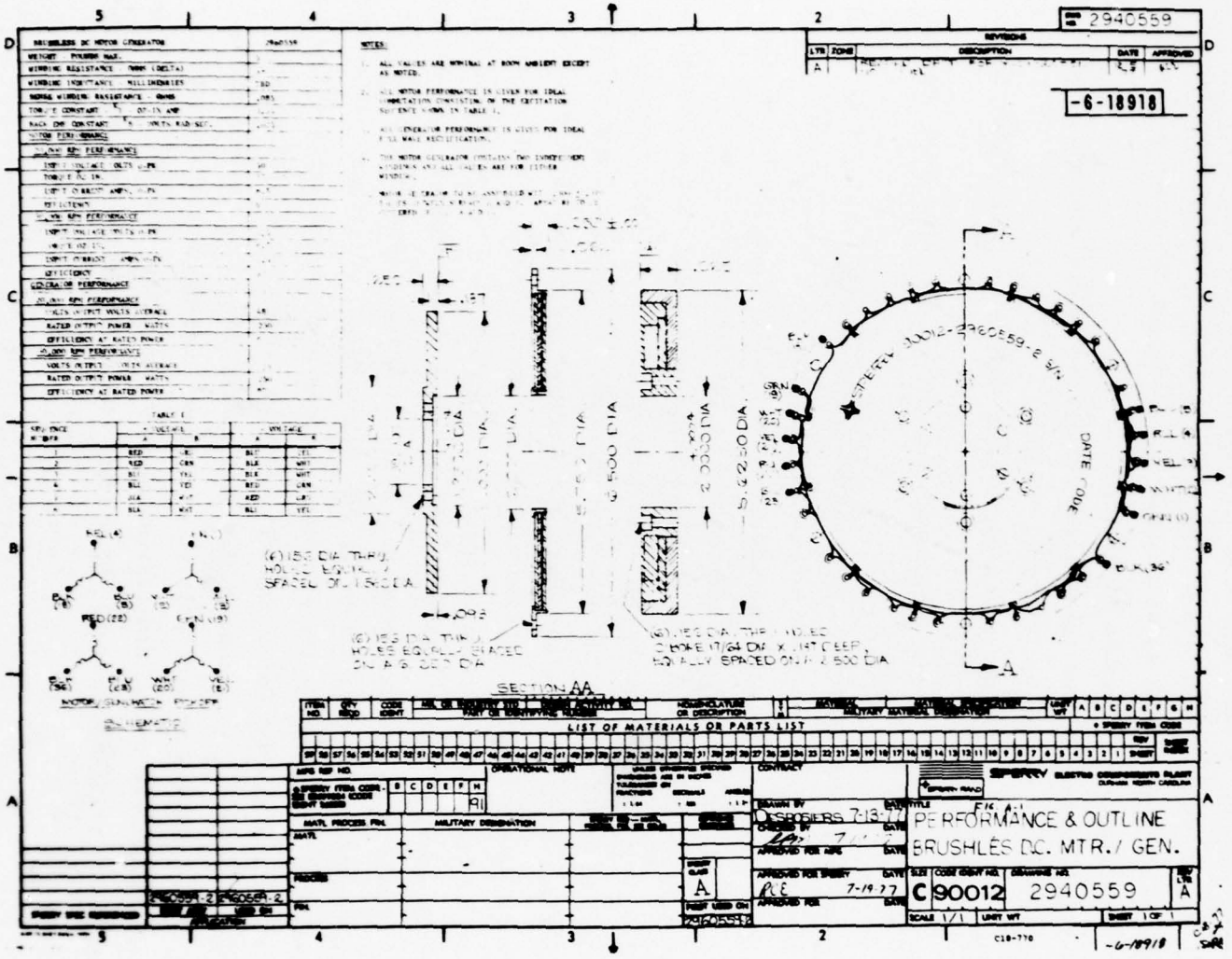


Fig. A-1. Performance and outline drawing of brushless dc motor generator.

system. It should be emphasized that this discussion is limited to digital drive techniques where regulation is accomplished by pulse width modulation such that efficiency is much higher than with a linear type voltage regulator. External regulation frees the commutator to be optimized for the commutation task, such as with very high motor frequencies where the PWM frequency gets too high and switching losses become significant.

The final trade-off, and the one not considered in the proposal, might be called High Voltage versus Low Voltage. Define:

High Voltage System: Motor/Generator peak back emf always higher than the bus voltage (+28 VDC).

Low Voltage System: Motor/Generator back emf always lower than the bus voltage.

SFS has done considerable work with the latter system. As will be shown, the high voltage approach offers excellent efficiencies. A system in which the peak back emf may vary between greater than and smaller than the bus voltage presents formidable implementation problems in the electronic driver.

There are eight combinations of these three parameters that a system might have. Most will be rejected by the following arguments. First, consider Continuous Commutation with the other two choices. Continuous Commutation with External Regulation is redundant since the commutation process itself must regulate the bus voltage to provide sinusoidal motor current. Continuous Commutation in a High Voltage System is possible, but requires a very complex driver to meet the combinations of motoring or generating, instantaneous bus voltage higher or lower than instantaneous back emf, and instantaneous motor current positive or negative. This driver is not only complex, additional switch drops are introduced which lowers its efficiency. Even with considerable effort, a driver circuit could not be conceptualized which did not have bidirectional power switches (switches which could, under control of a low level signal, either block voltages of both polarities or pass current in both directions). Such switches can be built, and consist of two transistors and two diodes each, with up to 2.9 volts drop across the switch. Controlling the switches is also complex.

Because of the additional switch drops, a Low Voltage, Externally Regulated system cannot compete with a Low Voltage system with Integral Regulation. A Discrete, Integral, High Voltage system has many of the problems of a Continuous, Integral, High Voltage System, and can be rejected. A Discrete, Integral, Low Voltage system would be a viable candidate; a three phase version using fewer switches than its two phase, Continuously Commutated, Integrally Regulated, Low Voltage counterpart. The three phase design would be slightly less efficient, however, due to the nonsinusoidal current waveform. In view of Sperry's considerable experience with the two phase approach, this type of discretely commutated system is therefore rejected.

The results of this narrative is summarized in Table A-2. It can be seen that two candidates are left:

Type 4. Discretely Commutated, Externally Regulated, High Voltage System

Type 5. Continuously Commutated, Integrally Regulated, Low Voltage System

The latter's optimal form factor is two phase with "H" bridges for each phase. Sperry experience has been concentrated in that area. The former is new to Sperry.

Figure A-2 gives a conceptual schematic for the new approach. Current sensing techniques are not shown and would have to be worked out. Transistor/rectifier parts Q1/CR1 through A6/CR6 form the commutator for a three phase delta connected motor. As stated previously, the three phase configuration reduces the harmonic content of the discretely commutated drive waveform. The delta format is chosen to minimize commutator requirements in that the delta does not require one of the transistors of a totem pole pair to turn ON just as the other is turning OFF. Many "shunt spike" problems are therefore avoided. The number of motor turns is also maximized with the delta connection. The six diodes full wave rectify the output in the generation mode. The motor interfaces with a high voltage Unregulated Bus which is roughly equal to the peak back emf of the motor.

A pulse width modulated switching regulator with three modes of operation is formed by the remaining semiconductors. A single energy storage inductor,

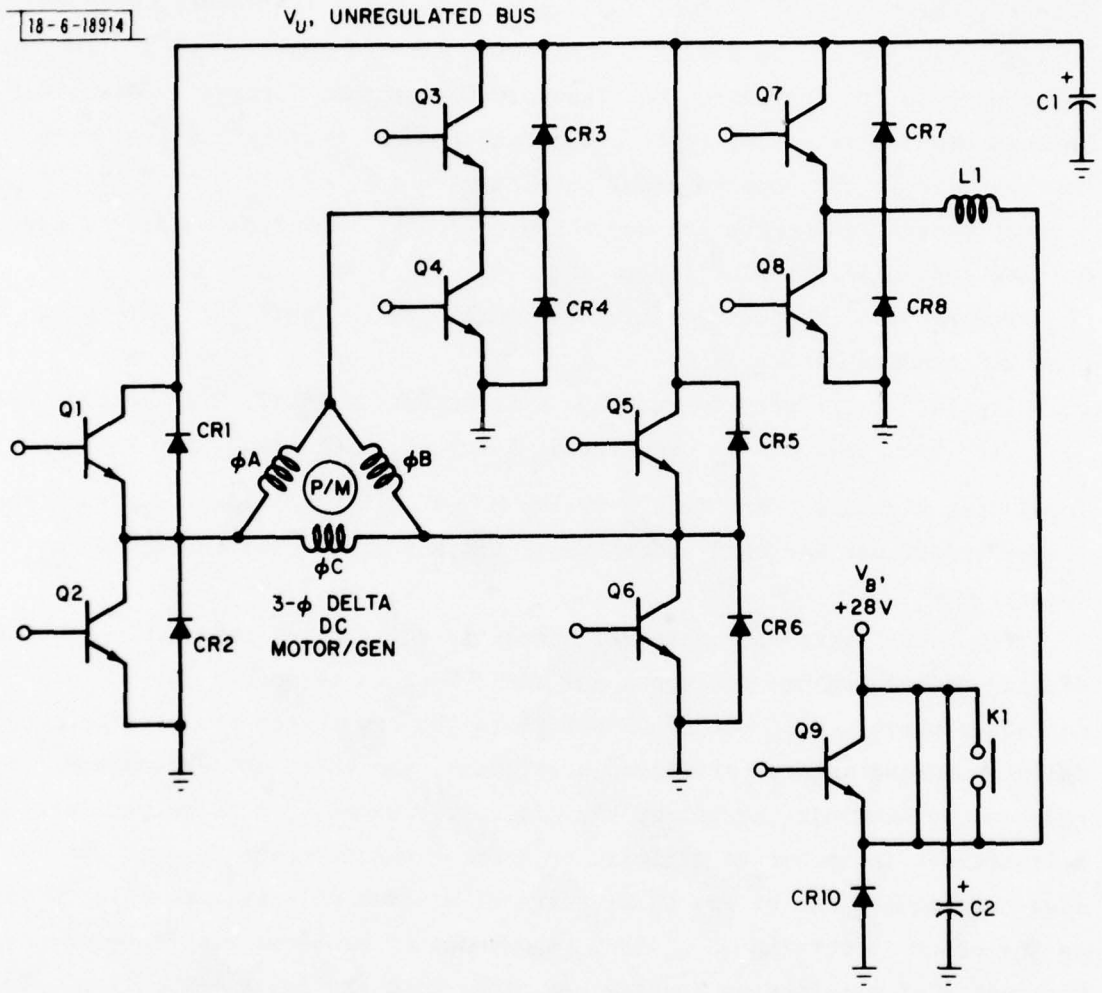


Fig. A-2. High voltage M/G drive concept.

TABLE A-2

SYSTEM CONFIGURATION COMPARISON

Type	System Characteristics (See text)			
	Commutation	Regulation	Voltage	
1	Discrete	Integral	Low	Simpler, but slightly less efficient than 5
2	Discrete	Integral	High	Complex and inefficient driver
3	Discrete	External	Low	Inefficient compared to 5
4	Discrete	External	High	High efficiency--a good candidate
5	Continuous	Integral	Low	Proposal recommendation
6	Continuous	Integral	High	Complex and inefficient driver
7	Continuous	External	Low	Redundant regulation approaches
8	Continuous	External	High	

L1, is used in the regulation operation. When in the generating mode, the system Unregulated Bus is stepped down by the PWM action of Q7, with CR8 acting as the catch diode. When motoring in the normal state of the Unregulated Bus being higher than +28 volts, a pulse width modulator is formed by Q8 and CR7. Finally, Q9 and CR10 form a third pulse width modulator which is only used at system start up when the motor back emf is less than the bus voltage. Since the Q9 modulator is only required at start up, K1 can be used to increase efficiency by bypassing that regulator. CR9 protects Q9 in case K1 is left open and the system returns current to the bus.

The Appendices go through efficiency calculations for each of the two candidate systems. A peak Unregulated Bus voltage of 100 volts was somewhat arbitrarily selected for the High Voltage system, based on existing semiconductor technology and the potential high reliability application. The Low Voltage approach is based on a back emf compatible with a 27 volt minimum bus. Table A-3 presents the results of these calculations. The range of efficiencies for each mode and type is the result of speed dependencies. A 2:1 speed range (75% of available energy extracted) was selected for this comparison. The very attractive generating efficiency of the High Voltage system makes it the prime candidate for implementation. This choice is considerably strengthened by the very high pulse width modulation frequency required with a 50,000 RPM integrally regulated motor and by an initial motor design which revealed difficulty in keeping the motor back emf low enough for the Low Voltage approach.

Although not shown in Fig. A-2, it is likely that additional inductances will have to be added to the commutation circuit to control semiconductor currents as the proposed motor has negligible winding inductance. Alternatively, it might be possible to eliminate C1. Since the winding resistance is also virtually negligible, careful circuit design will be necessary to prevent destructive currents from flowing.

The motor/generator selected is a three phase, delta connected device. The motor/generator will operate over a 2.5:1 speed range (20K or 50K RPM). At 20,000 RPM, the device as a generator must have sufficient average back emf to overcome the bus voltage plus rectifier drops. Using full wave rectification,

TABLE A-3

DRIVER EFFICIENCY COMPARISON

Type / Mode	High Voltage 3Ø	Low Voltage 2Ø
Generating	91-94%	77-88%
Motoring	88-91%	75-86%

that portion of a sine wave encompassing 60 degrees each side of peak is the active waveform to be rectified. The average value of such a waveform is 0.8270 times the peak value. Assuming a 28 volt bus and 3 volts of switch/wiring drop, the back emf at minimum operating speed must then be at least:

$$V_{min} = \frac{28 + 3}{.8270} = 37.5 \text{ volts peak}$$

As an alternative to an auxiliary start-up circuit to accommodate the condition of motor peak back emf less than the bus voltage, start-up could be accomplished by wave width modulating the commutator to limit the current. Efficiency in this mode is unimportant since it is only done once during the flight. This could complicate the low level circuitry somewhat, but eliminates Q9, CR9, CR10, and K1 from Fig. A-2.

Some time was spent looking at wave width modulation techniques for the three phase concept. By using sinusoidal sense winding outputs, it was concluded that speed independent, wave width modulation could be accomplished which was symmetrical, eliminating the third harmonic under all conditions.

A.5 MOTOR/GENERATOR DESIGN

This project presents a challenge in two distinct areas--electromagnetic and mechanical. In arriving at a final design, both areas must be considered. The next section will present a development of the basic equations used in the design of this motor/generator followed by a section on the final design.

A.5.A. Development of Models

The decision to use an external inductor as part of the commutation/regulation electronics makes modeling the inductance of less importance than anticipated in the proposal. The large air gap, absence of iron in the armature, and low permeability of the Samarium cobalt permanent material inherently result in very low inductance which can be neglected in the motor/generator analysis. Thus the primary parameters needed to establish the performance are the winding resistance and the generated back emf. The resistance

calculation is simply a matter of determining the length of the conductor from the geometry of the armature and will not be detailed. The back emf was calculated as follows:

The basic equation for voltage due to a conductor moving in a magnetic field is:

$$e = B\ lV \times 10^{-8} \tag{1}$$

where e = The generated voltage in volts.
B = Magnetic flux density in lines/in^2.
l = Effective length of conductor in B field in inches.
V = Velocity of conductor relative to field in/sec.

the velocity due to rotation is:

$$V = wr \tag{2}$$

w = Angular velocity in rad/sec.
r = Radius in inches.

substituting (2) into (1) and rearranging -

$$\frac{e}{w} = B\ l\ r \times 10^{-8} \tag{3}$$

for multiple conductors

$$K_B = \frac{e}{w} = B\ l\ r\ N/eff \times 10^{-8} \tag{4}$$

For our case, we need only to determine the flux density in the air gap and the effective turns. All basic discussions of permanent magnetic circuits show that minimum magnetic material is required to obtain a specific air gap flux

density if the magnet is operated with a shear slope to give maximum energy product (B x H). We have found at Sperry that the minimum total weight for conventional motors and generator is usually obtained at somewhat higher shear slopes and never at lower. For this design, using an ironless armature resulting in a very large magnetic gap, and requiring substantial sections of non-magnetic material to provide mechanical strength, it is not practical to utilize sufficient length of permanent magnet material to obtain a shear slope significantly greater than 1.0 which is the maximum energy point for Samarium cobalt and this was selected for this design.

The magnet flux density can be determined from the manufacturer supplied demagnetization curve for a B/H of 1 to be 4K Gauss. Some suppliers provide a curve for a "reluctance factor" to reduce the flux and obtain the useful flux. This method or a leakage factor, usually imperically or intuitively obtained, must be used to obtain the "useful" or air gap flux density. Either method results in a factor of 0.8 or an air gap flux density of 4.0 x 0.8 = 3.2 Kilo Gauss or 20 Kilolines per square inch magnetic flux density in the gap.

The effective number of turns is obtained from the final magnetic configuration by determining the maximum number of turns which will be located in the B-field. Using this number of turns will give the peak back emf.

The major mechanical design problem was to contain the rotating permanent magnets at speeds of 50,000 RPM. The analysis of the stresses in the rotor were conducted using standard methods, primarily from Roark's book, "Formulas for Stress and Strain".

A.5.B. Final Design Parameters

1. Electromagnetic Design and Performance Calculations

The electronic interface analysis (Section A.4) defined a three-phase motor/generator with a voltage of 37.5 volts peak minimum at 20,000 RPM or a back emf constant of -

$$K_B = \frac{37.5}{20{,}000 \times .1047} = .018 \text{ Volts/Rad/Sec minimum}$$

For maximum efficiency, the winding resistance should be minimum.

Analysis of Generator Losses

The major losses in a conventional permanent magnet generator are:

- Stator or Armature I^2R losses
- Fundamental Frequency Iron losses (Eddy Current and Hysteresis)
- High Frequency Iron losses

For the ironless armature design, the fundamental iron loss is nonexistent. The high frequency iron loss is caused by pulsations of the flux as the magnet rotates past the slot openings. This is also nonexistent. At the high frequency encountered at high speed, consideration must be given to increased resistance of the conductors due to skin effect. Also since the conductors are located directly in the flux field, the effect of eddy current losses must be evaluated.

The losses to be considered then are the armature I^2R losses and eddy current losses in the conductors. The original concept for the winding was a delta connected winding using five active poles for each redundant half and one pole for each sense winding. After some preliminary measurements of air gap flux density showed approximately 10% variation from the magnet surface to the return path, it was concluded that the windings should be connected in wye to eliminate the possibility of losses due to circulating currents.

Attempts to calculate the eddy current losses due to the changing flux density proved fruitless. By using several "reasonable" assumptions, the calculated losses varied from neglectible to greater than rated output. A test was conducted to determine if these losses were significant. A toroidal core of laminated nickel iron was fabricated as follows:

Outside Diameter	6 inches
Inside Diameter	4-7/8 inches
Length	11/16 inches
Slot	1/16 inch
Turns	100
Resistance	0.4 ohm
Inductance	3.92 mH

Tests were conducted to determine the flux density in the gap versus current as follows:

Input Current	Gap Flux Density
0.25	270 Gauss
0.50 Amp	553 Gauss
0.75 Amp	818 Gauss

Tests were then made to measure the input power when excited at 2000 Hertz and 5000 Hertz with nothing in the gap, with one of the coils wound with Litz wire, with a coil wound with solid wire, and with a sheet of aluminum foil. The current was set at .65 amp rms to give a gap density of 1KG peak. The increase in power as the various samples were placed in the air gap is tabulated below:

IN GAP	INCREASED POWER AT 2K HZ	INCREASED POWER AT 5K HZ
Nothing	0	0
Coil of Litz Wire	<.03	<.03
Coil of Solid Wire	<.03	<.03
.002 Th. Aluminum Foil	>2.0	>4.0
.005 Th. Aluminum Foil	>4.0	>8.0

In the above test, no increase in power could be measured with the generator coils, either using solid wire or Litz wire. The resolution of the meter was approximately .03 watts. As a worst case, then, the eddy current losses will be:

$$\text{Max. Losses} = \left(\frac{B}{1.0}\right)^2 \times \text{Number of Coils} \times .03$$

$$\text{Max. Losses} = \left(\frac{3.2}{1.0}\right)^2 \times 12 \times .03 = 3.7 \text{ Watt}$$

The increase in resistance due to skin effect for solid wire is:

SPEED	AC RESISTANCE
20,000	1.2 x Rdc
50,000	2.25 x Rdc

With forty strand Litz wire, the increase in resistance is neglectible. A summary of the calculated parameters for the generator is tabulated in Table A-4 using tested values for selected parameters. This table shows that the generator efficiency is 92.9% at 20,000 and 97.6% at 50,000 RPM using the worst case eddy current losses. These calculations are based on one of the two redundance windings.

Performance as a motor is summarized in Table A-5 using the same basic parameters. This table shows that the motor efficiency is comparable to the generator under the condition of 250 watts constant output power. If it is assumed that the duty cycle specified in "Specification for Flywheel Motor-Generator Design" is used and the average torque for constant acceleration is used, the efficiency drops to 84% at 20,000 RPM, 93% at 50,000 RPM, or 88.6% average efficiency. The primary loss in this case is the eddy current loss of 3.7 watts which is a worst case number and is likely high.

2. Mechanical Design and Stress Calculations

The motor generator consists of three separate pieces--the armature or stator, the permanent magnet rotor, and the return path. See Outline Drawing in Fig. A-1. The construction of each of these will be discussed separately below.

a. The Armature

The armature is fabricated using three coil forms made of epoxy impregnated fiberglass to hold and provide proper spacing of the twelve wound coils. The coils are wound on a special form to give the same shape as the coil form and are impregnated prior to removing from the winding form. After the coils are assembled and bonded to the coil forms, the three stages are located in an aluminum bracket and the coils are connected

TABLE A-4

GENERATOR PERFORMANCE

PARAMETER	UNITS	CALCULATED VALUE
Winding Resistance	Ohms	.39
Back emf - K_B	Volts/Rad/Sec	.023
Inductance	Microhenries	15
At 20,000 RPM		
Generator Voltage	Volts Peak	48.1
Average Voltage	Volts Peak	39.8
Current at 250 Watts	Amps DC	6.28
I^2 R Losses	Watts	15.5
Eddy Current Losses	Watts	3.7
Total Losses	Watts	19.2
Efficiency	%	92.9
At 50,000 RPM		
Generated Voltage	Volts Peak	120.4
Average Voltage	Volts DC	99.6
Current at 250 Watts	Amps	2.51
I^2 R. Losses	Watts	2.46
Eddy Current Losses	Watts	3.7
Total Losses	Watts	6.16
Efficiency	%	97.6
Average Efficiency	%	96%

TABLE A-5

MOTOR PERFORMANCE

PARAMETER	UNITS	CALCULATED VALUE
Winding Resistance	Ohms	0.39
Back emf - K_B	Volts/Rad/Sec	.023
Inductance	Micro Ohms	15
Torque Constant	Oz. In/Amp	3.26
Average Torque for 10 Hr. Run-up	Oz. In.	1.35
At 20,000 RPM, 1.35 Oz.-In.		
Generated Voltage	Volts Peak	48.1
Input Current	Amps	.414
I^2R Losses	Watts	.067
Eddy Current Losses	Watts	3.7
Total Losses	Watts	3.77
Output Power	Watts	20
Efficiency	%	84.1
At 20,000 RPM, 250 Watts		
Generated Voltage	Volts Peak	48.1
Input Current	Amps	6.28
I^2R Losses	Watts	15.4
Eddy Current Losses	Watts	3.7
Total Losses	Watts	19.1
Output Torque	Oz. In.	16.9
Efficiency	%	92.9
At 50,000 RPM, 1.35 Oz.-In.		
Generated Voltage	Volts Peak	120.4
Input Current	Amps	.414
I^2R Losses	Watts	.067
Eddy Current Losses	Watts	3.7
Total Losses	Watts	3.77

TABLE A-5 (Continued)

PARAMETER	UNITS	CALCULATED VALUE
Output Power	Watts	50
Efficiency	%	93
At 50,000 RPM, 250 Watts		
Generated Voltage	Volts 0-Peak	120.4
Input Current	Amps	2.52
I^2R Losses	Watts	2.48
Eddy Current Losses	Watts	3.7
Total Losses	Watts	6.18
Output Torque	Oz.-In.	6.77
Efficiency	%	97.6
Average Efficiency at 1.35 Oz-In.	%	88.6
Average Efficiency at 250 Watts Out	%	94.5
Sense Coil		
Resistance	Ohms	.05
Back emf Constant - K_B	Volts/Rad/Sec	.005

using press fit terminals around the outer land of the bracket. The jumpers and connectors are insulated and protected with a polyurethane coating. The coil assembly is then potted using a heavily filled epoxy.

b. The Return Path

The return path is machined from a high strength stainless steel and heat treated for maximum strength.

c. The Permanent Magnet Rotor

The permanent magnet rotor presented the primary challenge to the mechanical design. After several false starts, the final design was selected to consist of a high strength titanium ribbed structure to contain the magnetics on five sides, a magnetic plate containing the magnets on the final side and providing a return path, and a final titanium ring with a shrink fit to share the stress load. The sketch in Fig. A-3 shows the general construction of this member. Some of the key design points are:

- Outer surface of magnet flat to distribute load
- Magnets bonded at OD only (i.e., All stresses are compressive)
- Return path supported at ID only (i.e., does not induce any stress load in Ti housing).
- Magnet is contained on all sides.

Appendix 3 contains the Rotor Stress Analysis. A summary of the stresses are shown in Table A-6.

TABLE A-6

STRESS SUMMARY

SECTION	MAXIMUM STRESS (KPSI)
Magnetic	17.7 (Compresses)
Outer Ring	94.2 (Tension)
Ribs	50 (Tension)
Inner Hub	42 (Tension)

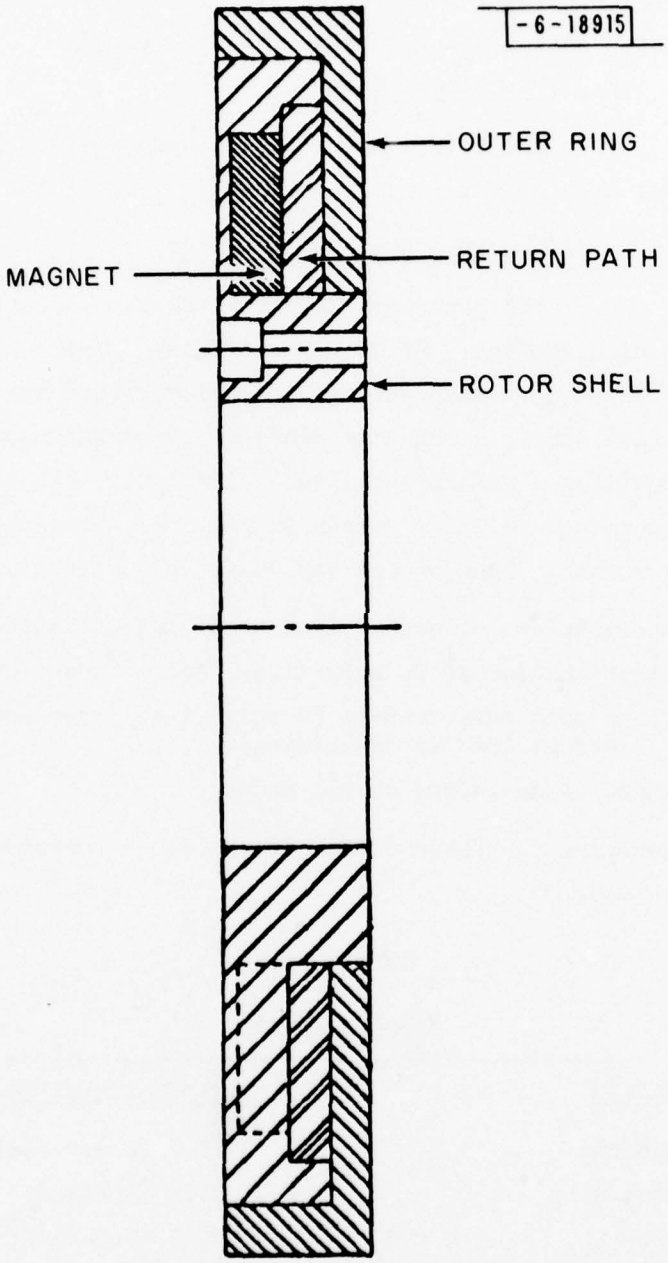


Fig. A-3. Construction of rotor.

WEIGHT

The calculated weight for the motor generator is four pounds with a breakdown as follows:

ITEM	WEIGHT
Rotor Shell	1.0
Magnet Plate	.42
Magnets	.42
Outer Ring	.87
Total Magnet Rotor	2.71
Return Path	.71
Wire	.20
Coil Form	.15
Coil Bracket	.16
Potting and Miscellaneous	.1
Total Stator	.61
TOTAL	4.03

A.6 COMMENTS ON SAMPLE FABRICATION

In general, the sample worked out well as designed with only minor corrections being required. The major item which will require changing, if additional units are built, is to increase the diameter of the armature flange to allow more room for the wire terminations. Difficulty was encountered in trying to contain this wire and it was necessary to omit sleeving from these jumpers on the breadboard unit.

Material substitutions were made on this unit to use material in stock at Sperry. Thus, the rotor housing is fabricated from 304 Stainless Steel rather than Titanium and the magnetic plates are 416 steel rather than 440C. These substitutions would prevent any high speed test.

The test performed on the sample at Sperry consisted of measuring:

Resistance
Inductance
Back emf constant
Wave shape

A summary of these data is presented in Table A-7 and Figs. A-4 and A-5. Photos of the engineering unit are shown in Figs. A-6 through A-8.

TABLE A-7

TEST DATA ON BREADBOARD UNIT

TERMINALS	RESISTANCE (Ohms)	INDUCTANCE (mH)	K_B (V/Rad/Sec)
Blk (18) - Red (5)	.396	.0344	.0239
Red (5) - Blu (4)	.397	.0358	.0243
Blu (4) - Blk (18)	.399	.0347	.0244
Blk (36) - Red (23)	.388	.0353	.0247
Blu (22) - Blk (36)	.385	.0338	.0246
Wht (2) - Yel (3)	.0853	.0094	.00499
Yel (3) - Grn (1)	.0841	.0089	.00490
Grn (1) - Wht (2)	.0858	.009	.00488
Wht (20) - Yel (21)	.090	.009	.00499
Yel (21) - Grn (19)	.085	.009	.00495
Grn (19) - Wht (20)	.087	.0091	.00488

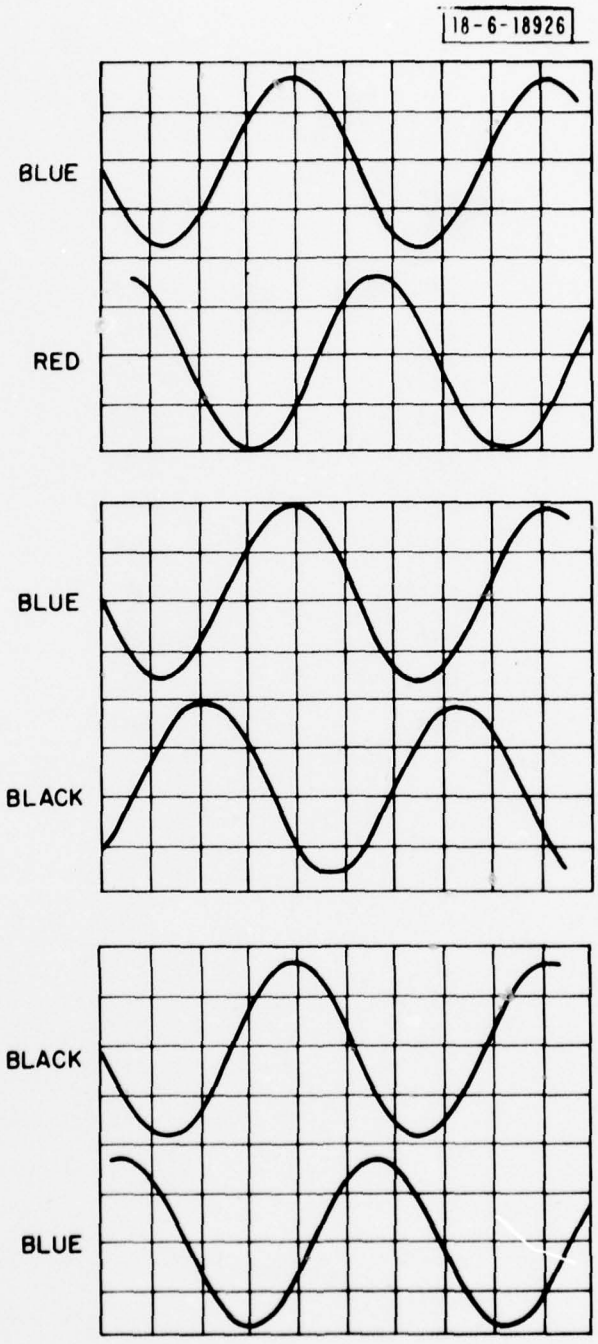
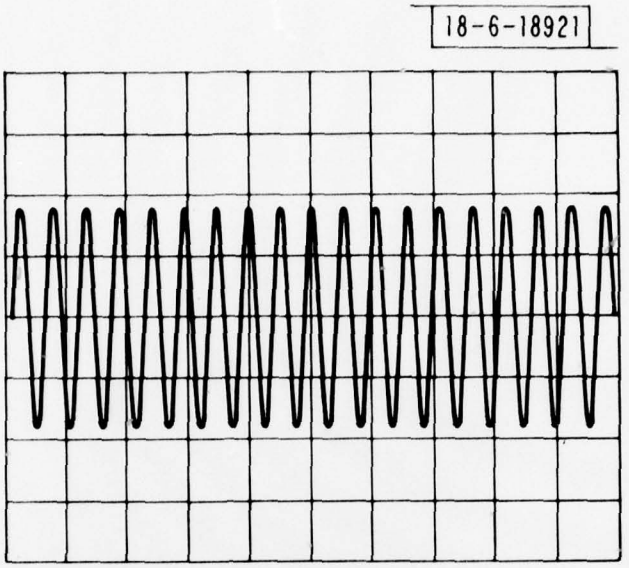


Fig. A-4. Output voltage waveshape and phasing.



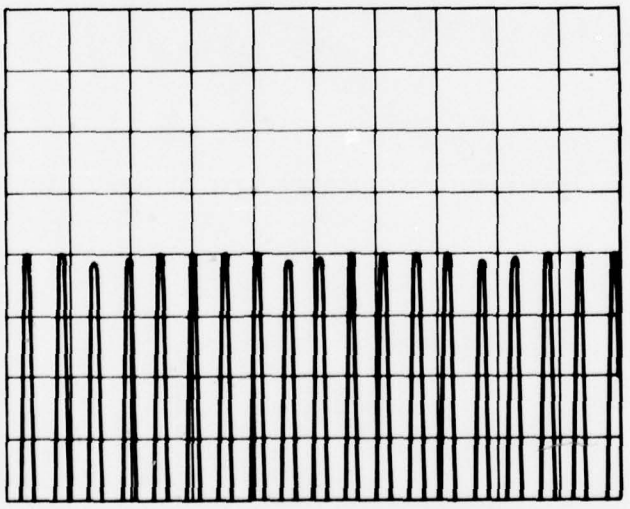


Fig. A-5. Output uniformity.

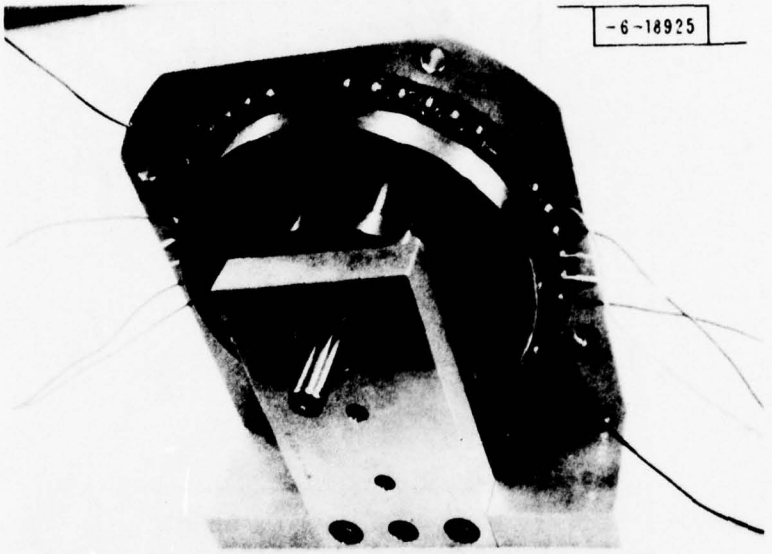


Fig. A-6. Breadboard unit in test fixture.

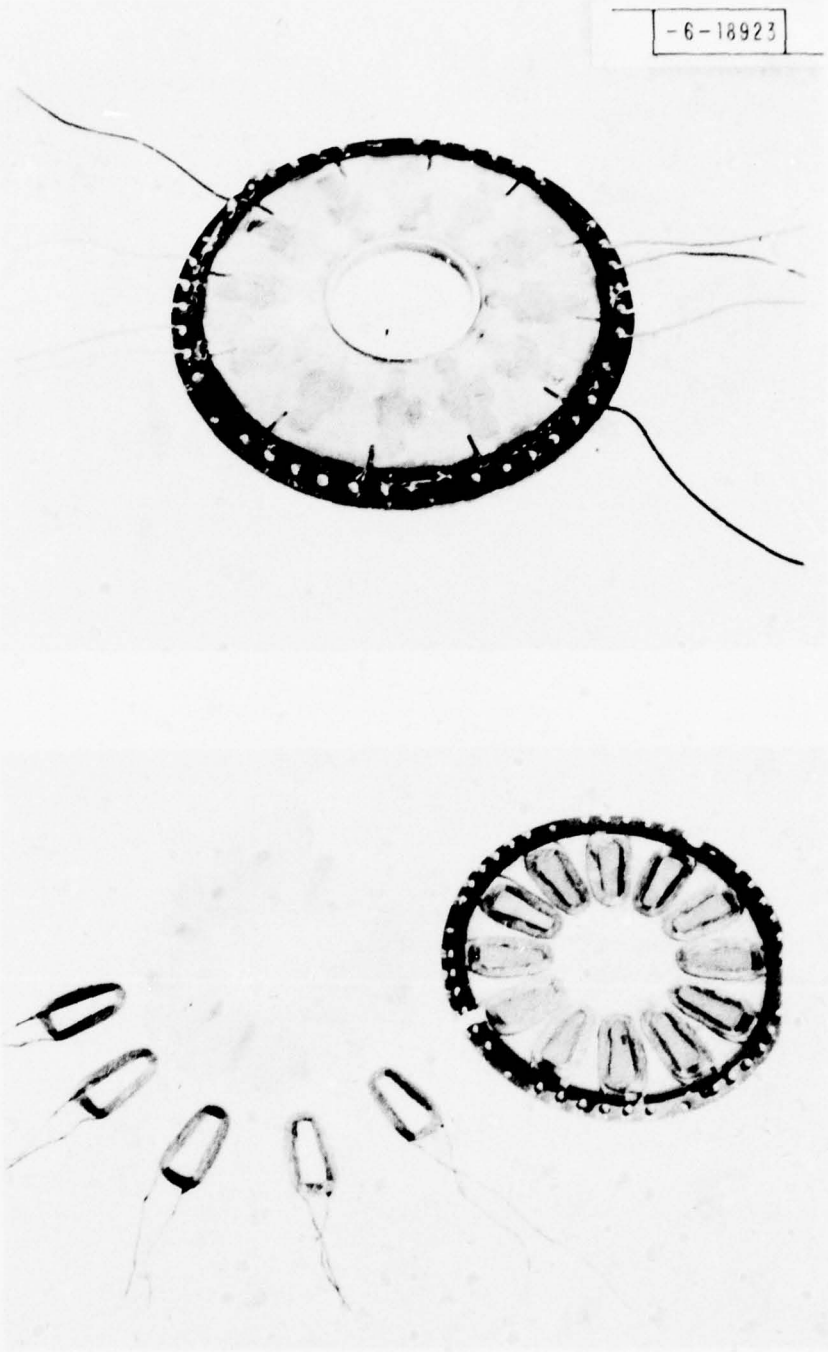


Fig. A-7. Stator for breadboard unit.

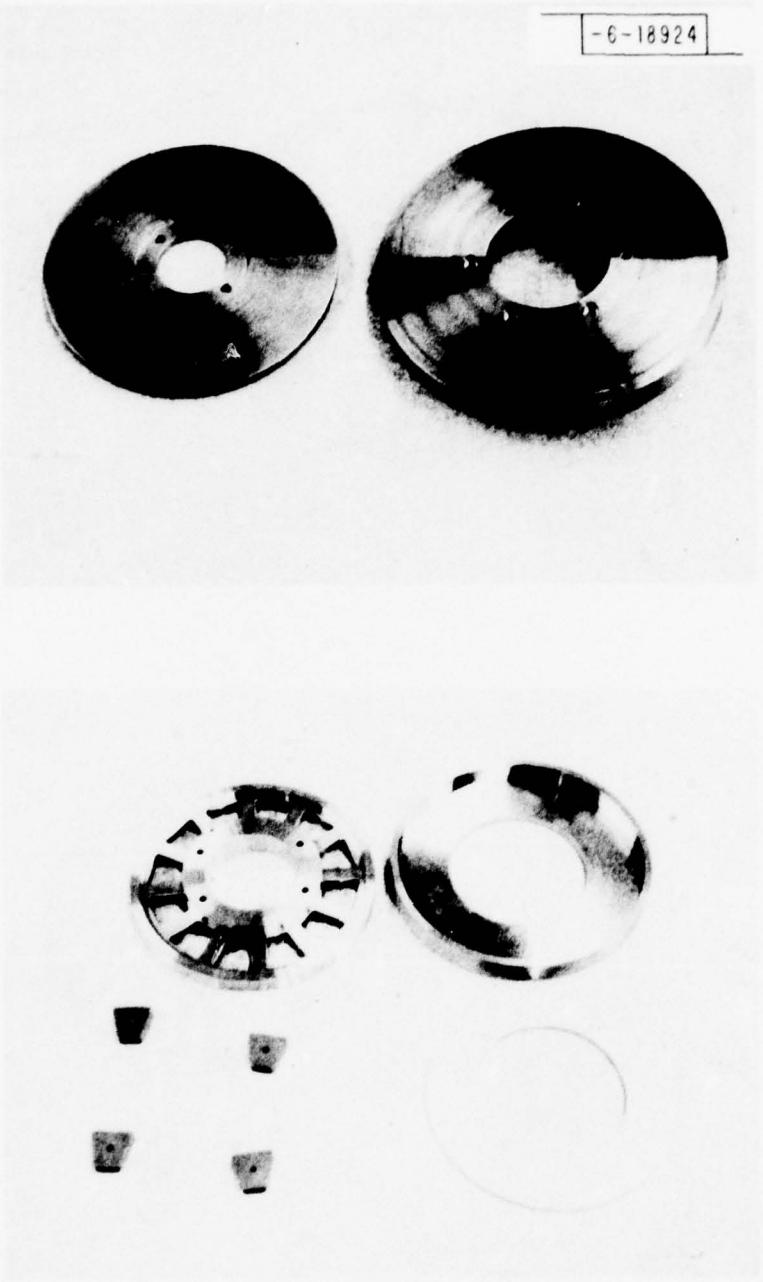


Fig. A-8. Rotor for breadboard unit.

A.7 Two-Phase Continuously Commutated Efficiency Calculations

TWO PHASE BACK EMF < 28V EFFICIENCY

A. Motoring

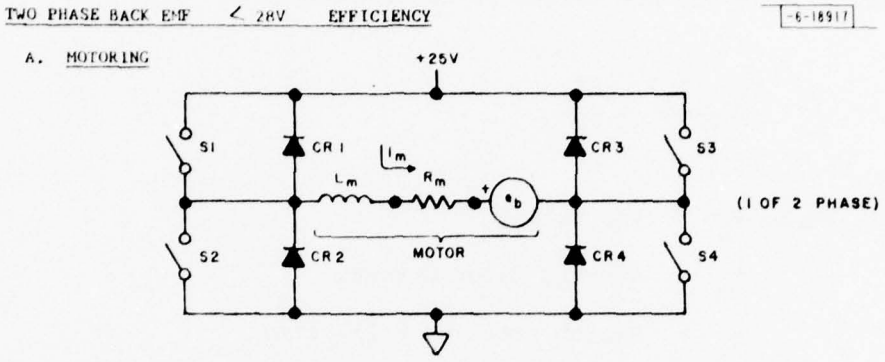


Fig. A-9. Motoring diagram.

Sinusoidal current is pumped through the motor by holding S4(S2) on and Pulse Width Modulating S1(S3) (Parentheses mode is negative current flow; S1-S4 is defined as positive current flow.) Consider the positive half cycle. Assume that the average of switch drop and catch diode drop is 1.5V. Therefore, the average switching voltage drop is always twice that, or 3.0 Volts.

The power delivered to the motor which is converted to mechanical power is $i_m e_b$, where e_b is the motor back emf:

$$e_b = K_b \omega \text{ SIN } \omega T$$

Where K_b = Back emf constant in volts/rad/sec.

ω = Motor rotational velocity in rad/sec.

The motor copper loss is $i_m^2 R_m$.

And the switch voltage drop loss is $i_m V_D$

Where V_D = Average switch drop

= 3.0 Volts as discussed above.

It is further assumed that the driver loss due to switching transients is negligible. This is a warranted assumption. Without going through the derivation, the loss in any one switch is approximately

$$\frac{V_B \cdot i_m}{6} \cdot \frac{2t_r}{T}$$

Where V_B = Bus Voltage

i_m = Average Motor Current

t_r = Switch rise (or fall) time

T = PWM period

It can easily be shown that $i_m = \frac{2}{\pi} I_{pk}$

Where I_{pk} is the peak motor current.

$$i_m = I_{pk} \text{ SIN } \omega T$$

$$i_m = \frac{I_{pk}}{\pi} \int_0^{\pi} \text{SIN } \omega T \, dwt - \frac{I_{pk}}{\pi} \text{ COS } \omega T \Big|_0^{\pi} = \frac{2}{\pi} I_{pk}$$

Note that i_m is selected to be in phase with the back emf. This results in maximum efficiency.

Taking both SIN and COS phases into account:

Pout = Mechanical Output Power = $e_{b_s} \; i_{m_s} + e_{b_c} \; i_{m_c}$

Where e_{b_s} = Back EMF for SIN winding

i_{m_s} = Motor Current in SIN winding

e_{b_c} = Back EMF for COS winding

i_{m_c} = Motor Current in COS winding

$$\text{Pout} = (K_b\ \omega\ \text{SIN}\ \omega T)\ (I_{pk}\ \text{SIN}\ \omega T) + (K_b\ \omega\ \text{COS}\ \omega T)\ (I_{pk}\ \text{COS}\ \omega T =$$

$$K_b\ \omega\ I_{pk}\ (\text{SIN}^2\ \omega T + \text{COS}^2\ \omega T) = K_b\ \omega\ I_{pk}$$

Motor Losses (ignoring iron loss) = Pml =

$$\text{Pml} = i_m{}^2 R_m$$

$$\text{Pml} = \frac{R_m}{\pi} \int_0^{\pi} i_m{}^2\ dwt = \frac{R_m}{\pi}\ I_{pk}{}^2 \int_0^{\pi} \text{SIN}^2\ \omega T\ dwt$$

$$= \frac{R_m\ I_{pk}{}^2}{\pi}\ [1/2\ \omega T - 1/4\ \text{SIN}\ 2\ \omega T]\ \Big|_0^{\pi}$$

$$= \frac{R_m\ I_{pk}{}^2}{\pi}\ \left[\frac{\pi}{2}\right] = \frac{R_m\ I_{pk}{}^2}{2} \qquad \text{(Per Phase)}$$

And driver loss = P_{dl} is:

$$P_{dl} = i_m\ V_D$$

$$P_{dl} = \frac{V_D}{\pi} \int_0^{\pi} I_{pk}\ \text{SIN}\ \omega T\ dwt = \frac{2\ V_D\ I_{pk}}{\pi} \qquad \text{(Per Phase)}$$

$$\text{Bus Power} = P_B = \text{Pout} + \text{Pml} + P_{dl}$$

$$= K_b \omega\ I_{pk} + R_m\ I_{pk}{}^2 + \frac{4}{\pi}\ V_D \pm I_{pk}.$$

$$= I_{pk}\ [K_b \omega + R_m\ I_{pk} + \frac{4}{\pi}\ V_D]$$

And Driver Efficiency =

$$= N_D = \frac{\text{Pout} + \text{Pml}}{P_B} \times 100\%$$

$$= N_D = \frac{K_B \omega + R_m\ I_{pk}}{K_B \omega + R_m\ I_{pk} + \frac{4}{\pi}\ V_D}$$

For further simplification, assume Pml = 0

$$\text{Then } N_D = \frac{K_B\omega}{K_B\omega + \frac{4}{\pi} V_D}$$

With the assumption that switch and diode drags are equal (in reality, diode drop is $\approx$1V and switch drop is $\leq$ 1.9V), the same equation applies to generation. Referring back to Fig. 1, generation is accomplished by maintaining --

$$i_m = I_{pk} \text{ SIN } \omega T$$

This is done by opening all switches except S4(S2), which is pulse width modulated. On closing, the motor is effectively shorted, and im builds up. On opening, the energy stored in L_M provides an output to the bus via CR3 (CR1), even though the back emf is less than the bus voltage. Generating, in general, will be slightly more efficient than motoring because of the substitution of a diode drop for a switch (transistor) drop in the former case. ($\approx$ 2% higher)

So, let's design a motor. The back emf must always be less than the bus voltage minus switch drops so that motoring may be accomplished.

Set $V_{B(min)}$ = 27 Volts

V_D = 3 Volts

V_F = Wiring, Filter Drop = 1 V N.C.

Then $e_{b(max)}$ = $K_B\omega W$ max. = 27-3-1 = 23 Volts

If ω min = $\frac{\omega_{max}}{2}$

Then $K_B\omega_{min}$ = 11.5 Volts

And:

$$\frac{K_B\omega \text{ min}}{K_B\omega \text{ min} + \frac{4}{\pi} V_D} \times 100\% \leq N_D \leq \frac{K_B\omega \text{ max}}{K_B\omega \text{ max} + \frac{4}{\pi} V_D} \times 100\%$$

$$\frac{11.5}{11.5 + \frac{4}{\pi} .3} \times 100\% \leq N_D \leq \frac{23}{23 + \frac{4}{\pi} .3} \times 100\%$$

$$75\% \leq N_D \leq 86\%$$

Readdressing switching time losses:

N_S = Switching time efficiency

$$\simeq = \frac{K_B\omega}{K_B\omega + \frac{2V_B}{\pi .6} \frac{.2\ tr}{T}} \times 100\%$$

If T = 50 M sec

tr = 1 M sec

Then, at $K_B\omega$ min; $N_S = \frac{11.5}{11.5 + \frac{56}{6\pi} \cdot \frac{2}{50}} \times 100\% = 99\%$

A.8 Three-Phase, Discretely Commutated Efficiency Calculations

THREE PHASE EFFICIENCY

Definitions

V_B = Bus voltage, nominalcy +28V

V_U = Unregulated, or Motor/Generator bus voltage.

K_B = Back EMF constant, V/Rad/Sec.

W = Rotational Velocity, Rads/Sec.

V_T = Voltage drop across transistor switch, $\leq$ 1.9V.

V_D = Voltage drop across diode, $\leq$ 1.0V.

I_B = +28V Bus current.

I_M = Motor (unregulated bus) current.

N = Efficiency, with subscripts delineating commutator, regulator, generating, and motoring modes, i.e.: N_{cg} indicating efficiency of the commutation in the generating mode.

THREE PHASE EFFICIENCY (Neglecting external inductor losses)

A. Motoring

1. Commutating Efficiency, N_{cm}

$$N_{cm} = \left(1 - \frac{2V_T}{V_U}\right) \times 100\%$$

2. Regulator efficiency, N_{rm}

Q8 and CR7 form the pulse width modulator in this mode.

Q8 is on $1 - \frac{V_B}{V_U}$ of the time

CR7 is on $\frac{V_B}{V_U}$ of the time

Losses are $\pm I_B \left[V_T \left(1 - \frac{V_B}{V_U}\right) + V_D \frac{V_B}{V_U}\right]$

Total Power is $V_B I_B$

$$\text{so } N_{rm} = \left\{ 1 - \frac{\left[V_T \left(1 - \frac{V_B}{V_U}\right) + V_D \frac{V_B}{V_U}\right]}{V_B} \right\} \times 100\%$$

so combined motoring efficiency, N_M is:

$$N_M = \left\{ \left(1 - \frac{2\ V+}{V_U}\right) 1 - \frac{\left[V_T \left(1 - \frac{V_B}{V_U}\right) + V_D \frac{V_B}{V_U}\right]}{V_B} \right\} \times 100\%$$

Now,

$$V_U = K_B \omega$$

Realizing the state-of-the-art in semiconductor technology, combined with the potential high-reliability application, set $V_{U\ (Max.)} = 100$ volts. If $\omega_{min} = 1/2\ \omega_{max}$, then $50 \leq V_U \leq 100V$. For ω_{min}:

$$N_M = \left\{\left(1 - \frac{2.1.9}{50}\right)\left[\frac{1 - \left[1.9\ (1 - \frac{28}{50}) + 1.0\ (\frac{28}{50})\right]}{28}\right]\right\} \times 100\%$$

$$= (.924)\ (1 - \frac{.836 + .56}{28}) \times 100\%$$

$$= (.924)\ (.950) \times 100\% = 88\%$$

For ω_{max},

$$N_M = (1 - \frac{2.19}{100})\ \ 1 - \frac{(1.9\ (1 - \frac{28}{100}) + 1.0\ (\frac{28}{100})}{28} \times 100\%$$

$$= (.962)\ (1 - \frac{1.368 + .28}{28}) \times 100\%$$

$$= (.962)\ (.941) \times 100\% = 91\%$$

B. Generating

1. Commutation Efficiency, N_{cg}

$$N_{cg} = \left(1 - \frac{2V_D}{V_U}\right) \times 100\%$$

2. Regulator Efficiency, N_{rg}

Q7 and CR8 form the pulse width modulator in this mode.

Q7 is on $\frac{V_B}{V_U}$ of the time.

CR8 conducts $1 - \frac{V_B}{V_U}$ of the time.

Losses are

$$I_B \left[V_T \frac{V_B}{V_U} + V_D \left(1 - \frac{V_B}{V_U} \right) \right]$$

Total output power is $V_B I_B$, so

$$N_{rg} = \left\{ 1 - \frac{\left[V_T \frac{V_B}{V_U} + V_D \left(1 - \frac{V_B}{V_U} \right) \right]}{V_B} \right\} \times 100\%$$

and combined efficiency, N_G is:

$$N_G = \left\{ \left(1 - \frac{2V_D}{2_{V_U}} \right) \; 1 - \frac{\left[V_T \frac{V_B}{V_U} + V_D \left(1 - \frac{V_B}{V_U} \right) \right]}{V_B} \right\} \times 100\%$$

For ω_{min}:

$$N_G = \left\{ (1 - \frac{2.1}{50}) \left[1 - \frac{\left[1.9 \frac{28}{50} + 1.0 \; (1 - \frac{28}{50}) \right]}{28} \right] \right\} \times 100\%$$

$$= (.960) \; (1 - \frac{1.064 + .44}{28}) \times 100\%$$

$$= (.960) \; (.946) \times 100\% = 91\%$$

For ω_{max}:

$$N_G = \left\{ (1 - \frac{2.1}{100} \left[1 - \frac{\left[1.9 \frac{28}{100} + 1.0 \; (1 - \frac{28}{100}) \right]}{28} \right] \right\} \times 100\%$$

$$N_G = (0.98) \; (1 - \frac{.532 + .72}{28}) \times 100\%$$

$$= (.98) \; (.955) \times 100\% = 94\%$$

A.9 Rotor Stress Calculations

STRESSES

Rotational Stress

O.D. = 5.3

I.D. = 4.875

Δ = .175

R = 2.544

W = 5235 rad/sec.

$$S = \frac{\Delta R^2 W^2}{386.4} \quad \text{(page 360)}$$

$$= \frac{.175 \times 2.544^2 \times 5235^2}{386.4}$$

$$S = 80.3\ K_{psi}$$

Mass of Magnet

$$W = \frac{.85 + .45}{2} \times .75 \times .25 \times .29 = .0353 \text{ lb. each}$$

$$F = M\gamma W^2 = \frac{W\gamma W^2}{g}$$

$$= \frac{.0353 \times 1.5 \times 5235^2}{386.4} = \underline{3.755 \text{ Klb.}} \text{ each}$$

Case 6, Page 217

$$S_{max} = \frac{3W}{4\pi t^2}$$

$$W = \text{Unit Load} = \frac{3.755 \times 10^3}{.85 \times .25} = 17.67 \text{ K psi}$$

$$t = .385$$

$$S_{r\ max} = \frac{3 \times 17.67}{4\pi \times .385^2} = 28.46 \text{ K psi}$$

$$st = \frac{3W}{4\pi t^2} = \frac{S_{r\ max}}{m} = \frac{28.46}{3} = 9.5$$

$$m = 1/V = 3$$

Totals

$$St = 80.3 + 9.5 = 89.8$$

$$S\gamma = 28.46$$

$$S = \sqrt{89.8^2 + 28.46^2}$$

$$S = 94.2$$

In Ribs

$$\sigma = \frac{F}{A} = \frac{3.755 \text{ K psi}}{.3 \times .25}$$

$$\sigma = 50.06$$

Inner Hub

Rotational

O.D. = 3.0

I.D. = 2.0

L = .625

$\partial = .175$

$\gamma = 1.25$

$t = .5$

$W = 5235$

$$S = \frac{\partial R^2 W^2}{386.11}$$

$$= \frac{.175 \times 1.25^2 \times 5235^2}{386.4}$$

$S = \underline{19.39 \text{ Kpsi}}$

Case 9, Page 174

Max. Tension = 1/2 W COT θ

$$= 1/2 \times \frac{3.755 \times}{\tan 15^\circ} = 7.01 \text{ Klb.}$$

$\sigma = T/A$

$$= \frac{7.0 \text{ Klb.}}{.625 \times .5} = \underline{22.4 \text{ Kpsi}}$$

Total 22.4 + 19.39 = $\underline{41.8}$ O.K.

STRESS ON MAGNET

$F = 3.755$ K each

$A = .850 \times .250 = .2125$

$\sigma = F/A = 17.7$ Kpsi. compressure

VS 42

NOTE: All page numbers and case numbers refer to: Formulas for Stress and Strain, R. J. Roark (McGraw Hill Publishing Company) Fourth Edition, 1965.

A.10 Addendum--Final Report

MAGNETIC CIRCUIT

The magnetic circuit is designed to utilize the high coercivity of Samarium cobalt. As a result, manufacturing tolerances and rotor-stator clearances do not appreciably affect performance. Figure A-10 shows the basic magnetic circuit including the dimensions affecting the magnet operating point.

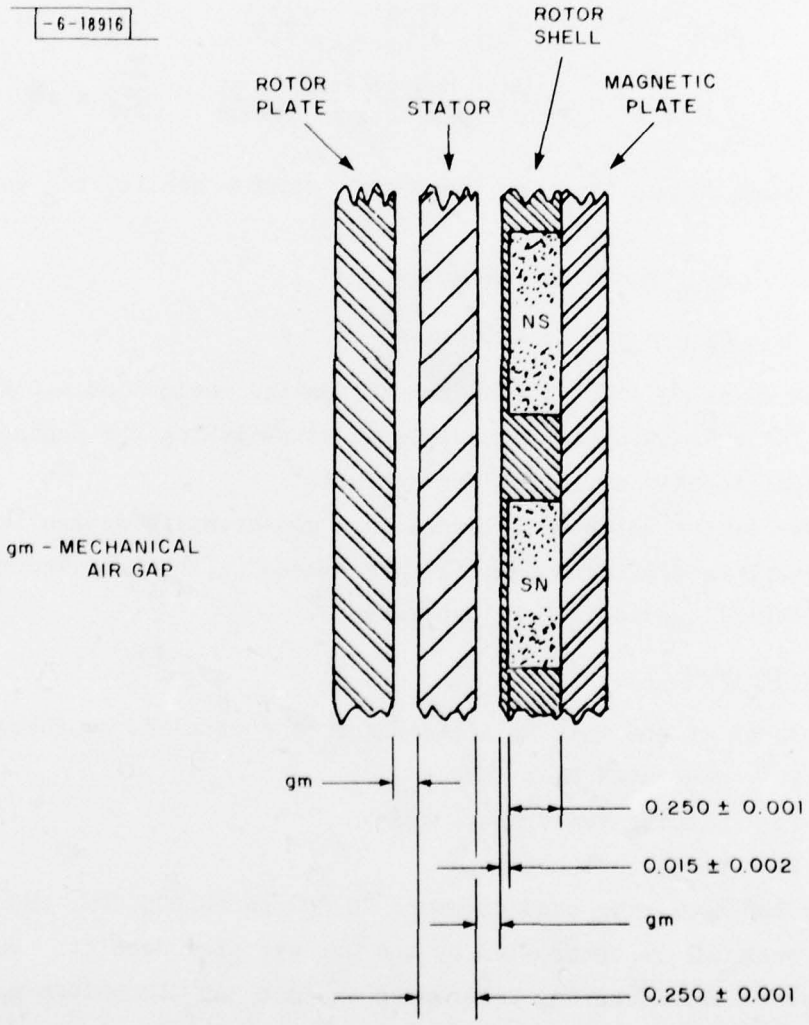


Fig. A-10. Magnetic circuit.

The effective magnetic air gap is the sum of the rotor shell covering the magnet, the stator thickness, and 2 gm. For purposes of analysis, the mechanical air gap is assumed to be .020 ± .005. From worst case tolerances, the magnetic air gap is:

Min. Gap = 0.292 in.

Max. Gap = 0.318 in.

Thus, the extremes of magnet operation are:

$$\text{Min. B/H} = \frac{\text{Min. Magnet Length}}{\text{Max. Gap x Leakage Factor}} = \frac{.249}{.318} \times .80 = .98$$

$$\text{Max. B/H} = \frac{\text{Max. Magnet Length}}{\text{Min. Gap x Leakage Factor}} = \frac{.251}{.292} \times .80 = 1.075$$

From the normal demagnetization curve for Samarium cobalt, the operating flux density is:

$B_{Min.}$ = 3.95 Kilogauss

$B_{Max.}$ = 4.15 Kilogauss

This variation is +3.75%, -1.25% from the design nominal of 4.0 Kilogauss. Considerable latitude is thus permissible in establishing the mechanical air gap without significantly affecting performance.

Another factor which contributes to a conservative design is that Samarium cobalt magnets manufactured recently are exceeding the normal demagnetization curve used (8 Kilogauss to 8 Kilo-oersteds).

WORST CASE EFFICIENCY

Efficiency of the unit as a generator is controlled by three factors:

1. Generated Back EMF,
2. Winding Resistance, and
3. Rotational Losses.

Under the operating conditions of 20,000 to 50,000 RPM, the variation in generated back EMF is controlled by the air gap flux density. Variation in density due to manufacturing tolerances and air gap dimensions was shown to be +3.75%, -1.25%. The other variable is magnet fabrication consistency.

This is typically ±5%. From Sperry's experience with Samarium cobalt, total unit-to-unit variation in back EMF does not exceed ±10%. This factor is used for worst case analysis and is considered quite conservative.

Winding resistance variation is primarily due to wire fabrication tolerances but is estimated to be ±10% to allow for winding technique and jumper/lead wire routing.

Rotational losses (eddy current losses) were determined as a worst case limit in the final report and are projected to be 3.7 watts maximum.

PARAMETER	NOMINAL	WORST CASE
K_B = Back EMF (Volts/Rad/Sec.)	.023	.0207
R = Resistance (Ohms)	.39	.429
W_E = Eddy Current Losses (Watts)	---	3.7

At 20,000 RPM

The worst case voltage at 20,000 RPM (2094 Rad/Sec) is:

$$V = K_B W = .0207\ (2094) = 43.35 \text{ Volts Peak}$$

and the average voltage is 35.86 volts peak.

The current at 250 watts is then--

$$\frac{250}{35.86} = 6.97 \text{ Amps.}$$

Using the worst case resistance of .429 ohm, the I^2R loss is 20.85 watts. Thus the worst case efficiency at 20,000 RPM is--

$$h = \frac{\text{Output Power x 100}}{\text{Output Power} + I^2R + W_E} = \frac{250 \times 100}{250 + 20.85 + 3.7} = 91.06\%$$

At 50,000 RPM

Using the same calculation method as for 20,000 RPM results in the following worst case parameters.

Average Voltage = 89.65 Volts

Current at 250 Watts = 2.789 Amps

I^2R Losses = 3.34 Watts

Worst Case Efficiency = 97.26%

The average efficiency over the operating range is then 95.2% worst case.

ACKNOWLEDGEMENTS

The author is grateful to Cornelius M. Sullivan for the inspired mechanical engineering effort resulting in the magnetic bearing realization. Also, thanks are due to Armand Bouvier whose persistent design work kept up with ever-changing concepts; and to the support of the Div. 6 Machine Shop under the direction of Frank Weibel and William Fielding, who produced excellent hardware in a timely manner. Thanks also to Steve Britten for the magnetic finite element program development, and to David Hyland for analysis of the anisotropic rotors.

UNCLASSIFIED

SECURITY CLASSIFICATION OF THIS PAGE *(When Data Entered)*

(18) (19) **REPORT DOCUMENTATION PAGE**

READ INSTRUCTIONS BEFORE COMPLETING FORM

1. REPORT NUMBER: ESD-TR-78-97	2. GOVT ACCESSION NO.
3. RECIPIENT'S CATALOG NUMBER	
(6) 4. TITLE *(and Subtitle)*: Flywheel Components for Satellite Applications	(9) 5. TYPE OF REPORT & PERIOD COVERED: Technical Note
6. PERFORMING ORG. REPORT NUMBER: Technical Note 1978-4	
(10) 7. AUTHOR(s): Alan R. Millner (14) TN-1978-4	8. CONTRACT OR GRANT NUMBER(s): (15) F19628-78-C-0002
9. PERFORMING ORGANIZATION NAME AND ADDRESS: Lincoln Laboratory, M.I.T. P.O. Box 73 Lexington, MA 02173	10. PROGRAM ELEMENT, PROJECT, TASK AREA & WORK UNIT NUMBERS: Program Element No. 65705F (16) ~~Project No.~~ 649L
11. CONTROLLING OFFICE NAME AND ADDRESS: Air Force Systems Command, USAF Andrews AFB Washington, DC 20331	(11) 12. REPORT DATE: 16 May 1978 13. NUMBER OF PAGES: 146
14. MONITORING AGENCY NAME & ADDRESS *(if different from Controlling Office)*: Electronic Systems Division Hanscom AFB Bedford, MA 01731 (12) 145 p.	15. SECURITY CLASS. *(of this report)*: Unclassified 15a. DECLASSIFICATION DOWNGRADING SCHEDULE

16. DISTRIBUTION STATEMENT *(of this Report)*

Approved for public release; distribution unlimited.

17. DISTRIBUTION STATEMENT *(of the abstract entered in Block 20, if different from Report)*

18. SUPPLEMENTARY NOTES

None

19. KEY WORDS *(Continue on reverse side if necessary and identify by block number)*

flywheel, rotors, hardware, bearings, attitude control, high efficiency, high-speed

20. ABSTRACT *(Continue on reverse side if necessary and identify by block number)*

The following paper studies the possibilities of using high-speed flywheels with magnetic bearings in communications spacecraft. Hardware point designs have been completed for a very low drag bearing and a very efficient, compatible motor generator. Using the results of these designs, a tradeoff study compares these flywheels with combinations of NiCd batteries, NiH_2 batteries, and conventional low-speed momentum wheels.

DD FORM 1 JAN 73 1473 EDITION OF 1 NOV 65 IS OBSOLETE

UNCLASSIFIED

SECURITY CLASSIFICATION OF THIS PAGE *(When Data Entered)*

207650 LB